

INELASTIC NEUTRON SCATTERING AND NEUTRON DIFFRACTION STUDIES
OF GAS HYDRATES

by

Kimberly Terri Tait

A Dissertation Submitted to the Faculty of the

DEPARTMENT OF GEOSCIENCES

In Partial Fulfillment of the Requirements
For the Degree of

DOCTOR OF PHILOSOPHY

In the Graduate College

THE UNIVERSITY OF ARIZONA

2007

GRADUATE COLLEGE

As members of the Dissertation Committee, we certify that we have read the dissertation prepared by Kimberly Terri Tait

entitled: INELASTIC NEUTRON SCATTERING AND NEUTRON DIFFRACTION STUDIES OF GAS HYDRATES

and recommend that it be accepted as fulfilling the dissertation requirement for the Degree of Doctor of Philosophy

Date: March 20, 2007
Dr. Robert T. Downs

Date: March 20, 2007
Dr. Roy Johnson

Date: March 20, 2007
Dr. Eric Seedorff

Date: March 20, 2007
Dr. Luke Daemen

Date: March 20, 2007
Dr. Charles Prewitt

Final approval and acceptance of this dissertation is contingent upon the candidate's submission of the final copies of the dissertation to the Graduate College. I hereby certify that I have read this dissertation prepared under my direction and recommend that it be accepted as fulfilling the dissertation requirement.

Date: March 20,
2007Dissertation Director: Dr. Robert T. Downs

STATEMENT BY AUTHOR

This dissertation has been submitted in partial fulfillment of requirements for an advanced degree at The University of Arizona and is deposited in the University Library to be made available to borrowers under rules of the Library.

Brief quotations from this dissertation are allowable without special permission, provided that accurate acknowledgment of source is made. Requests for permission for extended quotation from or reproduction of this manuscript in whole or in part may be granted by the head of the major department or the Dean of the Graduate College when in his or her judgment the proposed use of the material is in the interests of scholarship. In all other instances, however, permission must be obtained from the author.

SIGNED: Kimberly Terri Tait

ACKNOWLEDGMENTS

I would like to thank my primary thesis advisor Dr. Robert T. Downs, although we didn't spend a lot of time together, the time we did I will cherish. I also would like to thank my official mentor at the Los Alamos National Laboratory Yusheng Zhao, and all of my unofficial mentors throughout the years at the Lujan Center that helped me out because they truly cared.

I want to thank my committee members Luke Daemen, Charlie Prewitt, Roy Johnson, and Eric Seedorff for their valuable input on my dissertation.

Everyone at the Los Alamos Neutron Scattering Center deserves a special recognition, if I had the room; it didn't matter if it was 3am on a Saturday night there was always someone at the Lujan Center that was willing to help out, or drive back from Santa Fe on the weekend to make sure my experiment would be as successful as possible. I would especially like to thank Luke Daemen, Darrick Williams, Monika Hartl, Wendy Mao, Leilani Conradson, Thomas Proffen, Frans Trouw, Alan Shapiro, Eric Larson, Brad Shurter, Mark Taylor, Melvin Borrego, Tim Medina, Sven Vogel, Cristian Pantea, and on and on!

The funding for stipend and my thesis work was in part funded by the LDRD-DR "Clathrate hydrate science and technology" and then, "Stabilization of Hydrogen Clathrates --- Engineering a Solution to Hydrogen Storage" as well as a generous donation of money for the RRUFF project at the University of Arizona by Mike Scott. Financial support for travel and expenses for my thesis were provided in part by P.E.O. Scholar award Norah L. Wallace named grant, the International Centre for Diffraction Data Ludo Frevel Scholarship, the Tucson Gem and Mineral Society scholarship and the American Association of Petroleum Geologist Marta Sutton Weeks named grant.

I especially would like to thank my fiancé Sal Sena and my parents Alf and Peggy Tait for their continued support.

TABLE OF CONTENTS

LIST OF FIGURES	8
LIST OF TABLES	15
ABSTRACT.....	16
Chapter 1 CLATHRATE HYDRATES.....	17
1.1 Introduction to Clathrates	17
1.1.1 Structure I.....	20
1.1.2 Structure II	22
1.1.3 Structure H.....	24
1.2 Filling the hydrate cages	24
1.3 Natural gas hydrate samples	26
Chapter 2 GAS HYDRATE SYNTHESIS APPARATUS AND NEUTRON DIFFRACTION	
RESULTS	30
2.1 Motivation.....	30
2.2 USGS gas hydrate synthesis apparatus	30
2.3 Low-Temperature Scanning Electron Microscopy (LTSEM)	38
2.4 Methane-ethane hydrate.....	40
2.5 Introduction to neutrons.....	42
2.6 Los Alamos Neutron Scattering Center (LANSCE).....	43
2.7 Neutron scattering of pre-synthesized samples.....	45
2.7.1 HIPPO and ancillary equipment	45
2.7.2 Results methane 77.93% ethane 22.07% (norm.) sample.....	48
2.7.3 Results methane 82.93% ethane 17.07% (norm.) sample.....	49
2.7.4 Results 50% methane, 50% ethane sample.....	50
2.7.5 Results 100% Ethane gas hydrate sample.....	51
2.8 Los Alamos gas hydrate apparatus.....	52
Chapter 3 INELASTIC NEUTRON STUDIES OF TETRAHYDROFURAN CLATHRATE	
WITH HYDROGEN.....	57
3.1 Introduction.....	57
3.2 Previous work	58
3.3 Motivation of experiment	65

TABLE OF CONTENTS - Continued

3.4 Experimental details- Introduction.....	65
3.4.1 Pharos spectrometer	66
3.4.2 Pharos experimental details	68
3.4.3 NIST Center for Neutron Research and DCS	72
3.4.4 Disk Chopper Spectrometer (DCS) experimental details	72
Chapter 4 INELASTIC NEUTRON STUDIES OF ETHYLENE OXIDE CLATHRATE.....	74
4.1 Motivation.....	74
4.2 Structure.....	74
4.3 Dynamics: previous work	77
4.4 Dynamics: neutron scattering	82
4.4.1 The Filter Difference Spectrometer (FDS)	83
4.4.2 Synthesis of the deuterated ethylene oxide clathrate	85
4.4.3 Ethylene oxide clathrate: Results.....	87
4.4.4 Adding hydrogen	93
4.5 Summary	96
Appendix A METHANOL- INHIBITOR OR PROMOTER OF THE FORMATION OF GAS HYDRATES FROM DEUTERATED ICE?	97
Abstract.....	98
Introduction.....	99
Experimental Details.....	101
Results and Discussion	104
Appendix B HIGH-P/LOW-T NEUTRON SCATTERING OF HYDROGEN INCLUSION COMPOUNDS—PROGRESS AND PROSPECTS.....	121
Abstract.....	122
Introduction.....	124
Results and Discussion	126
Experimental Techniques.....	140
Appendix C INELASTIC NEUTRON SCATTERING STUDY OF HYDROGEN IN D ₈ - THF/D ₂ O ICE CLATHRATE.....	142
Abstract.....	143
Introduction.....	144

TABLE OF CONTENTS - Continued

Methods	145
Results.....	148
Discussion.....	155
Conclusion	170
Acknowledgments.....	171
REFERENCES	172

LIST OF FIGURES

Figure 1. The phase diagram of ice showing phases I – XI. Amorphous phases and Ice XII are not shown. http://www.lsbu.ac.uk/water/phase.html	19
Figure 2. Global distribution of gas hydrates from: http://www7430.nrlssc.navy.mil/7432/hydrates/background.htm	20
Figure 3a. 5^{12} small cage (pink) and $5^{12}6^2$ cage (blue) in the structure I clathrate structure; 3b. Ball and stick diagram of the oxygen (blue) and hydrogen (grey) of the structure I 5^{12} cage (left) and $5^{12}6^2$ cage (right) with the axes labeled.	22
Figure 4a. 5^{12} small cage (pink) and $5^{12}6^4$ cage (green) in the structure II clathrate structure; 4b. Ball and stick diagram of the oxygen (blue) and hydrogen (grey) of the structure II cages.....	23
Figure 5. 5^{12} small cage (pink), the $4^35^66^3$ medium cage (purple) and the $5^{12}6^8$ large cage (yellow).	24
Figure 6. Comparison of guest molecule sizes and cavities occupied as simple hydrates (Sloan, 1998a).	25
Figure 7. The inside of the sample preparation freezer at the USGS gas hydrate lab. Note the triply-distilled ice for the starting materials in freezer bags, top left, blender for freezing in the bottom left, and two sieves center and right-center.....	32
Figure 8. Photograph of the gas hydrate synthesis apparatus at the USGS. A conventional household freezer is used to cool the fluid that surrounds the two suspended samples and the gas reservoir. A heating element under the bath controls the temperature of the fluid.	33
Figure 9a. Schematic drawing of the USGS gas hydrate synthesis apparatus (modified from Stern et al., 2000); 9b. Schematic drawing of the reaction between the ice and gas.....	34
Figure 10a. P-T-t plot of a synthesis run of a 90% methane- 10% ethane (starting) gas hydrate at the USGS. Note the thermal anomaly at 273K due to the supercooled water freezing abruptly with an error pointing out the freezing anomaly. 10b. Fully converted gas hydrate from synthesis apparatus in indium sleeve (from Stern et al., 2000).....	35
Figure 11. Final gas concentrations of the second sample (methane/ethane) in a gas hydrate run at the USGS Organic Geochemistry Mass Spectrography Laboratory.....	37
Figure 12. Examples of dissociation features of the methane-ethane hydrate with the LTSEM; scale is shown in bottom of the photos.	39
Figure 13a. Cohesive methane-ethane hydrate sample with porosity; 13b. granular ethane hydrate with individual crystal morphology shown. Scale of images shown on photos.	40
Figure 14. Predicted composition region for the structural transition to occur (Subramanian et al., 2000a).....	41
Figure 15. Comparison of atomic number dependence vs. scattering length, b for X-rays and neutrons (Krawitz, 2001).....	43

LIST OF FIGURES - Continued

Figure 16. Schematic diagram of the two experimental areas at the Lujan Center, experimental area-1 and -2 (ER-1 and ER-2), where 17 available flight paths surround the tungsten target (figure supplied by LANSCE-Lujan Center).....	44
Figure 17. Schematic of the HIPPO chamber, denoting the beam path through the diffractometer, the sample chamber, and the panels of detectors (figure supplied by LANSCE-Lujan Center).....	45
Figure 18a) top-hat setup being craned into NPDF (photo courtesy of Thomas Proffen); 18b) typical closed cycle refrigerator for neutron experiments used at LANSCE (from http://www.arscryo.com/csw204.html)	46
Figure 19a. Schematic general view (top left corner) and the enlarged section view of the setup designed for high-pressure, low-temperature hydrostatic experiments at LANSCE (Lokshin and Zhao, 2005); 19b. photo of internal cell at liquid nitrogen temperatures attached to the closed cycle cryostat (photo courtesy of K.A. Lokshin).	47
Figure 20. Rietveld LeBail fit (green line) of the three-phase methane-ethane gas hydrate diffraction pattern (red marks) with the $\chi^2 = 3.24$; ticks on the bottom of the figure show the d-spacing positions of the three phases: structure II- black, ice- red, structure I- blue) and some of the major peaks have been identified with arrows for ease of comparison.	49
Figure 21. Rietveld LeBail fit (green line) of the three-phase methane-ethane gas hydrate diffraction pattern (red marks) with the $\chi^2 = 3.45$; ticks on the bottom of the figure show the d-spacing positions of the three phases: structure II- black, ice- red, structure I- blue) and some of the major peaks have been identified with arrows for ease of comparison.	50
Figure 22. Rietveld fit (green line) of the 50:50 methane-ethane gas hydrate diffraction pattern (red marks); ticks on the bottom of the figure show the d-spacing positions of the three phases: structure II- black, ice- red, structure I- blue). Some of the major peaks have been identified with arrows for ease of comparison.	51
Figure 23. Rietveld LeBail fit (green line) of the two-phase ethane gas hydrate diffraction pattern (red marks) with the $\chi^2 = 2.22$; ticks on the bottom of the figure show the d-spacing positions of the three phases: structure I- black, ice- red) and some of the major peaks have been identified with arrows for ease of comparison.	52
Figure 24. Early conceptual design of the gas hydrate gas handling system at the Los Alamos Neutron Scattering Center.	53
Figure 25. Schematic diagram of the gas hydrate synthesis apparatus with valve numbers and lengths of tubing.	55
Figure 26. Picture of gas hydrate synthesis apparatus at LANSCE, inset- schematic diagram of final gas hydrate synthesis apparatus at LANSCE.....	55
Figure 27. LabVIEW front panel for gas hydrate syntheses at Los Alamos.....	56

LIST OF FIGURES - Continued

Figure 28. Volume of 4 kg of hydrogen compacted in different ways, with size relative to the size of a car (Schlapbach and Zuttel, 2001).....	58
Figure 29a) The sII crystal structure consisting of $5^{12}6^4$ and 5^{12} cages; b) the tetrahedral cluster of four hydrogen molecules in the $5^{12}6^4$ cage; c) a cluster of two hydrogen molecules oriented towards opposite pentagonal faces in the 5^{12} cage.	59
Figure 30. Temperature dependence of D_2 occupancy in the large (diamond symbols) and small (circle symbols) cages of the hydrogen clathrate hydrate structure. Open and filled symbols represent data obtained at ambient and high (~ 2 kbar) pressures, respectively. Data points with no error bars represent the values, which were fixed in the final refinements but were refined in the range 3.8(2) – 4.2(2) for the large cage and 0.9(1) – 1.1(1) for the small cage in the initial refinements. No significant correlation between large and small cage occupancy parameters was observed (Lokshin et al., 2004).....	60
Figure 31. Sketch of a tetrahydrofuran molecule (C_4H_8O) the oxygen has two lone pairs of electrons sticking out from the ring. These electron pairs represent a large electronic density and make it easy for THF to participate intermolecular bonding, e.g., via hydrogen bonding.	61
Figure 32. H_2 gas content (wt %) as a function of THF concentration and a schematic diagram of H_2 distribution in the cages of THF + H_2 hydrate (Lee et al., 2005).....	63
Figure 33a. Observed Fourier map of the THF- d_8 system centered in the $5^{12}6^4$ cavity at (3/8, 3/8, 3/8) with the ring of density attributed to the THF- d_8 molecule and the density contours on the edges due to the water molecules. The map size is 10 Å, and the contours are drawn at 0.1 – 10 fm. 6b. Observed Fourier map of the D_2 + THF- d_8 system centered in the 5^{12} cavity at (0,0,0) with the single hydrogen molecule centered in the picture and the other density contours attributed to portions of the water cage. The map size is 8 Å, and contours are drawn at 0.2 – 2.0 fm. Both are figures from Hester et al., 2006.	64
Figure 34. Summary of hydrogen cage occupancies in gas hydrates (http://www.hydrogen.energy.gov/pdfs/review06/bes_st11_sloan.pdf).....	66
Figure 35. Schematic of the High-Resolution Chopper Spectrometer, Pharos at LANSCE (supplied by LANSCE-Lujan Center).	67
Figure 36a. Schematic of the gas hydrate cell designed at LANSCE for Pharos experiments; 9b. Cutaway view of the internal structure of the cell- seven sample wells, split by 1/10" Al for safety concerns (supplied by M. Taylor, designer from LANSCE).	68
Figure 37. Schematic of gas handling system (V = valve, and BD = burst disk) and picture of actual setup on top of the Pharos instrument.	71
Figure 38. Schematic of isotope substitution of experiments on THF + H_2 on Pharos.	71
Figure 39. ILL designed liquid helium bath orange cryostat.....	73

LIST OF FIGURES - Continued

Figure 40. The ethylene oxide molecule. The molecule is significantly larger than methane and is highly polar (dipole moment 1.88 Debye -virtually identical to that of water) owing to the large electron density on the oxygen atom (figure from L. L. Daemen).	75
Figure 41. The crystal structure of $C_2H_4O \cdot 6.86H_2O$ as determined by McMullan and Jeffrey (1965) by single crystal X-ray diffraction at 243 K. Ethylene oxide is not shown for clarity; each O-O bond shows two sites for hydrogen. Each site has an average occupancy of 0.5 and two unit cells are shown. Two large cages (tetrakaidecahedra) are clearly visible at the center of the figure. Dodecahedra appear at the center of each cubic unit cell.	76
Figure 42. The $5^{12}6^2$ structure I tetrakaidecahedron cage with only the oxygen atoms of the cage shown, with two preferred orientations of the ethylene oxide molecule shown (McMullan and Jeffrey, 1965).	77
Figure 43. Frequency distributions at 30 K, 90 K and 214 K (Wegener et al., 1978).	82
Figure 44. Schematic of the Filter Difference Spectrometer (FDS) at LANSCE (Supplied by LANSCE-Lujan Center).	83
Figure 45. Setup for the synthesis of ethylene oxide clathrates. A carefully measured volume of D_2O is placed in a glass tube connected to valve C. The D_2O is frozen with liquid nitrogen and with valves B, C, S, and V open (A closed) the apparatus is evacuated. Subsequently V, S, and C are closed and with B open, A is opened to fill the calibrated volume connected to valve B. Once the desired pressure of ethylene oxide is reached in the calibrated volume, valve A and B are closed and the apparatus is again evacuated to remove residual ethylene oxide in the apparatus. Valves B, C, and S are then opened to condense the ethylene oxide in the calibrated volume into the glass tube containing D_2O . When the pressure in the calibrated volume falls to zero, valve C and S are closed and the sample tube is disconnected (between C and S) from the vacuum line. Its content is allowed to warm up to room temperature. Gentle mechanical agitation then allows for thorough mixing of D_2O and ethylene oxide. The solution is then transferred to an aluminum sample holder (for neutron scattering) and slowly cooled below its freezing point to form the clathrate.	87
Figure 46. Neutron vibrational spectrum of ethylene oxide clathrate collected at 10 K on FDS. Peaks A, B, and C are the librational modes of ethylene oxide. The labeling corresponds to that used by Wegener et al. (1978) (see Figure 43). Peak D and the broad band E are discussed in the text. The arrows indicate two shoulders that were not present in the Wegener et al. result.	88
Figure 47. The high frequency portion of ethylene oxide clathrate. The solid line is a maximum entropy reconstruction of the vibrational spectrum.	91
Figure 48. Neutron vibrational spectrum of hydrogen loaded in ethylene oxide clathrate, $T=40$ K. The spectrum from the pure ethylene oxide clathrate was subtracted to highlight the contribution from hydrogen. Two large	

LIST OF FIGURES - Continued

peaks are clearly visible at 126 and 150 cm^{-1} . The solid line is the Maximum Entropy reconstruction of the spectrum.	95
Figure A-1. A schematic drawing of the aluminum pressure cell. The cell is approximately 76 mm long and has an inside diameter of 8 mm.	102
Figure A-2. Virtually real time monitoring (15 minutes per histogram) of the kinetics of formation of CO_2 hydrate from polycrystalline ice by in situ neutron powder diffraction. (a) Beginning of the reaction—neutron powder diffraction pattern of the D_2O ice (hexagonal structure, space group P63/mmc) at 200 K with no pressure; A-2b. Reaction in progress, system pressurized with either CO_2 or CH_4 —neutron powder diffraction pattern of the mixture of hexagonal D_2O ice and type-I hydrate. This pattern can be viewed as a superposition of patterns (a) and (c), with relative intensities corresponding to the mole fractions of the two phases, respectively. A2-c. End of the reaction, i.e., all D_2O ice converted in situ to hydrate—neutron powder diffraction pattern type-I hydrate (primitive cubic structure, space group Pm-3n) at 200 K and 7 MPa He. The y-axis (not shown) represents the intensity in arbitrary units.	109
Figure A-3. Conversion of deuterated ice to carbon dioxide hydrate at 6 MPa at temperatures of 263 and 253 K (filled symbols represent the fraction of hydrate, open symbols stand for the fraction of ice). Each data point represents the mole fraction as refined from a 15 min histogram. Data from Henning et al. (2000), courtesy of A. J. Schultz.....	110
Figure A-4. In situ neutron powder diffraction patterns of a frozen $\text{D}_2\text{O} + \text{CD}_3\text{OD}$ mixture at 220 K with no pressure (a); and the corresponding patterns 20 minutes (b) and 40 minutes (c) after the system was pressurized with CO_2 at 250 K and 1.7 MPa. Due to the rapid conversion rates, the fractions of ice and hydrate could not be accurately refined. The y-axis (not shown) represents the intensity in arbitrary units.	112
Figure A-5. Comparison between the rate of conversion of deuterated ice to carbon dioxide hydrate at 6 MPa and at 230 K and the rate of conversion of a mixture of deuterated ice and deuterated methanol to carbon dioxide hydrate at the same pressure and at a temperature of 200 K.....	115
Figure A-6. In situ neutron powder diffraction patterns of a frozen $\text{D}_2\text{O} + \text{CD}_3\text{OD}$ mixture at 200 K with no pressure (a); and the corresponding pattern 90 minutes (b) after the system was pressurized with CH_4 at 200 K and 1.7 MPa. The higher background is due to the presence of H (large incoherent scattering cross-section). The y-axis (not shown) represents the intensity in arbitrary units.	118
Figure A-7. Fitted neutron diffraction pattern of a mixed methane-ethane sI clathrate (82.93 wt% methane + 17.07 wt% ethane) with minor sII phase and D_2O ice. Data are shown as red plus signs, and the green curve is the best fit to the data. Tick marks below the pattern show the positions of allowed reflections (blue – sI phase; red – ice; black – sII phase). The insert shows neutron patterns of methane clathrate formed from ice and D_2 in	

LIST OF FIGURES - Continued

<i>situ</i> in the Al pressure cell. Note that formation of methane clathrate was not complete even after 10 h at 500 bar and 270 K, indicating sluggish formation kinetics compared with hydrogen clathrate (see below).	128
Figure A-8. Neutron diffraction patterns of deuterium clathrates produced from (A, B) water and (C) powdered ice, at approximately the same P-T conditions (Lokshin & Zhao, 2005). Note that the formation kinetics of D ₂ -clathrates formed from ice powder is much faster than from water.	131
Figure A-9. Structural view of D ₂ distribution in the large (top) and small (bottom) cages of deuterium clathrate (Lokshin et al, 2004). Oxygen atoms are shown as red spheres, deuterium framework atoms—green, and guest D ₂ molecules—yellow. Note that the D ₂ ···D ₂ separation is the distance between the centers of mass of the two D ₂ molecules. Below 50 K, the guest D ₂ molecules are localized (left). With increasing temperature, the D ₂ molecules can rotate more freely, yielding a nearly spherical D ₂ density distribution (right).	131
Figure A-10 (A) Fitted neutron diffraction pattern of Cu ₃ [Co(CN) ₆] ₂ at 40 K and 10 MPa of D ₂ pressure. Data are shown as red plus signs, and the green curve is the best fit to the data. Tick marks below the pattern show the positions of allowed reflections (first row – Al cell; second row – sample). The insert shows increased unit-cell volume under 10 MPa of D ₂ pressure at 100 K. (B) Crystal structure of Cu ₃ [Co(CN) ₆] ₂ ·9H ₂ O at ambient condition (brown – Cu; pink – Co; black – C; light blue – N; dark blue – water). (C) Crystal structure of Cu ₃ [Co(CN) ₆] ₂ ·nH ₂ (green – H ₂) showing H ₂ at the (¼, ¼, ¼) site (the relatively large green sphere illustrates free-rotation of H ₂ molecules in the cages). (D,E) Difference Fourier nuclear maps showing that the incorporated D ₂ molecules mainly occupy the original water site (¼, ¼, ¼) (D) with some possibly associated with Cu (E). The residual intensities at the Co and Cu sites are due to the limited resolution of our data and the strong scattering of Co and Cu.	135
Figure A-11. Low frequency neutron vibrational spectrum of Cu ₃ (BTC) ₂ with its crystal structure shown as an insert. Cu ₃ (BTC) ₂ has three H ₂ equivalents adsorbed at 40 K. The curve is a maximum entropy reconstruction of the spectrum. It enhances some details that are present in the data (dots) but may be not easy to see.....	136
Figure A-12. Structure diagram of a potential hybrid material of the metal-organic framework (MOF) with the CH ₄ (H ₂) ₄ molecular compound encapsulated into its cage. MOF consists of metal-oxygen clusters (tetrahedra) on the vertices of the lattice and organic linker molecules (hexagons) along its edges, which largely define the size and shape of the cage. Blue balls in CH ₄ (H ₂) ₄ represent CH ₄ , and red balls represent H ₂	138
Figure A-13. Schematic general view (in the top-left corner) and the enlarged sectional view of the experimental setup designed for in situ high-P low-T neutron diffraction at LANSCE (Lokshin & Zhao, 2005).	140
Figure A-14: Diffraction pattern from ternary clathrate H ₂ /d ₈ -THF/D ₂ O at 5 K measured on DCS with an incident wavelength of 5.5 Å. The three shaded peaks are from residual ice in the sample.....	150

LIST OF FIGURES - Continued

Figure A-15: Inelastic scattering spectrum from THF-ice clathrate before and after the addition of hydrogen measured at 8 K.....	151
Figure A-16: Model fit using multiple Gaussians and a sloping background for the neutron energy gain data measured on Pharos at 8 K.....	151
Figure A-17: Model fit using multiple Gaussians and a sloping background for the neutron energy loss data measured on Pharos at 8 K.....	152
Figure A-18: Neutron energy gain peaks observed on DCS at 5 K (squares) and 50 K (triangles).	154
Figure A-19: Upper trace is H ₂ /d-THF/D ₂ O measured at 8 K using an incident energy of 70 meV on Pharos. Lower curve is the equivalent spectrum measured for TDF/D ₂ O at 8 K using an incident energy of 120 meV. Both curves are a sum of S(Q,E) for Q=1-5 Å ⁻¹	154
Figure A-20: Two Gaussian plus sloping background fit of the Pharos data measured at 8 K with 70 meV incident neutrons.	156
Figure A-21: Comparison between the prediction from the 5D quantum theoretical model (line) and the data measured on Pharos at 8 K.	161
Figure A-22: Comparison between prediction of particle in a box model (line) and the experimental data measured at 8 K on Pharos.	164
Figure A-23: Comparison between prediction for particle in a sphere of radius 1.8 Å (line) and the data taken on Pharos at 8 K.	165
Figure A-24: Comparison between the excitations expected for particle on the surface of a sphere with radii 1.05 and 1.1 Å, and the data taken on Pharos at 8 K.	167
Figure A-25: Debye-Waller plots from the DCS data, with the intensity summed over the neutron energy loss range of +/-1 meV.	168
Figure A-26: Temperature dependence of the hydrogen molecule Debye-Waller Factor (squares). Also shown is the variation in the zero-Q intercept of the fits in Figure A-25 (triangles, arbitrary units).	170

LIST OF TABLES

Table 1. Ratio of molecular diameters to cavity diameters for natural gas hydrates formers (modified from Sloan, 1998b). _____	28
Table 2. Comparison of molecular compounds with Department of Energy (DOE) hydrogen storage targets (modified from Mao and Mao, 2004). _____	61
Table 3. Mol % THF (starting solution) vs. H ₂ :THF mole ratio in the hydrate vs. max wt% H ₂ in the hydrate for the three regions as outlined by Lee et al. 2005. _____	62
Table 4. Summary of all runs performed over 44 days of beam time on Pharos, organized by the selected incident energy of the experiment. _____	70
Table 5. Absorption peaks observed in the vibrational spectrum of C ₂ H ₄ O · 6.86D ₂ O by Bertie et al. (1975) at 4.3 K. _____	78
Table 6. Librational frequencies of ethylene oxide in ethylene oxide clathrate. Comparison of infrared absorption and inelastic neutron scattering measurement. _____	89
Table 7. Internal modes of enclathrated ethylene oxide measured on FDS as well as in the gas phase. _____	94
Table A-1: Results from fitting the H ₂ scattering data measured at 8 K. _____	152
Table A-2: Energies of the translational quantum states of ortho- and para-hydrogen predicted by (Xu et al., 2006), and the predicted neutron energy gain transitions from the ortho-hydrogen translational ground state. _____	160

ABSTRACT

Gas hydrates (clathrates) are elevated-pressure (P) and low-temperature (T) solid phases in which gas molecule guests are physically incorporated into hydrogen-bonded, cage-like ice host frameworks. Natural clathrates have been found worldwide in permafrost and in ocean floor sediments, as well as in the outer solar system (comets, Mars, satellites of the gas giant planets). Diffraction patterns have been collected of gas hydrates at various methane and ethane compositions by preparing samples in an *ex situ* gas hydrate synthesis apparatus, and CO₂ gas hydrates were prepared *in situ* to look at the kinetics of formation.

Storage of hydrogen in molecular form within a clathrate framework has been one of the suggested methods for storing hydrogen fuel safely, but pure hydrogen clathrates H₂(H₂O)₂ form at high pressures. It has been found that mixed clathrates (a stabilizer molecule in the large cage) and hydrogen gas together can reduce the pressures and temperatures at which these materials form.

In situ neutron inelastic scattering experiments on hydrogen adsorbed into a fully deuterated tetrahydrofuran water ice clathrate show that the adsorbed hydrogen has three rotational excitations (transitions between $J = 0$ and 1 states) at approximately 14 meV in both energy gain and loss. These transitions could be unequivocally assigned the expected slow conversion from ortho- to para-hydrogen resulted in a neutron energy gain signal at 14 meV, at a temperature of 5 K ($kT = 0.48$ meV). A doublet in neutron energy loss at approximately 28.5 meV are interpreted as $J = 1 \rightarrow 2$ transitions.

In situ neutron inelastic scattering experiments on hydrogen adsorbed into ethylene oxide, a structure I former, were also carried out at the Los Alamos Neutron Scattering Center (LANSCE). There is convincing evidence (shifted rotational mode of molecular hydrogen) that hydrogen is capable of diffusing in the small cages of ethylene oxide clathrate. Values are also obtained for the librational modes of enclathrated ethylene oxide and several water translation modes. Also reported for the first time are the internal modes (higher frequencies) of ethylene oxide in ethylene oxide clathrate as measured by inelastic neutron scattering.

Chapter 1

CLATHRATE HYDRATES

1.1 Introduction to Clathrates

The Merriam-WebsterTM dictionary defines the word “clathrate” as “relating to or being a compound formed by the inclusion of molecules of one kind in the cavities of the crystal lattice of another.” The etymology of the word clathrate can be traced to the Latin root *clathratus* for “furnished with a lattice,” or *clathri* (plural) for “lattice”; today, the word clathrate is used to describe compounds that display a host-guest relationship. Tetrahedrally bound silicon “cages,” with sodium atoms as the “guest” species have been described (e.g. Kasper, 1965), as well as germanium and tin analogs (e.g. Gallmeier et al., 1969) and the structurally related carbon-based fullerenes (e.g. Kroto et al., 1985). Clathrates in this thesis will refer to the H₂O-bonded (or D₂O-bonded) cage structure with a variety of guest molecules.

Ice is a remarkably complicated material that has fourteen currently known solid phases, including three amorphous phases (Figure 1). Virtually all ice in the biosphere is ice Ih (Space group *P6₃/mmc*) because it is stable at ambient temperatures down to 73 K and exists at ambient pressures up to 0.2 GPa (or 2⁹ Pa, Figure 1). Since all clathrate structures consist of approximately 85% water on a molecular basis, many of the clathrate mechanical properties resemble those of a hexagonal ice- ice Ih (Sloan, 1998a). Ice Ih is a quartz-like layer structure, a tridymite lattice with a relatively loose packing, in which three-quarters of the bonds are in a central-symmetrical arrangement and one-quarter is in a mirror-

symmetrical arrangement, and symmetrical cavities are formed between them. Each cavity is surrounded by six water molecules at a distance of 2.94 Å from the center. Around each water molecule there are six cavities at a distance of 3.47 Å that form uninterrupted channels. In water, four valence electrons form two “lone-pair” orbitals; the hydrogen bond is caused by the attraction of the positive pole on one molecule to a negative pole on the neighboring water molecule (Sloan, 1998a). In ice and in hydrates, only one hydrogen (or proton) lies between two oxygen atoms with a distance between oxygen nuclei of 2.76 Å. When polar or slightly polar gas molecules come into contact with water near the freezing point of water, a clathrate forms. This physical enclosing process, accompanied only by weak interactions, take place between the host and guest constituents when the guest enters the cavities in the host lattice. The guests are released from the cavities only when the host lattice breaks down (Berecz and Balla-Achs, 1983). In principle, any gas molecule that is small enough to fit in the cavity of the water lattice can form a gas hydrate.

The most common naturally occurring gas hydrate is methane hydrate, which forms in permafrost, ocean floor sediment, as well as in the outer solar system (comets, Mars, satellites of the gas giant planets). Clathrates in oceanic deposits have a great potential as an energy resource for the future; some scientists have estimated that the global reserve of methane in hydrate form contains more than twice the energy of all natural gas, petroleum, and coal deposits combined (Figure 2) (Kvenvolden, 2000; Sloan, 1998a). In a fully saturated structure I clathrate, 1 molecule of methane is present for every 5.75 molecules of

water. In principle, 1 m³ of methane hydrate can contain up to 164 m³ of methane gas at standard pressure and temperature (Kvenvolden, 2000).

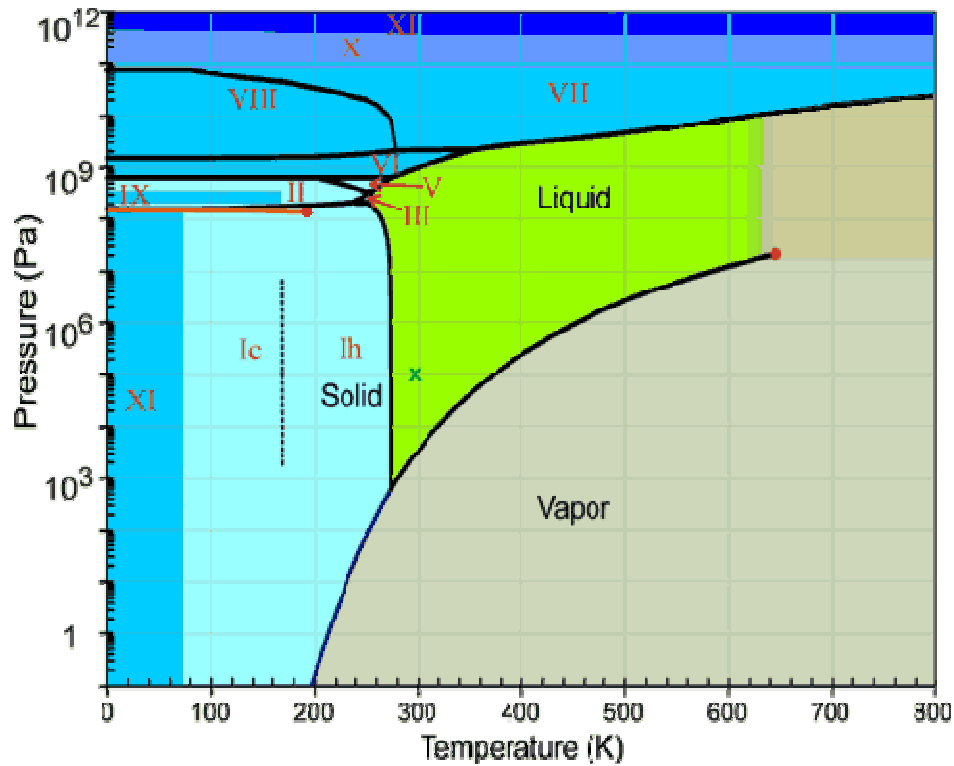


Figure 1. The phase diagram of ice showing phases I – XI. Amorphous phases and Ice XII are not shown. <http://www.lsbu.ac.uk/water/phase.html>.

Clathrates in oceanic deposits exist in rather delicate equilibrium conditions, and certain perturbations, such as depressurization and/or warming, can cause decomposition into methane gas and water. This reaction has significant implications for clathrate exploitation because methane released to the atmosphere due to destabilization of ocean-floor hydrates could exacerbate greenhouse effects and potentially contribute to global warming.

Clathrate hydrates exhibit three main crystal structures, denoted I, II and H. A structure III has been reported, but it is a filled-ice structure, not a clathrate structure, and will not be discussed here.

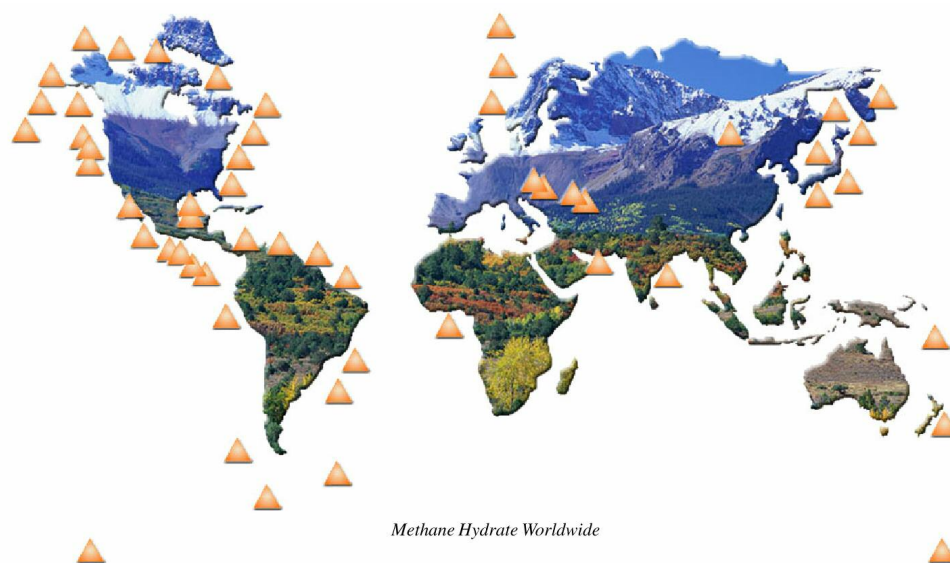


Figure 2. Global distribution of gas hydrates from:
<http://www7430.nrlssc.navy.mil/7432/hydrates/background.htm>

1.1.1 Structure I

Structure I gas hydrates consist of 5^{12} cages and $5^{12}6^2$ cages that form a cubic $Pm\bar{3}n$, body-centered cell ($a = 12 \text{ \AA}$) with an ideal unit cell formula of $6X \cdot 2Y \cdot 46\text{H}_2\text{O}$ (X and Y refer to large $5^{12}6^2$ cage and the 5^{12} , respectively).

Two spherical pentagonal-dodecahedral cavities (5^{12} cage) are each surrounded by 20 water molecules at a distance of 4.2 \AA from the center of the cavity (Berez and Balla-Achs, 1983). The 14-sided cavity (tetrakaidecahedron) is called $5^{12}6^2$ because it has 12 pentagonal

and two hexagonal faces (Figure 3). In the event of total occupation of the cavities, the formula of the resulting gas hydrate is $X \cdot 5.75 \text{ H}_2\text{O}$ (where X denotes the hydrate-forming molecule). If the gas molecule is too large to be incorporated into the small cavity, only the large cavities are occupied. The ideal composition would then be $X \cdot 7.67 \text{ H}_2\text{O}$.

There are three crystallographically nonequivalent oxygen atoms in the hydrate cage, and six crystallographically nonequivalent deuterium or hydrogen atoms. In the 5^{12} cage, there is only 1.5° departure of the O-O-O angles from the tetrahedral angles of ice Ih and only 3.5° departure from the free-water angle (Sloan, 1998a). There are twenty water molecules on the surface of the cage with thirty bonds; ten water molecules have hydrogen atoms pointing away from the cavity as potential points of attachment to other molecules or cavities (Sloan, 1998a).

The $5^{12}6^2$ cavity is the most non-spherical cavity in sI or sII. There are four crystallographically different types of oxygen sites at 4.25 Å, 4.47 Å, 4.06 Å, and 4.64 Å from the center of the cage, making the cage an oblate ellipsoid. This cavity also has the largest O-O-O angle variation (5.1°) from the tetrahedral angle preferred by water (Sloan, 1998a).

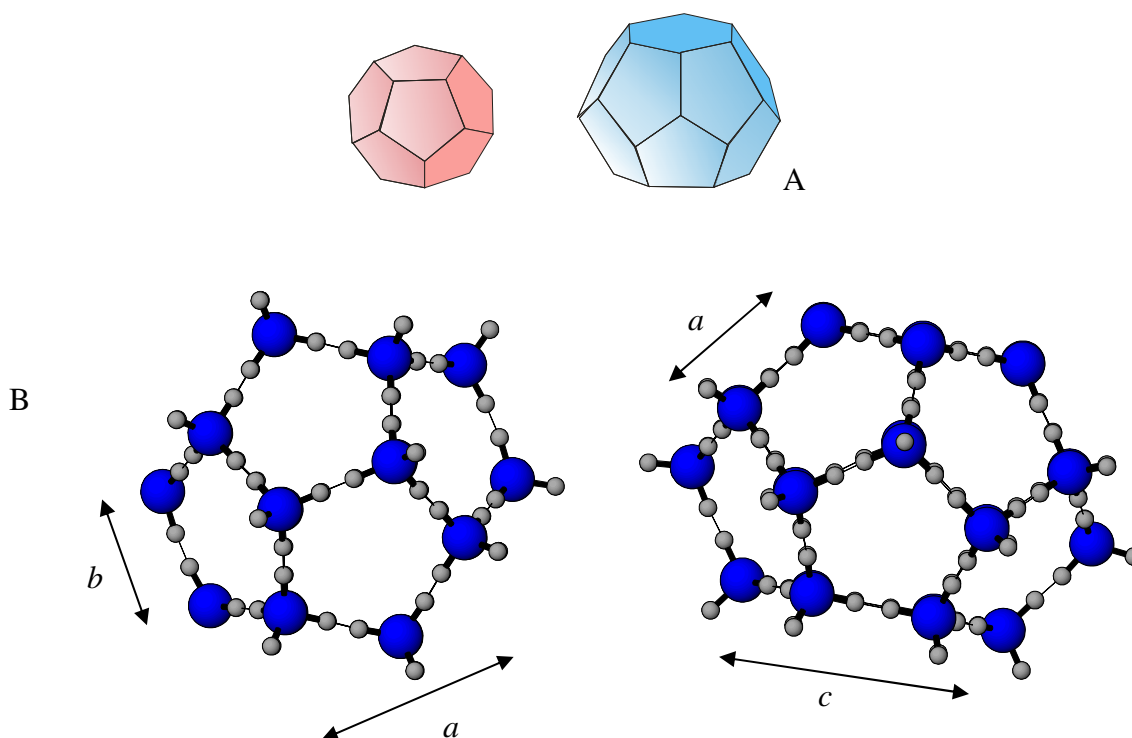


Figure 3a. 5¹² small cage (pink) and 5¹²6² cage (blue) in the structure I clathrate structure; 3b. Ball and stick diagram of the oxygen (blue) and hydrogen (grey) of the structure I 5¹² cage (left) and 5¹²6² cage (right) with the axes labeled.

1.1.2 Structure II

The unit cell consists of 136 water molecules- 16 pentagonal-dodecahedral (5¹²) and 8 hexakaidecahedral cavities (5¹²6⁴) to form a cubic diamond lattice $Fd\bar{3}m$ ($a = \sim 17.3 \text{ \AA}$) (Berecz and Balla-Achs, 1983) (Figure 4). In this hydrate type, the composition of the resulting hydrate when the small cages are occupied is $X \cdot 5.66 \text{ H}_2\text{O}$, or, if only the large cavities are filled, the composition is $X \cdot 17 \text{ H}_2\text{O}$.

The 5^{12} cage in the structure II clathrate is similar to the 5^{12} cage in structure I; only in structure I the average cage radius is 3.95 \AA , and structure II is 3.91 \AA , which plays a slight role in certain gas molecules fitting in these small cages. The $5^{12}6^4$ cavity can contain molecules as large as 6.6 \AA .

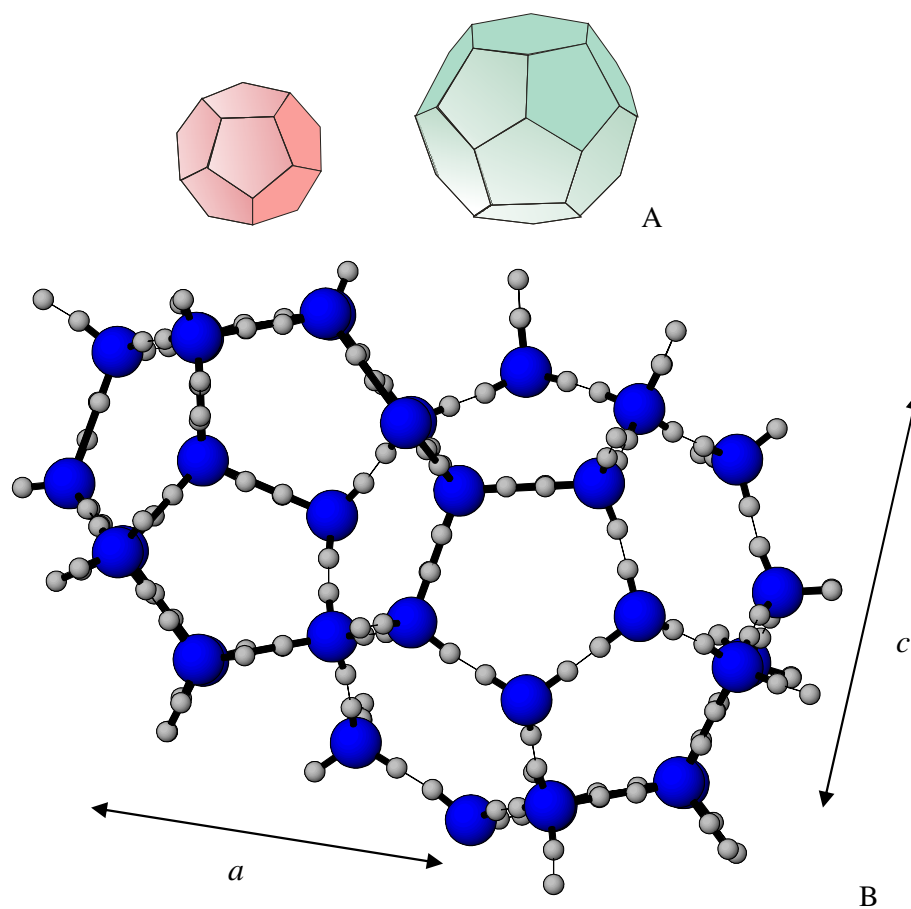


Figure 4a. 5^{12} small cage (pink) and $5^{12}6^4$ cage (green) in the structure II clathrate structure; 4b. Ball and stick diagram of the oxygen (blue) and hydrogen (grey) of the structure II cages.

1.1.3 Structure H

The structure H hydrates (Figure 5) form a hexagonal structure, $P6/mmm$ with $a = 12.3 \text{ \AA}$ and $c = 10.17 \text{ \AA}$ (approximately) which can only have a small occupant (such as methane, nitrogen, or carbon dioxide) in the small cage and a large occupant for the large cage (up to 9 \AA , e.g. ethylcyclohexane). There are three pentagonal-dodecahedral cavities (5^{12}), two medium irregular dodecahedron cavities ($4^3 5^6 6^3$) that have three-square faces and three hexagonal faces, in addition to six pentagonal faces. The largest ($5^{12} 6^8$) cavity has twelve pentagonal faces, as well as a band of six hexagonal faces and a hexagonal face at the cavity top and bottom (Sloan, 1998).

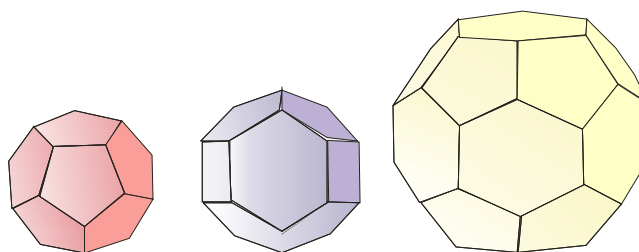


Figure 5. 5^{12} small cage (pink), the $4^3 5^6 6^3$ medium cage (purple) and the $5^{12} 6^8$ large cage (yellow).

1.2 Filling the hydrate cages

At ambient pressures the three main hydrate structures can generally only contain, at most one guest molecule (except for some noble gases and hydrogen etc). Molecules smaller than 3.5 \AA are too small to stabilize any cavity, while above 7.5 \AA are too large to fit into any cavity in sI or sII (Sloan, 1998a). Some molecules can only stabilize the large cavity of a structure, but if the molecule stabilizes the small cavities of the structure (in other words, is

physically small), it can also enter the large cavity of the structure (Sloan, 1998a) (Figure 6). Of the more than 130 compounds that form clathrate hydrates with water molecules, all form either a structure I (sI), structure II (sII), or structure H (sH), with very few exceptions (Sloan, 1998a).

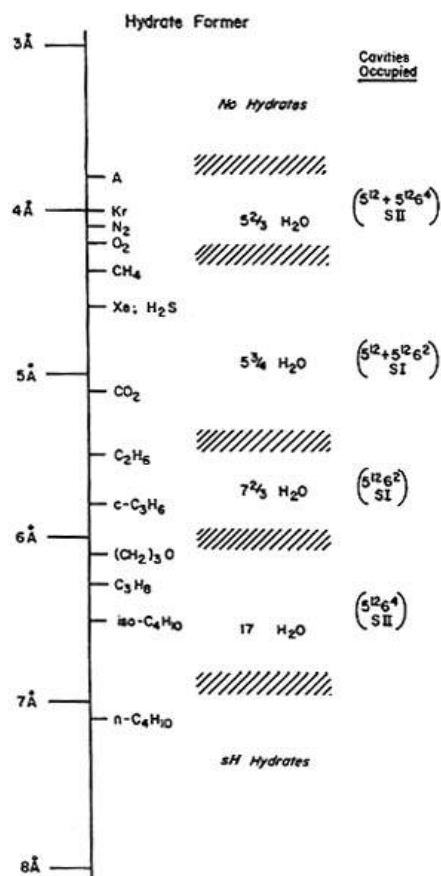


Figure 6. Comparison of guest molecule sizes and cavities occupied as simple hydrates (Sloan, 1998a).

1.3 Natural gas hydrate samples

Natural clathrates have been found worldwide in permafrost and in ocean floor sediments, as well as in the outer solar system (the Moon, comets, Mars, satellites of the gas giant planets). Natural gas hydrates form in oceanic sediments and permafrost from a gas mixture that contains primarily methane (CH_4), as well as ethane (C_2H_6), propane (C_3H_8), and other gases in smaller amounts. Most (99.99%) hydrates in nature are methane hydrates, which could be due to the fact that methane is preferentially incorporated into the clathrate structure over other natural gases. But this does not explain the abundance of methane gas (relative to ethane and propane) in most natural hydrates. The vast majority of clathrate hydrates near the Earth's surface are probably the result of biogenic conversion of organic matter into methane gas at shallow depths (Buffett, 2000).

Of the natural gas components in nature, only ethane and carbon dioxide stabilize the $5^{12}6^2$ cavity; if the 5^{12} cavities of structure I are stabilized by smaller molecules of a single component, those molecules will also occupy the $5^{12}6^2$ cavities (Sloan, 1998a).

Since methane and ethane are relatively small molecules, they individually form structure I hydrate, but when mixed form a structure II hydrate. Propane is too large to fit into either cavity of structure I, but it fits into the large cavity of structure II. Thermal conversion of organic matter into hydrocarbon gases at temperatures in excess of 80°C produces larger quantities of ethane and propane, and therefore, differences in the composition of the hydrates is due to the differences in gas supply (Buffett, 2000).

Structure I has two small polyhedra for every six large polyhedra, whereas structure II has 16 smaller polyhedra for every 8 larger polyhedra. The average cavity radius of the smaller cages is similar for structure I and II, 3.95 and 3.91 Å, respectively. However, the average cavity radius of the larger cages shows a significant difference- 4.33 Å for structure I compared to 4.73 Å for structure II (Rawn et al., 2003). Even though the small 5^{12} cage is common to all three structures, I, II and H, the symmetry and size of these small cages is different (Ripmeester and Ratcliffe, 1998).

Methane, the smallest hydrocarbon, can enter the small and large cavities in both structure I and structure II, but structure I is preferred because methane contributes more to the stability of the cages. However, mixtures of methane and larger gas molecules will form structure II. Table 1 shows the size ratio of several common gas molecules within each of the four cavities- a size ratio of approximately 0.9 is necessary for stability of a simple hydrate. When the size ratio exceeds unity, the molecule will not fit within the cavity and therefore, a clathrate will not form (Sloan, 1998b).

		(molecular diameter)/(cavity diameter)			
		structure I		structure II	
molecule	guest diam (Å)	5 ¹²	5 ¹² 6 ²	5 ¹²	5 ¹² 6 ⁴
CH ₄	4.1	0.855	0.744	0.868	0.655
C ₂ H ₆	5.5	1.08	0.939	1.1	0.826
C ₃ H ₈	6.3	1.23	1.07	1.25	0.943
<i>i</i> -C ₄ H ₁₀	6.5	1.27	1.11	1.29	0.976
<i>n</i> -C ₄ H ₁₀	7.1	1.39	1.21	1.41	1.07

Table 1. Ratio of molecular diameters to cavity diameters for natural gas hydrates formers (modified from Sloan, 1998b).

Another factor that needs to be considered is the pressure at which the clathrates are formed- the quantity of small gas molecules incorporated depends strongly on the pressure (Berecz and Balla-Achs, 1983).

Clathrate structures are determined mainly by the size of the gas molecule, but other properties of the guest molecules play a minor role in determining the structure that might occur. The most important rotation inhibition interactions between guest molecules (in adjacent cages) are the dipole-dipole interactions, but they are a relatively minor factor (Sloan, 1998a). The weak van der Waals interactions between a guest molecule and the water molecules in the cage will position the guest molecule in its most stable position- where the repulsion between the H atoms (if present in the guest molecule) and adjacent water molecules is at a minimum (Gough et al., 1974). Methane, the most common natural

gas hydrate guest molecule has no dipole moment and therefore, the dipole moment in this case has no effect on which cage the methane will occur in.

The guest species may be either an atom or a molecule, and can be up to a maximum size in a certain cage, depending on the limiting size of cage available. The interaction between the host and guest is usually associated with weak Van der Waals forces. There may be limited translational motion for a sufficiently small guest, such as an atom, but if the guest is larger, such as a molecule there should be some fairly free rotation vibrational motion (Andersson and Ross, 1983). The rotational freedom is probably due to the fact that the sums of the cage water dipoles effectively cancel near the center of the cage (Sloan, 1998a). Most guest molecules prefer to be located off-center near the cavity wall, particularly at temperatures below 77K (Sloan, 1998a).

For example, Tse et al. (2001) described a Xe atom with local vibrations due to rattling motions in a hydrate cavity, which he measured with incoherent inelastic neutron scattering. As the xenon atom approaches the wall of the cavity, a repulsive interaction becomes dominant, and the water molecules near the xenon atom are pushed outwards slightly to alleviate the unfavorable interaction (Tse et al., 2001). CH₄ molecules in the clathrate cavities rotate almost freely, but the amplitudes of translational motions are small (Tse et al., 1997).

Chapter 2

GAS HYDRATE SYNTHESIS APPARATUS AND NEUTRON DIFFRACTION RESULTS

2.1 Motivation

The slow kinetics (many hours to weeks) associated with clathrate formation precludes the *in situ* synthesis of samples for neutron scattering. *Ex situ* synthesis does not tie up a diffractometer during sample preparation, allows for better control of synthesis conditions, and offers the possibility of sample quality verification prior to the collection of neutron data. For most clathrate measurements by neutron scattering, *ex situ* synthesis is the only practical route.

The gas hydrate laboratory at the United States Geological Survey (USGS), Menlo Park, California, has been successfully synthesizing gas hydrates for over twenty years. Their gas hydrate apparatus has synthesized pure, polycrystalline gas hydrates for their laboratory's research, as well as other researchers worldwide. This institution was very generous in providing access to their facility for sample synthesis, as well as all the necessary information to build a similar synthesis apparatus at Los Alamos National Laboratory.

2.2 USGS gas hydrate synthesis apparatus

The formation of gas hydrates is a surface phenomenon, so the basic principle is to introduce the gas of interest to finely ground "seed" ice (finely ground increases the surface area for the gas to react) and heat the sample to drive the kinetics of formation. Other

methods are possible; an excellent and comprehensive review of a variety of methods and fabrication apparatus is given by Sloan (1998, Chapter 6).

The starting seed ice is made by freezing triply distilled H₂O or D₂O in a steel container with heating tape to reduce the trapping of gas bubbles into the ice block. The ice is then crushed, ground, and sieved to 180-250 μm grain size and packed into an indium sleeve at approximately 40% porosity. Discs are placed over each end to prevent displacement of the ice during the experiment. The grinding, sieving, and packing of the ice needs to be carried out in a freezer to keep the sample cold (Figure 7). The indium sleeve is used as a barrier between the ice and the stainless steel pressure vessel (pressure vessel herein) for ease of removal at the end of the experiment. The ice sample is then placed into a pressure vessel, connected to the high-pressure gas lines, and thermocouples are inserted into the bottom of the sample to carefully monitor the temperature during synthesis. The pressure vessel is submerged in a liquid bath at a pre-cooled temperature ($\sim 250\text{K}$) (Figure 8, 9a).

After repeated purging to remove contamination from previous experiments and/or oxygen, the sample vessels are evacuated. The gas of choice is introduced slowly in the sample vessel. In general, the gas must be pre-cooled to avoid melting the ice when the vessel gets filled to the pressure required for synthesis. This pressure varies from gas to gas, as well as with the starting temperature for the synthesis experiments. For example, Stern et al. (2000) synthesized methane hydrate at a starting temperature and pressure of 250K and 35 MPa using methane gas. Once the gas is introduced at the proper pressure, the sample is isolated from the gas source to monitor gas intake via the drop in pressure. By heating the

ice and gas mixture slowly through the melting point of ice, the mixture slowly converts to gas hydrate (Figure 9b).



Figure 7. The inside of the sample preparation freezer at the USGS gas hydrate lab. Note the triply-distilled ice for the starting materials in freezer bags, top left, blender for freezing in the bottom left, and two sieves center and right-center.

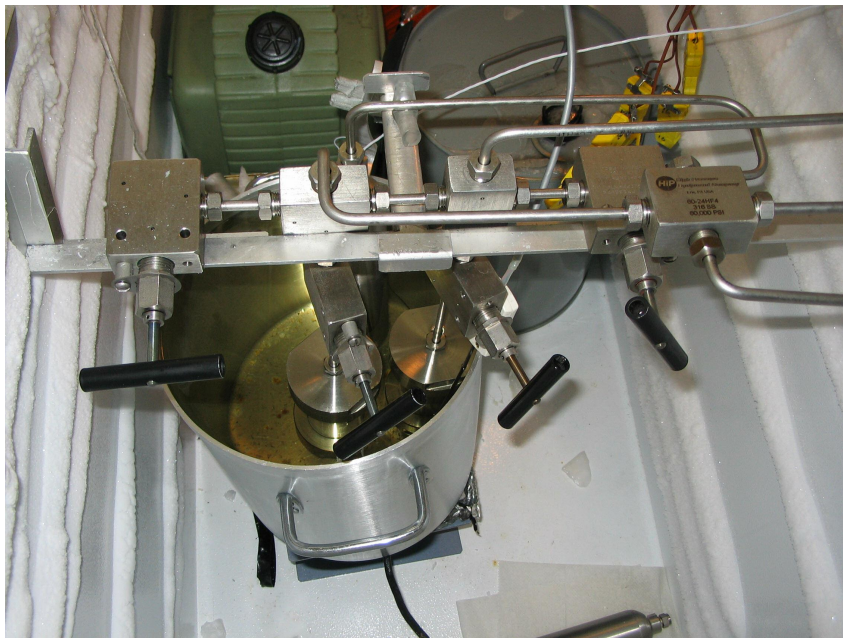


Figure 8. Photograph of the gas hydrate synthesis apparatus at the USGS. A conventional household freezer is used to cool the fluid that surrounds the two suspended samples and the gas reservoir. A heating element under the bath controls the temperature of the fluid.

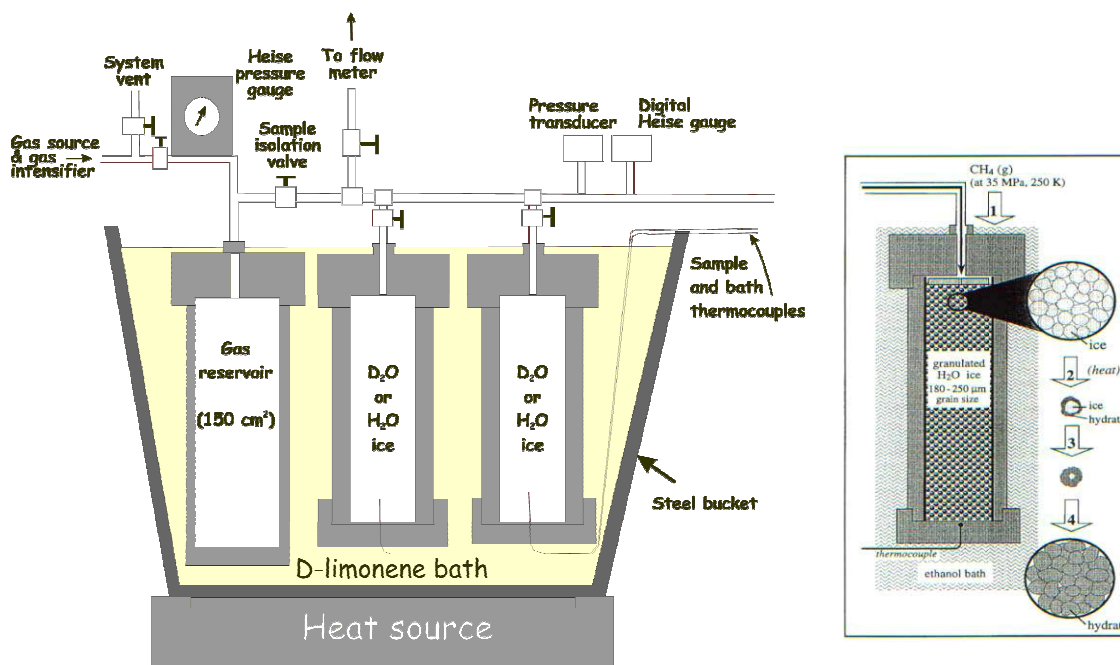


Figure 9a. Schematic drawing of the USGS gas hydrate synthesis apparatus (modified from Stern et al., 2000); 9b. Schematic drawing of the reaction between the ice and gas.

Data-acquisition software monitors and records the P-T conditions throughout each run (Figure 10a). By looking at the P-T record, one can determine if the ice has been converted to gas hydrate completely. Indeed, there is a freezing anomaly at 273K (Figure 10a, arrow denoting the anomaly): the pressure and temperature readings are discontinuous due to unreacted and supercooled water suddenly freezing to form ice. After full conversion to gas hydrate, the sample chambers are vented, but the pressure must remain within the gas hydrate stability zone. The sample vessels are disconnected from the gas handling system and submerged into liquid nitrogen to quench them. Immediately before this operation, the

pressure in the vessel is relieved to ensure that any remaining free gas will not liquefy in the sample chamber. Allowing methane (for example) to freeze as the sample is cooled to liquid nitrogen temperature (77 K) results in a material that is mildly explosive and very difficult to work with when re-warmed (Stern et al., 2000). Following the quenching procedure, the pressure vessels are opened, and the indium sleeve (Figure 10b) containing the gas hydrate is stored for future experiments in a liquid nitrogen dewar.

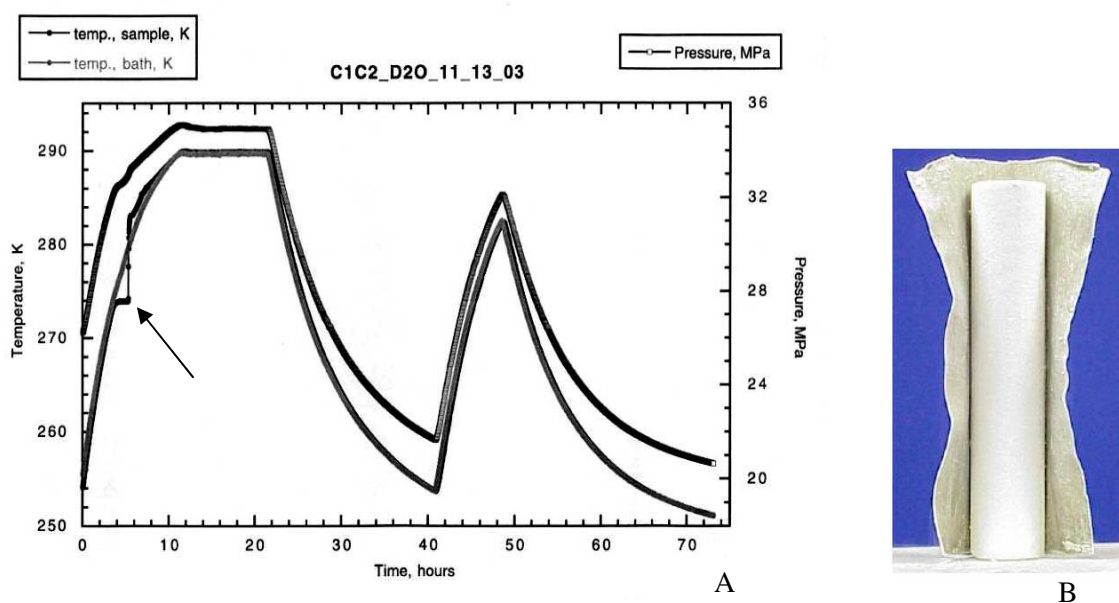


Figure 10a. P-T-t plot of a synthesis run of a 90% methane- 10% ethane (starting) gas hydrate at the USGS. Note the thermal anomaly at 273K due to the supercooled water freezing abruptly with an error pointing out the freezing anomaly. 10b. Fully converted gas hydrate from synthesis apparatus in indium sleeve (from Stern et al., 2000).

Sample #1: The first sample synthesized in these experiments was with a methane-ethane mixture (starting ratio 80:20), one sample vessel was equipped with a conventional indium jacket (132.10 mm). Two ice-filled vanadium-cans were placed in the other vessel to

see if a sample could be synthesized directly in a neutron sample holder. This vessel had a half-sized indium jacket (71.5 mm) only. The indium sleeve was packed with 26.81 g of D₂O ice. The two cans contained 2.17 g and 1.72 g of D₂O ice, respectively, and the half-sized indium jacket was filled with 24.79 g of D₂O ice.

Sample #2: The second sample synthesized at the USGS was a methane-ethane mixture gas (starting ratio 90:10), with the same sample can and indium sleeve arrangement as the first run. The large indium jacket contained 29 g of D₂O ice initially. The half-sized jacket had 14.89 g D₂O ice, and the two cans contained 2.22 g and 2.08 g of ice.

Sample #3: The third sample that was synthesized contained only ethane gas, which took over three weeks to complete. For this sample there were two full-sized indium sleeves in the sample vessels, with 29.11 g and 26.08 g of D₂O ice.

Many variables can affect the gas uptake into the hydrate structure. After each synthesis, gas chromatography and mass spectroscopy (GC/MS) were used to determine the relative percentages of gases (for multi-component gas systems) and to determine the sample stoichiometry. Typically there will be a noticeable variation in the relative gas compositions in the final gas hydrate compared to the starting gas mixture (for example, the 90%-10% starting methane-ethane source gas produces a clathrate of composition of 82.9%-17.1% methane-ethane in the final product, Figure 11). To determine the composition of the final product, a piece of the synthesized gas hydrate is decomposed (melted), and the gas is collected in a lecture bottle. This sample is then measured with gas chromatography, and the results are compared with two standards of methane and ethane gases. The results of the first

sample were methane 77.93% ethane 22.07% (norm.) and the second - methane 82.93% ethane 17.07% (norm.).

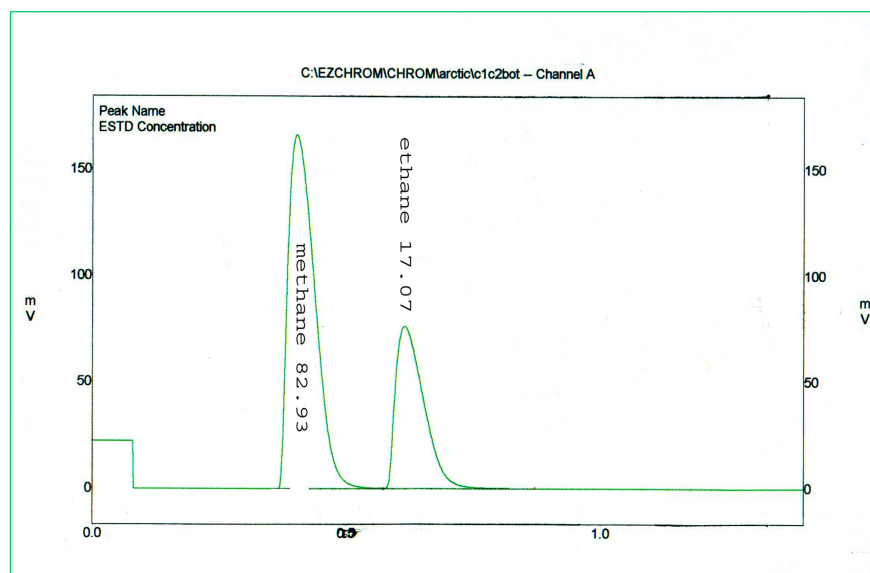


Figure 11. Final gas concentrations of the second sample (methane/ethane) in a gas hydrate run at the USGS Organic Geochemistry Mass Spectrography Laboratory.

During a second visit to the USGS, a second sample of ethane hydrate with D₂O ice was synthesized. The two sample vessels contained 24.17 g and 20.20 g of ice, respectively. The second sample synthesized at the USGS contained 50% methane and 50% ethane (by weight), with 24.15 g of D₂O ice in the large indium sleeve; the second vessel has a half-size jacket with 20.12 g of ice and two vanadium cans with 2.56 g and 2.26 g of D₂O ice. Gas chromatography of the synthesized samples showed gas concentrations as follows- the top of the sample was 47.25% methane and 52.73% ethane (with 0.02% CO₂); the bottom was 47.18% methane and 52.82% ethane, demonstrating a homogeneous concentration

throughout the sample. The third sample was a 50%:50% methane-ethane sample with H₂O seed ice. The gas chromatography results were similar to the D₂O sample.

2.3 Low-Temperature Scanning Electron Microscopy (LTSEM)

The USGS has a Low-Temperature Scanning Electron Microscope (LTSEM) for gas hydrate research. The ability to analyze low-temperature samples is a fairly new and relatively unique technique that can study the gas hydrate pore and grain interaction and has been used fairly extensively to look at the differences between natural and synthetic samples (Stern et al., 2004; Suess et al., 2002).

In preparation for LTSEM, a small section of each sample (0.75 x 0.75 x 0.5 cm) was mounted with clamps in a brass sample holder. The sample holder has a thin bottom to maintain close thermal contact with the stage on which it is mounted. Samples were quickly transferred in liquid nitrogen (LN₂) to the Gatan Alto 2100 low-temperature preparation chamber (evacuated and pre-chilled below 100 K), which was in turn attached to a LEO 982 field emission SEM. A scalpel was used to fracture the sample and remove the surface of the hydrate. This step is necessary to remove any deposits of condensation from atmospheric water, as well as any material that may have reacted with the atmosphere during transfer to the preparation chamber of the LTSEM.

After the sample was fractured in the preparation chamber, it was transferred under vacuum directly into the SEM scanning chamber. The sample temperature was continuously monitored by thermocouples placed in the sample stages of both the preparation chamber and the SEM chamber. Imaging was conducted at temperatures below 105 K and vacuum below

10^{-5} mbar, using low voltage (≤ 3 kV) to minimize sample alteration or beam damage to the sample surface (Stern et al., 2004).

LTSEM images were collected for several of the samples synthesized during the two USGS visits. Most samples presented no particular difficulties in terms of manipulation and mounting for microscopy. The ethane sample, however, was very reactive and difficult to get into the SEM chamber. There was a large amount of frozen ethane in the sample. The sample warmed up between the initial brass sample holder mounting and evacuation of the preparation chamber steps and became explosive. All samples decomposed slightly (Figure 12) which resulted in a porous ice texture. Nonetheless, where the sample was cleaved, some grain features could be seen. The gas hydrate grain features in Figure 13a,b are similar to images in Stern et al. (2004) and Staykova et al. (2003), and are attributed to the outlines of the original ice grains. The original porosity is reduced by the sintering that takes place during synthesis to form a macroscopically cohesive sample (Staykova et al., 2003).

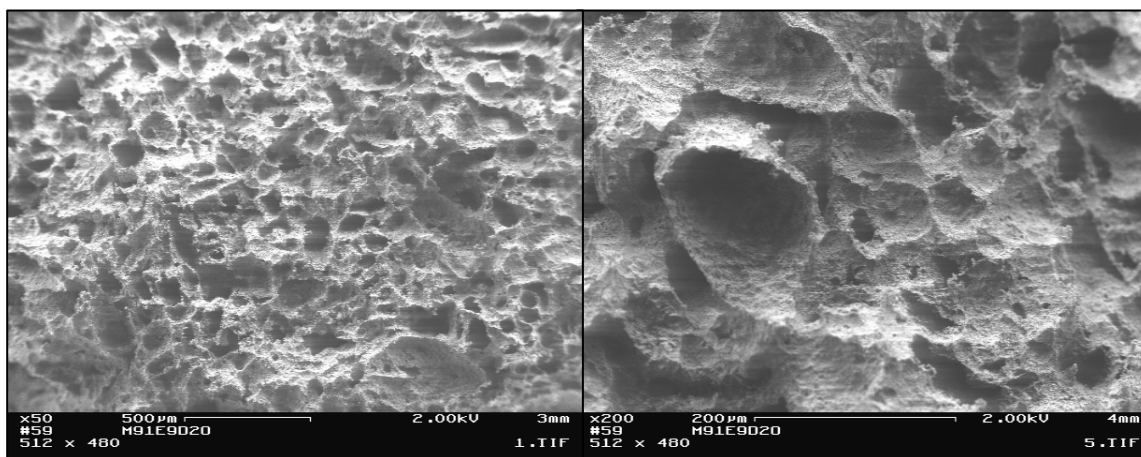


Figure 12. Examples of dissociation features of the methane-ethane hydrate with the LTSEM; scale is shown in bottom of the photos.

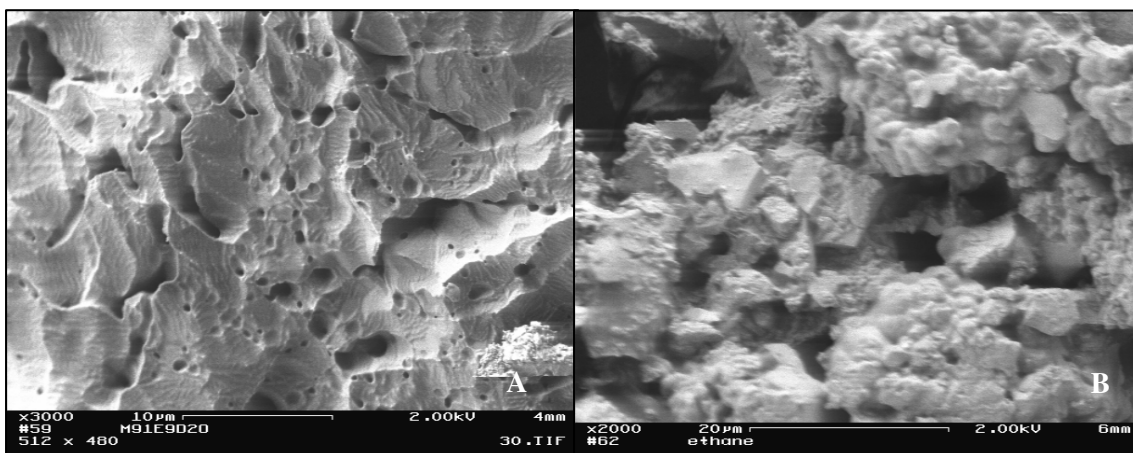


Figure 13a. Cohesive methane-ethane hydrate sample with porosity; 13b. granular ethane hydrate with individual crystal morphology shown. Scale of images shown on photos.

2.4 Methane-ethane hydrate

Pure ethane and pure methane gases form structure I hydrates due to cage stability issues- the methane molecule can fit in the small and large cages of the sI structure, whereas ethane can only fit in the large $5^{12}6^2$ cage due to its larger size. It was assumed for modeling that the combination of the two gases would also form a structure I clathrate (Holder and Hand, 1982). Uchida et al. (2002) show that below 2% and above 22% the C_2H_6 molar fraction, structure I clathrate forms. Structure II is obtained with hydrates with 2-11% C_2H_6 . Structure I and II co-exist for 12-22% molar fraction C_2H_6 .

Subramanian et al. (2000a) and Ballard and Sloan (2000) showed that at 274.15 K the equilibrium hydrate structure for methane and ethane changed from structure I to structure II at approximately 72 mole percent methane in the water-free gas phase (Figure 14).

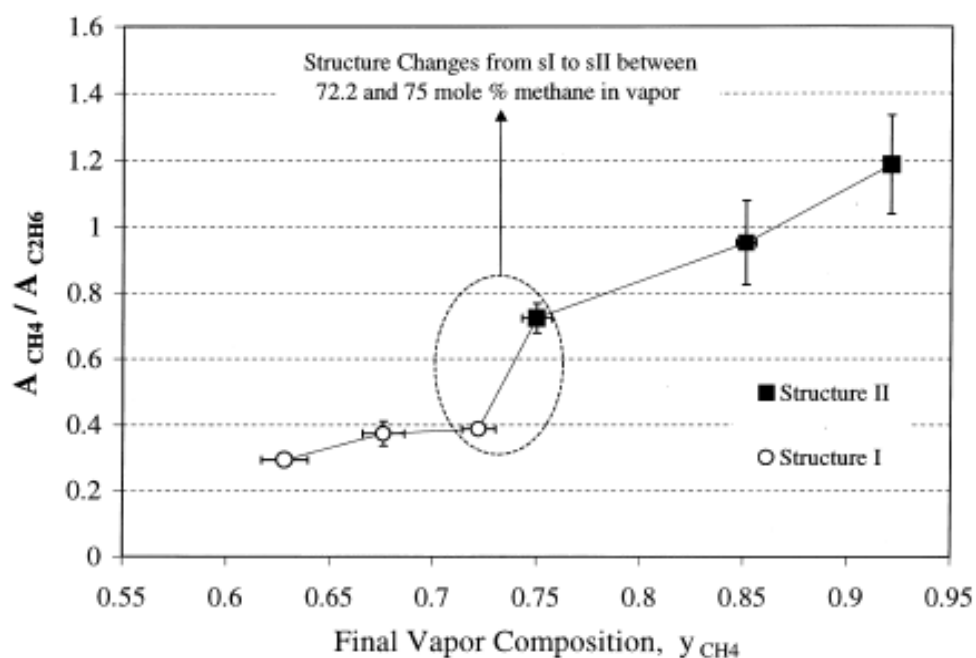


Figure 14. Predicted composition region for the structural transition to occur (Subramanian et al., 2000a).

Subramanian et al. (2000a) used research grade (99.92%) methane and C.P. grade (99%) ethane. Their mixtures were gravimetrically prepared in stainless steel containers and were thermally agitated using an infrared source before reaction in pyrex capillary cells. The authors do not report measuring the final gas concentrations in the hydrate, only the starting gas concentrations. Ballard and Sloan (2000) do not discuss the details of their sample preparation procedure, but one can assume that they followed procedures similar to Subramanian et al (2000b) because they work in the same laboratory. Uchida et al. (2002) report the gas composition of the initial feed gas (determined by the C_2H_6 concentration) and

the gas concentration in equilibrium with the hydrates after the complete reaction in equilibrium with an on-line gas chromatograph.

2.5 Introduction to neutrons

Neutrons are scattered by the atomic nuclei of the sample, whereas X-rays interact with the electron cloud surrounding the nuclei, so with increasing atomic number, the probability of an X-ray interacting with an electron increases (Figure 15). Since the nucleus of an atom is relatively small (the nucleus is typically 100,000 times smaller than the distance between nuclei), the incident beam has a high penetration depth because the probability of interacting with a scattering center (nucleus) is small (Pynn, 1989). Therefore, neutrons are only weakly scatter once they penetrate the sample. Experimentalists want to use elements that have a high scattering cross section σ , measured in barns (1 barn = 10^{-28} m²) that is equivalent to the effective area presented by the nucleus to the passing neutron (Pynn, 1989). Neutrons do have a mass ($m = 1.675 \times 10^{-27}$ kg), and therefore sizeable momentum; the strength of the neutron-nucleus interaction is represented by the scattering length, b .

The cross section σ , an area, is related to b by the simple relation $\sigma_{\text{tot}} = 4\pi \langle b^2 \rangle$ (where 4π steradians of possible scattered beam solid angle) with the scattering length were half the radius of the nucleus as seen by the neutron (Pynn, 1989). There are two types of scattering that can occur as the neutron interacts with the nucleus- *coherent* and *incoherent* scattering. Coherent scattering (or Bragg scattering) is where the neutron waves interact with the whole sample as a unit so that the scattered waves from different nuclei interfere, which provides information about the sample (crystal structure, motions of the atoms, etc.). With

incoherent scattering, the neutron waves interact independently with each nucleus in the sample so that the scattered waves from different nuclei do not interfere destructively. It occurs in all directions and is generally weak. Therefore, incoherent scattering does not provide crystal structure information about a sample and produces background for diffraction experiments. These incoherent scattering events, however, can exchange energy with the sample; these events allow experimentalists to perform neutron vibrational spectroscopy. The total scattering cross section σ_{tot} of an atom is the sum of the coherent and incoherent scattering cross sections, σ_{coh} and σ_{inc} , respectively (Krawitz, 2001).

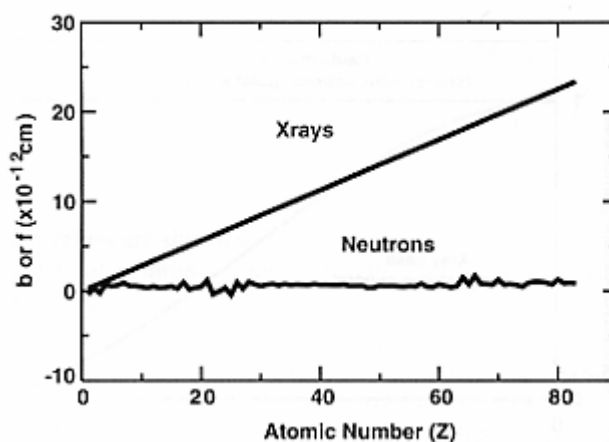


Figure 15. Comparison of atomic number dependence vs. scattering length, b for X-rays and neutrons (Krawitz, 2001).

2.6 Los Alamos Neutron Scattering Center (LANSCE)

The Los Alamos Neutron Science Center (LANSCE) is a pulsed spallation neutron source that uses an 800-MeV linear accelerator system that accelerates both negative hydrogen ions and protons. At the LANSCE facility, there are three experimental areas, the Manuel Lujan Jr. Neutron Scattering Center (Lujan Center), the Weapons Neutron Research

(WNR) facility, and the Proton Radiography Facility (pRad); the experiments discussed within this dissertation that were completed at LANSCE were carried out at the Lujan Center. The Lujan Center uses the 800-MeV H^- beam to produce cold, thermal and epithermal neutrons in the meV-keV range to 17 flight paths around a light-water cooled split-tungsten target (Lisowski and Schoenberg, 2006) (Figure 16). For the clathrate research described in this dissertation at LANSCE, four instruments were used; two diffractometers, the High-Pressure-Preferred Orientation Neutron Diffractometer (HIPPO) and the High-Intensity Powder Diffractometer (HIPD), and two inelastic spectrometers, the Filter Difference Spectrometer (FDS) and the High-Resolution Chopper Spectrometer (Pharos).

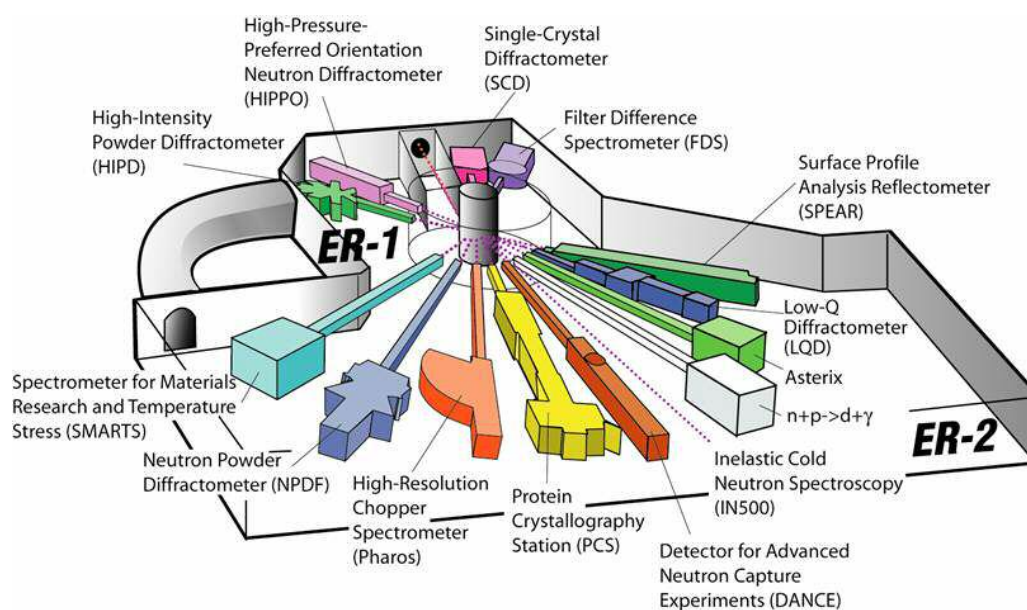


Figure 16. Schematic diagram of the two experimental areas at the Lujan Center, experimental area-1 and -2 (ER-1 and ER-2), where 17 available flight paths surround the tungsten target (figure supplied by LANSCE-Lujan Center).

2.7 Neutron scattering of pre-synthesized samples

Samples were transported to LANSCE in a liquid nitrogen filled dewar for subsequent neutron diffraction experiments on HIPPO in the low-temperature, high-pressure gas hydrate setup and a displax for the vanadium can samples.

2.7.1 HIPPO and ancillary equipment

The High Pressure, Preferred Orientation Diffractometer (HIPPO) is the newest of the diffractometers at LANSCE. It is used for high-pressure and/or high-temperature experiments, textural analysis and general diffraction experiments. The diffractometer achieves very high neutron count rates due to a short (9 m) initial flight path on a high-intensity water moderator. The detector system consists of 1360 ^3He detector tubes arranged in panels on rings of 150° , 90° , 40° , 20° , and 10° diffraction angles around the incident beam direction (Figure 17).

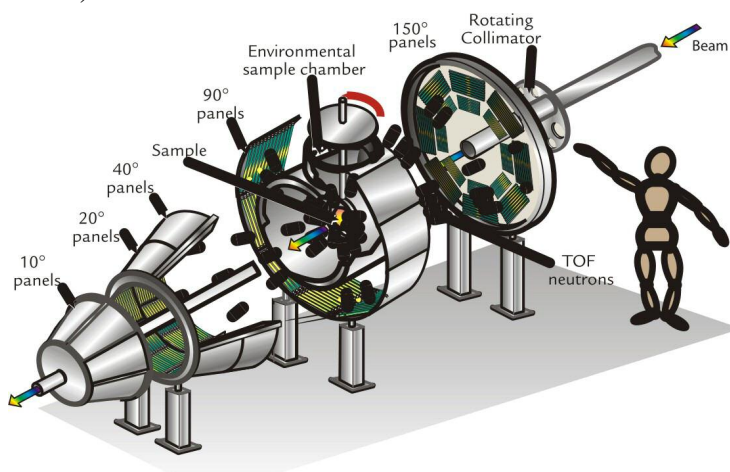


Figure 17. Schematic of the HIPPO chamber, denoting the beam path through the diffractometer, the sample chamber, and the panels of detectors (figure supplied by LANSCE-Lujan Center).

Several different sample environments are needed to do clathrate research due to the complexity of the pressure and temperature conditions at which these samples need to remain for the duration of the experiments. For several experiments a “top-hat” apparatus (Figure 18a) is craned into the instrument with a closed-cycle helium refrigerator (Figure 18b) head that can achieve temperatures below $<10\text{K}$. The sample is then attached via a screw at the end of the cold finger, and diodes are attached to the sample for continuous sample thermometry during the experiment.



Figure 18a) top-hat setup being craned into NPDF (photo courtesy of Thomas Proffen); 18b) typical closed cycle refrigerator for neutron experiments used at LANSCE (from <http://www.arscopy.com/csw204.html>)

A hydrostatic high-pressure and low-temperature apparatus was designed at LANSCE for experiments up to 10 kbar and temperatures from 4 to 300K (Lokshin and Yusheng, 2005). It was used for some of the diffraction experiments discussed below. A significant advantage of this cell that represents an advance over previous designs is the horizontal geometry in which the incident neutron beam travels along the cell axis, which allows for the experimentalist to adjust the sample position to maximize detector illumination (Figure 19a and 19b).

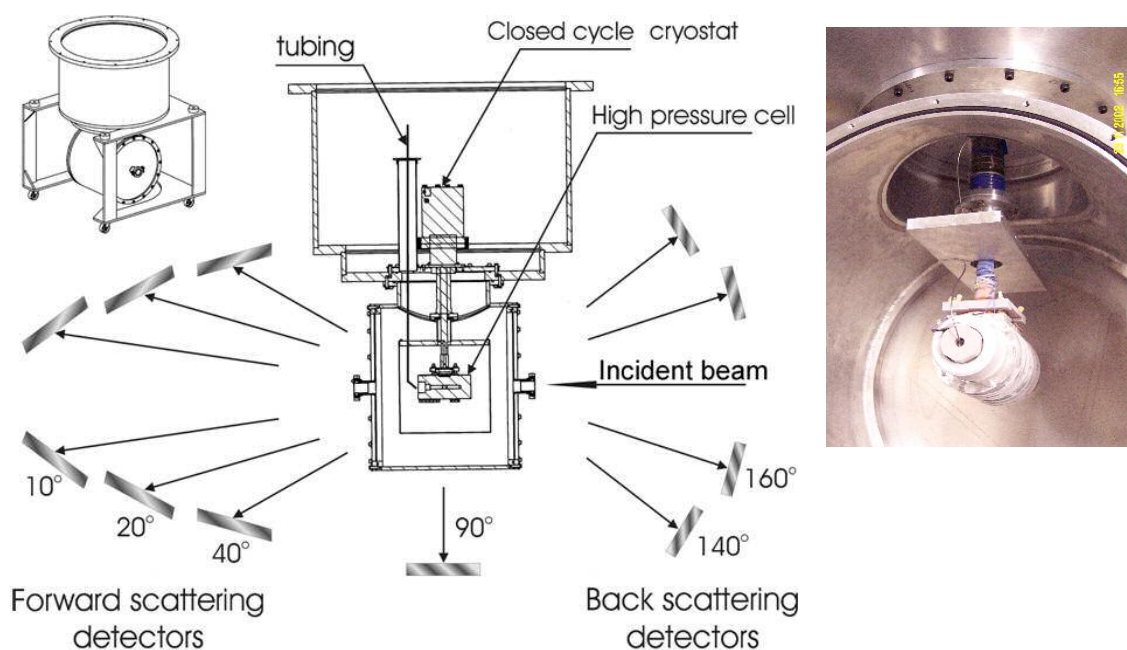


Figure 19a. Schematic general view (top left corner) and the enlarged section view of the setup designed for high-pressure, low-temperature hydrostatic experiments at LANSCE (Lokshin and Zhao, 2005); 19b. photo of internal cell at liquid nitrogen temperatures attached to the closed cycle cryostat (photo courtesy of K.A. Lokshin).

For the samples in the low-temperature, high-pressure setup, pieces of the synthesized gas hydrate were broken off, ground in a liquid-nitrogen cooled mortar and packed in a pre-cooled sample can. The sample can is placed in the cell to minimize displacement of the center of diffraction upon the application of pressure and then attached to the pre-cooled displacer and craned into the HIPPO sample chamber. Data was collected and Rietveld structure analysis was then performed to determine composition with the General Structure Analysis Software (GSAS) (Larson and von Dreele, 1994).

2.7.2 Results methane 77.93% ethane 22.07% (norm.) sample

The 77.93% methane, 22.07% ethane gas hydrate synthesized at the USGS in the indium sleeve was ground and placed into the low-temperature, high-pressure setup, and several diffraction patterns were collected at ambient pressure and 250K. There is a fair amount of ice in the sample, which could have happened during transportation or handling of the sample prior to data collection. The gas hydrate sample is mainly structure I, with a minor amount of structure II present (Figure 20).

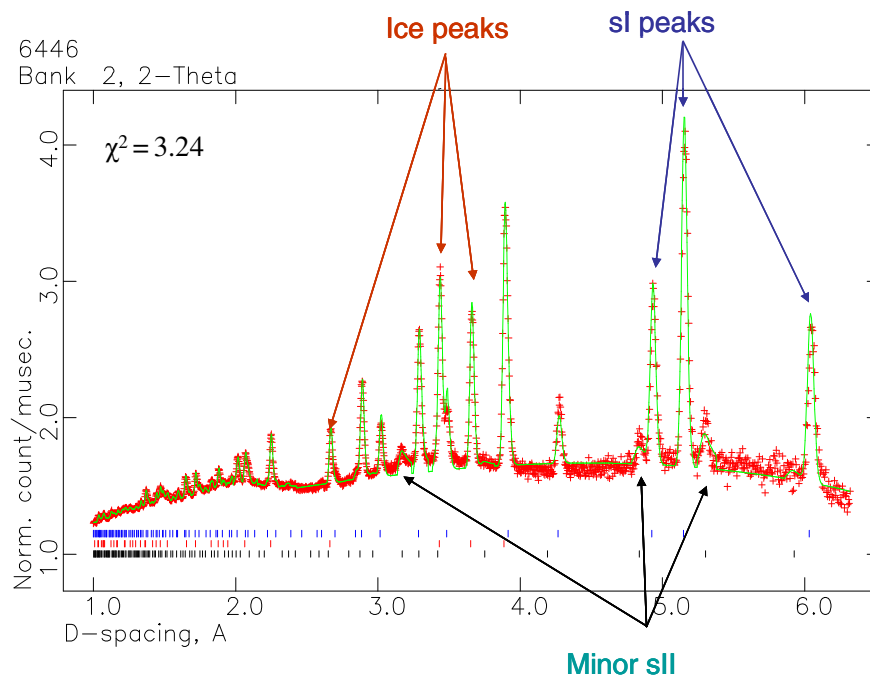


Figure 20. Rietveld LeBail fit (green line) of the three-phase methane-ethane gas hydrate diffraction pattern (red marks) with the $\chi^2 = 3.24$; ticks on the bottom of the figure show the d-spacing positions of the three phases: structure II- black, ice- red, structure I- blue) and some of the major peaks have been identified with arrows for ease of comparison.

2.7.3 Results methane 82.93% ethane 17.07% (norm.) sample

The 82.93% methane, 17.07% ethane gas hydrate synthesized at the USGS in the indium sleeve was ground and placed into the low-temperature, high-pressure setup, and several diffraction patterns were collected at ambient pressure and 250K. There is some amount of ice in the sample, which could of happened during transportation or handling of the sample prior to data collection. The gas hydrate sample is mainly structure I, with a minor amount of structure II present (Figure 21).

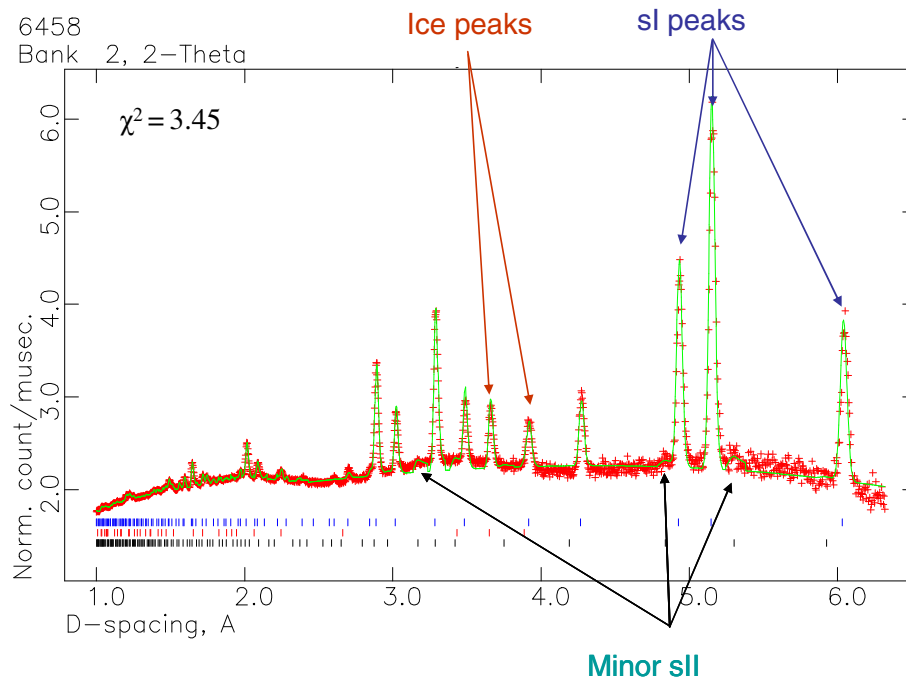


Figure 21. Rietveld LeBail fit (green line) of the three-phase methane-ethane gas hydrate diffraction pattern (red marks) with the $\chi^2 = 3.45$; ticks on the bottom of the figure show the d-spacing positions of the three phases: structure II- black, ice- red, structure I- blue) and some of the major peaks have been identified with arrows for ease of comparison.

2.7.4 Results 50% methane, 50% ethane sample

As predicted and reported in the literature (Ballard and Sloan, 2000; Subramanian et al., 2000a; Subramanian et al., 2000b; Uchida et al., 2002 etc.), the 50%-50% methane-ethane hydrate sample should form a sI clathrate (Figure 22), but unfortunately in our results the sample is mainly ice (approximately ~80%) with sII clathrate, and with minor sI clathrate. This is the first reported neutron diffraction pattern of the 50:50 methane-ethane hydrate.

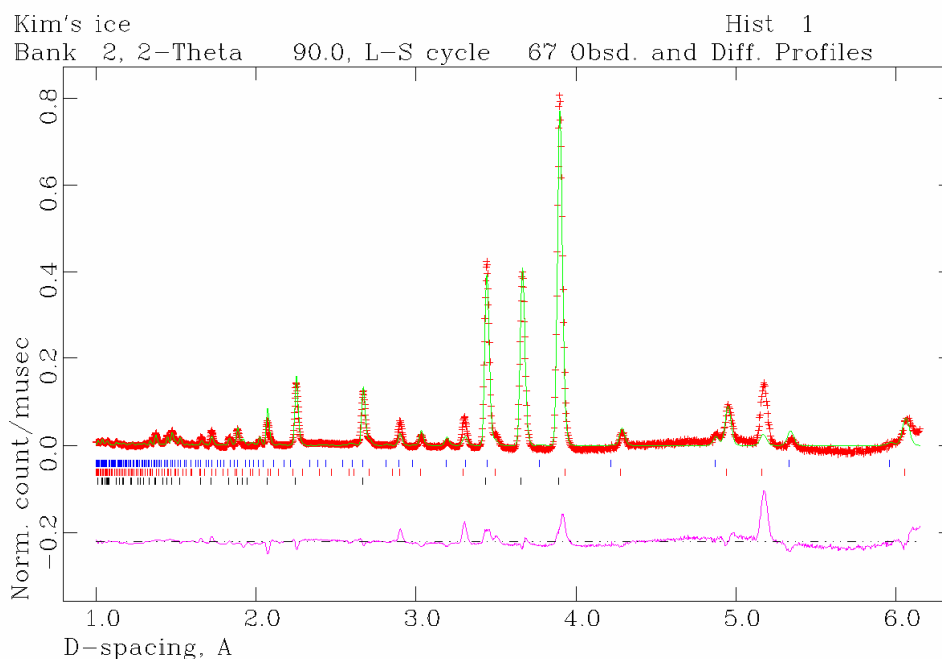


Figure 22. Rietveld fit (green line) of the 50:50 methane-ethane gas hydrate diffraction pattern (red marks); ticks on the bottom of the figure show the d-spacing positions of the three phases: structure II- black, ice- red, structure I- blue). Some of the major peaks have been identified with arrows for ease of comparison.

2.7.5 Results 100% Ethane gas hydrate sample

As predicted and reported in the literature (Subramanian et al., 2000a, 2000b; Uchida et al., 2002, Sloan, 1998, Ballard and Sloan 2000, etc), the 100% ethane hydrate sample forms a sI clathrate (Figure 23). A small amount of ice is present and may be due to minor ethane hydrate decomposition during sample preparation and handling after synthesis. This is the first reported neutron diffraction pattern of ethane hydrate.

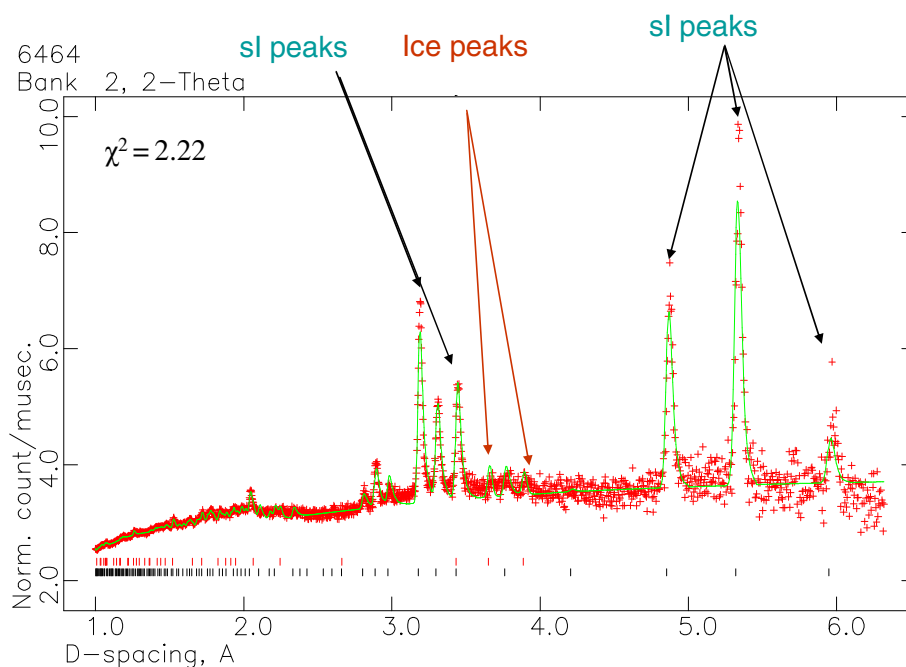


Figure 23. Rietveld LeBail fit (green line) of the two-phase ethane gas hydrate diffraction pattern (red marks) with the $\chi^2 = 2.22$; ticks on the bottom of the figure show the d-spacing positions of the three phases: structure I- black, ice- red) and some of the major peaks have been identified with arrows for ease of comparison.

2.8 Los Alamos gas hydrate apparatus

After two extended visits to the USGS gas hydrate laboratory in Menlo Park, California, it was determined that the cost and time benefit of reproducing a similar Laboratory in Los Alamos, New Mexico was attractive. Design of the gas hydrate synthesis apparatus started in 2005, based on the USGS synthesis laboratory design, to which were added some capabilities that were uniquely needed for Los Alamos' gas hydrate and hydrogen storage projects (Figure 24).

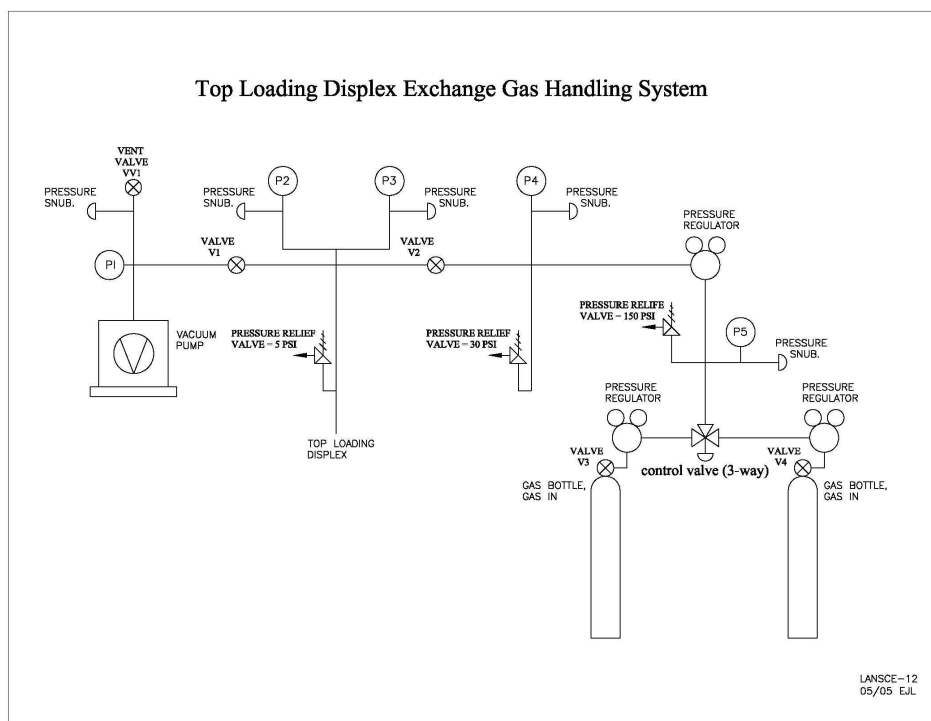


Figure 24. Early conceptual design of the gas hydrate gas handling system at the Los Alamos Neutron Scattering Center.

Due to strict safety regulations at the National Laboratory, most of the apparatus' parts were purchased commercially from a certified vendor. The gas hydrate apparatus at Los Alamos can mix up to four gases at once. These gases are fed through a Dynablender™ Mass Flow Control box so that the operator can choose the appropriate gas ratios. The gas mixture is stored in a steel vessel. The high-pressure lines are evacuated via a TriScroll™ 600 Dry Scroll Vacuum Pump connected to the line at valve 6 (refer to Figure 25 for valve numbering). Once the line has been evacuated (which can be determined by the vacuum gauge), valve 6 is closed to seal off the vacuum pump. The gas is then introduced up to valve 7, with the option of increasing the pressure of the gas past what the gas cylinder can

provide at valve 2, which is a 3-way valve for the gas intensifier to be included. There is a redundancy in the pressure valving on this part of the apparatus: there is a digital pressure gauge on valve 2, and an analogue pressure gauge before valve 7 for safety, in case one gauge fails.

With minor modifications, samples are prepared according to the USGS method (pre-ground D₂O or H₂O ice, sieved and placed into an indium tube at 40% porosity) suspended from the high-pressure lines at valves 8 and 9. The sample vessels are submerged into a 4:1 water/ethylene glycol bath in the Cole-Parmer™ low-temperature bath, supported on the bottom by a fabricated Al-block for stability and to minimize stress on the high-pressure line. Once the proper pressure has been reached, valve 7 is opened (with 10 closed, the vent line), and the gas is introduced into the two identical pressure vessels (Figure 26). Each vessel has its own pressure gauge to monitor the pressure, and a thermocouple is placed through the bottom of the cell to monitor the internal sample temperature.

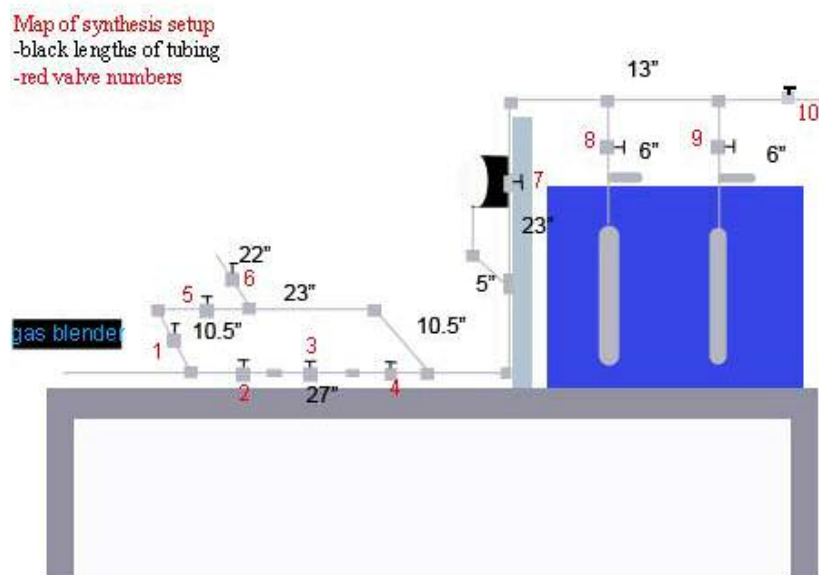


Figure 25. Schematic diagram of the gas hydrate synthesis apparatus with valve numbers and lengths of tubing.

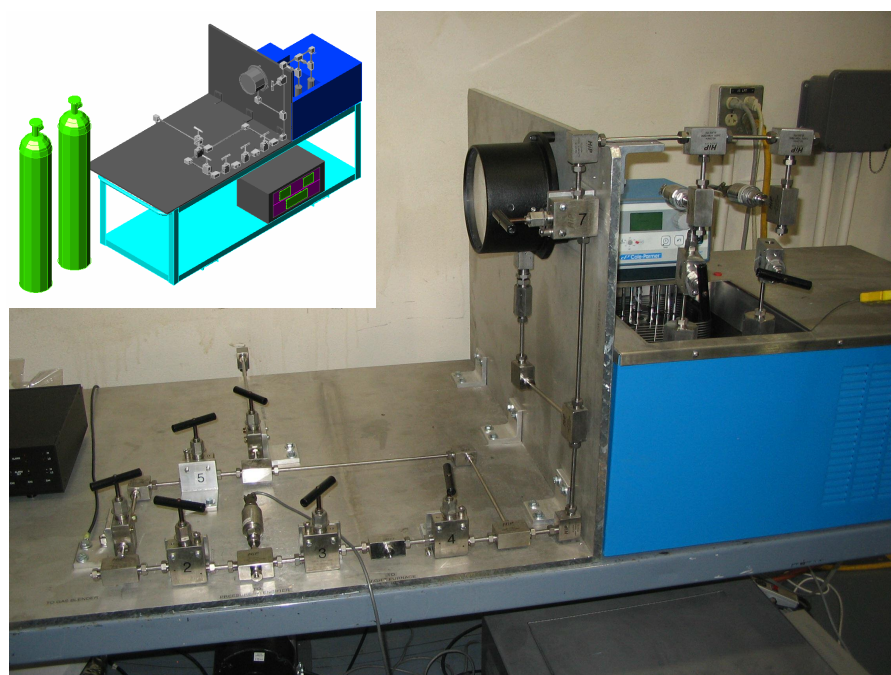


Figure 26. Picture of gas hydrate synthesis apparatus at LANSCE, inset- schematic diagram of final gas hydrate synthesis apparatus at LANSCE.

A LabVIEW interface (to monitor P-T-t) was designed over a period of 12 months to control the low-temperature bath. The interface allows the user to choose the synthesis conditions and upload them to the controller box on the low-temperature bath. The interface then monitors the digital pressure gauges, the thermocouple readouts and the temperature of the ethylene glycol:water fluid in the bath (Figure 27). Once the run is completed, the LabVIEW interface writes the data to an Excel spreadsheet for future data processing of the condition of formation.

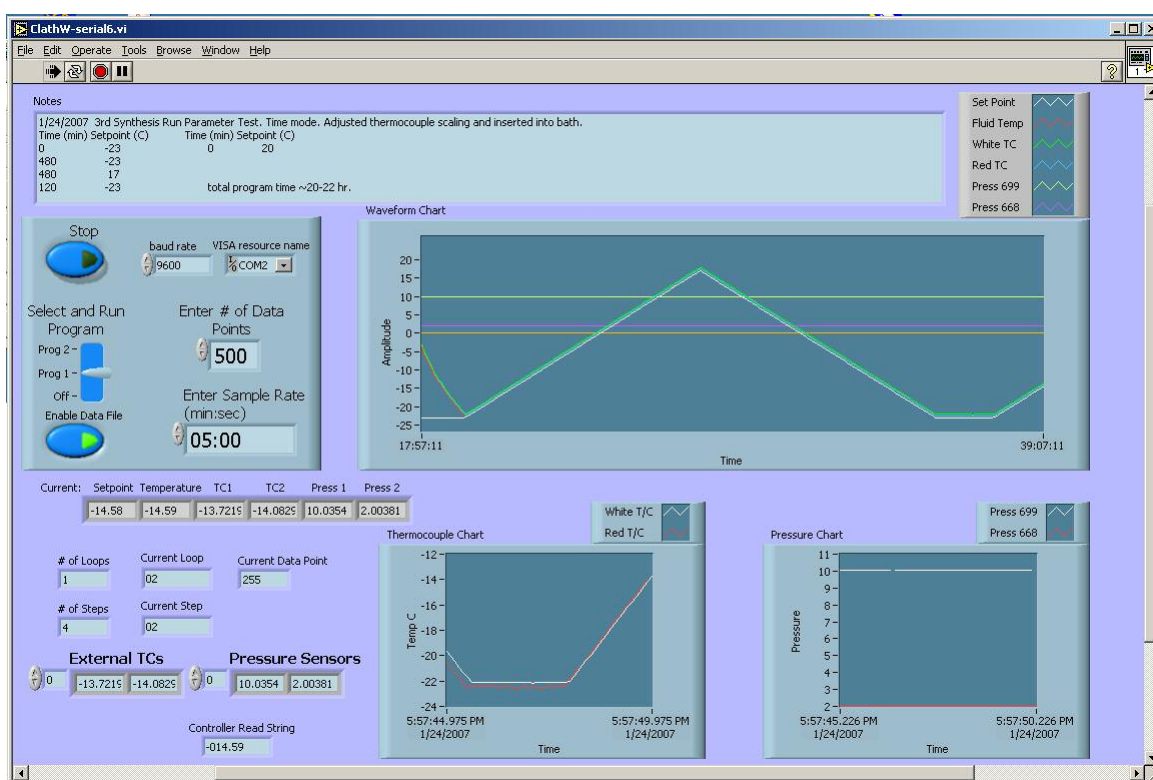


Figure 27. LabVIEW front panel for gas hydrate syntheses at Los Alamos.

Chapter 3

INELASTIC NEUTRON STUDIES OF TETRAHYDROFURAN CLATHRATE WITH HYDROGEN

3.1 Introduction

Fossil fuels in the form of coal, oil, and natural gas have powered the technology and transportation networks since the industrial revolution that began at the turn of the 18th century. Increasing demands for this non-renewable resource puts enormous strain on the environment. The world's demand for energy is projected to double by 2050 in response to population growth and the industrialization of developing countries (Hoffert et al., 1998). One promising alternative to fossil fuels is hydrogen- through its reaction with oxygen; hydrogen releases energy in heat engines or in fuel cells, and water is its only by-product. Although hydrogen is the most abundant element on the surface of the Earth (mainly due to water), less than 1% is present as molecular hydrogen gas H₂. It occurs in chemical compounds such as water or hydrocarbons that must be chemically transformed to yield H₂ (Schlapbach and Zuttel, 2001). To further complicate the issue, H₂ storage options are limited- cylinders of liquid H₂ and high-pressure gases are possible for stationary consumption of hydrogen in large plants that can accommodate large weights and volumes. Meeting non-stationary requirements such as the volume restrictions in cars and trucks, require that hydrogen be stored at densities higher than its liquid density, and a hydrogen

storage material must be found (Figure 28). The non-stationary storage of hydrogen for vehicles may dramatically influence the vehicle's cost, range, performance, and fuel economy, as well as the investment requirements, energy use, and potential emissions of a hydrogen refueling infrastructure (Berry and Aceves, 1998).



Figure 28. Volume of 4 kg of hydrogen compacted in different ways, with size relative to the size of a car (Schlapbach and Zuttel, 2001).

3.2 Previous work

Storage of hydrogen in molecular form within a clathrate framework has been one of the suggested methods for storing hydrogen fuel safely, but pure hydrogen clathrates $\text{H}_2(\text{H}_2\text{O})_2$ form at high pressures. The $\text{H}_2(\text{H}_2\text{O})_2$ clathrate, synthesized at 200–300 MPa and 240–249 K, can be preserved to ambient P at 77 K and holds 50 g/liter hydrogen by volume or 5.3 wt % (Mao and Mao, 2004). It was originally thought that hydrogen molecule was too small to stabilize the clathrate structure, but with the small cages doubly occupied and the large cages quadruply occupied by hydrogen molecules, the hydrogen clathrate is stable

(Figure 29a-c). The extremely high pressures to form a pure hydrogen clathrate has made it an impractical solution for hydrogen storage.

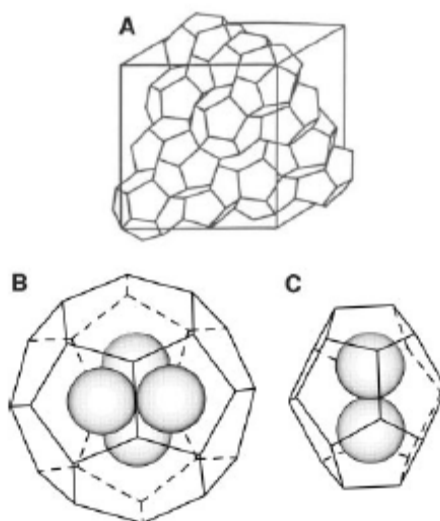


Figure 29a) The sII crystal structure consisting of $5^{12}6^4$ and 5^{12} cages; b) the tetrahedral cluster of four hydrogen molecules in the $5^{12}6^4$ cage; c) a cluster of two hydrogen molecules oriented towards opposite pentagonal faces in the 5^{12} cage.

Lokshin et al. (2004) performed neutron diffraction experiments at LANSCE on hydrogen clathrate at different pressures and temperatures and found that the number of D_2 molecules and their distribution in the clathrate structure depend on temperature and pressure. The large cage was found to be occupied by four tetrahedrally arranged D_2 molecules, with each molecule oriented toward the centers of the hexagons of the cages, but the maximum occupancy of the small 5^{12} cage was determined to be a single hydrogen molecule (Figure 30).

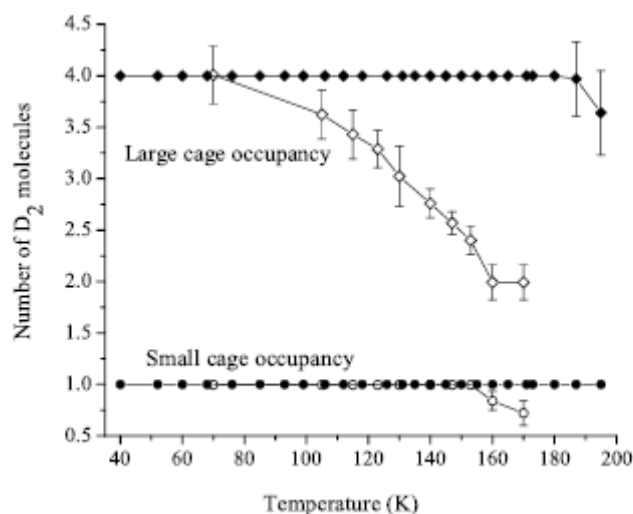


Figure 30. Temperature dependence of D₂ occupancy in the large (diamond symbols) and small (circle symbols) cages of the hydrogen clathrate hydrate structure. Open and filled symbols represent data obtained at ambient and high (~ 2 kbar) pressures, respectively. Data points with no error bars represent the values, which were fixed in the final refinements but were refined in the range 3.8(2) – 4.2(2) for the large cage and 0.9(1) – 1.1(1) for the small cage in the initial refinements. No significant correlation between large and small cage occupancy parameters was observed (Lokshin et al., 2004).

Florusse et al. (2004) reported a binary clathrate of H₂O + H₂ + THF (tetrahydrofuran, Figure 31) that was stable at low pressures and relatively high temperatures (above the freezing point of ice) that renewed the interest of clathrates as a possible hydrogen storage material. The THF molecule stabilizes the large 5¹²6⁴ cage of the sII clathrate, and the hydrogen molecule stabilizes the 5¹² cage. But with the THF molecule occupying all of the large 5¹²6⁴ cages, the hydrogen storage capacity of this hydrate (2.1 wt% H₂) is well below the Department of Energy (DOE) storage targets (Table 2).

		H ₂ wt. %
DOE target	2005	4.5
DOE target	2010	6
DOE target	2015	9

Table 2. Comparison of molecular compounds with Department of Energy (DOE) hydrogen storage targets (modified from Mao and Mao, 2004).

Lee et al. (2005) reported that by “tuning” the amount of THF in the large cages, you can increase the amount of hydrogen stored in the hydrate. In order to increase the hydrogen content of the hydrate, the hydrogen guest must also enter the large cage, so they carried out several experiments by reducing the amount of THF in the structure from 5.56 mol% to 0.1 mol% (Table 3) and thereby increasing the hydrogen storage of the material up to ~4 wt% at modest pressures (Figure 32).

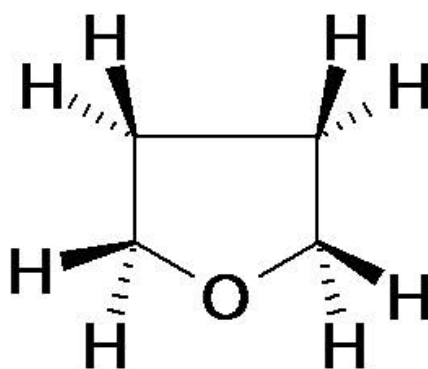


Figure 31. Sketch of a tetrahydrofuran molecule (C₄H₈O) the oxygen has two lone pairs of electrons sticking out from the ring. These electron pairs represent a large electronic density and make it easy for THF to participate intermolecular bonding, e.g., via hydrogen bonding.

Mol% THF (starting soln)	H ₂ :THF mole ratio in hydrate		Max wt% H ₂ in hydrate
10	4		2.09
5.56	4	III	2.09
4	3.44		1.8
2	3.36		1.76
1.5	4.03		2.09
1	4.52	II	2.24
0.5	8.35		3
0.2	17.63		3.8
0.15	23.1	I	4.03
0.1	0		0

Table 3. Mol % THF (starting solution) vs. H₂:THF mole ratio in the hydrate vs. max wt% H₂ in the hydrate for the three regions as outlined by Lee et al. 2005.

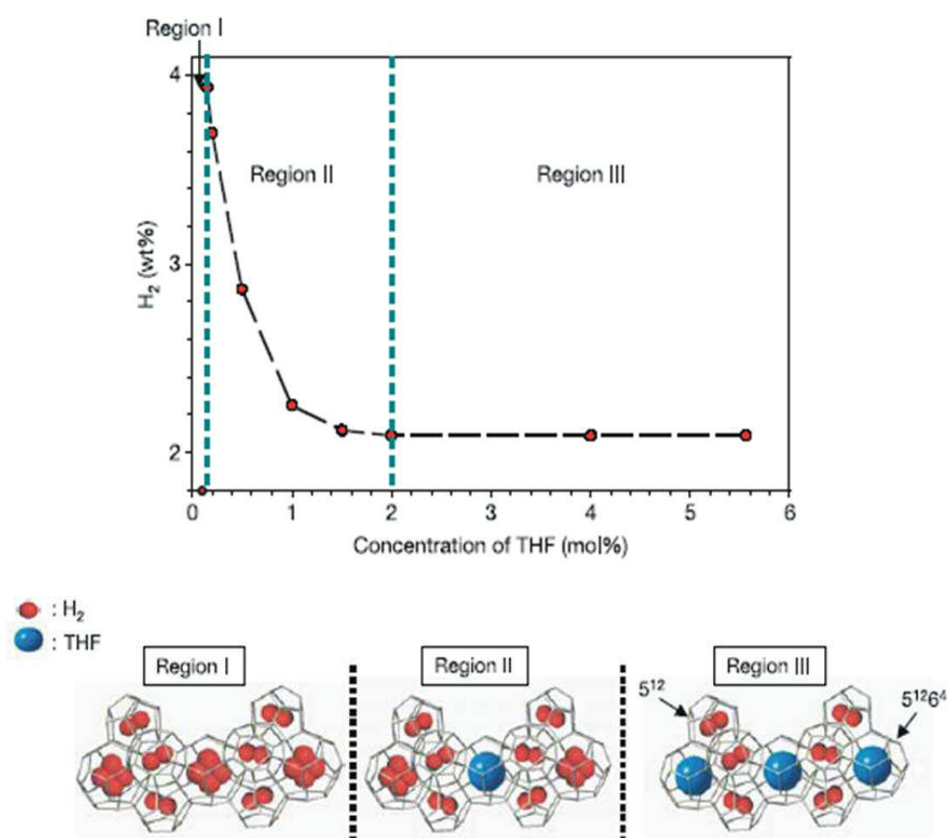


Figure 32. H₂ gas content (wt %) as a function of THF concentration and a schematic diagram of H₂ distribution in the cages of THF + H₂ hydrate (Lee et al., 2005).

The existence or non-existence of H₂ double-occupancy of the 5¹² cage will be a key factor in determining the feasibility of binary cubic clathrates for hydrogen storage, because double occupancy changes the possible hydrogen concentration in the hydrate from 1 to 2% for the stoichiometric hydrate (Hester et al., 2006).

Recently Hester et al. (2006) performed a series of neutron powder experiments on the THF-H₂ clathrate hydrate to directly determine the occupancy of hydrogen in the small cavities of the binary clathrate. They determined that the THF molecule occupies the large cage (Figure 33a) and most importantly, the small 5¹² cage is occupied by only a single molecule of hydrogen (Figure 33b). This experimental data was published after the experiments carried out at LANSCE and have been used to help model the inelastic neutron scattering results we have observed.

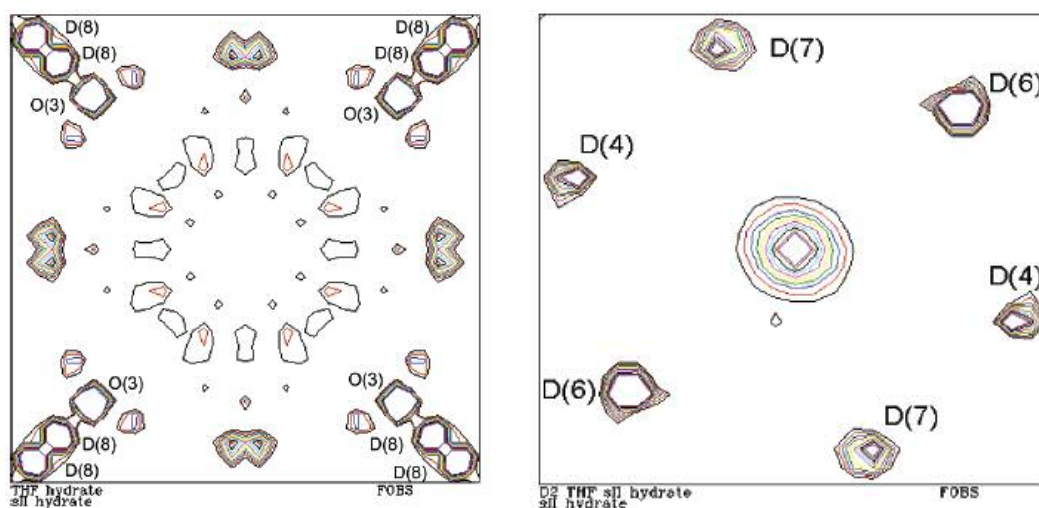


Figure 33a. Observed Fourier map of the THF-*d*₈ system centered in the 5¹²6⁴ cavity at (3/8, 3/8, 3/8) with the ring of density attributed to the THF-*d*₈ molecule and the density contours on the edges due to the water molecules. The map size is 10 Å, and the contours are drawn at 0.1 – 10 fm. 6b. Observed Fourier map of the D₂ + THF-*d*₈ system centered in the 5¹² cavity at (0,0,0) with the single hydrogen molecule centered in the picture and the other density contours attributed to portions of the water cage. The map size is 8 Å, and contours are drawn at 0.2 – 2.0 fm. Both are figures from Hester et al., 2006.

3.3 Motivation of experiment

In the spring of 2005, the Lee et al. (2005) paper had just been published, and there was much interest in the ability to “tune” clathrate hydrates by reducing the large stabilizer molecule and increase the hydrogen storage abilities. In the literature, there was quite a discrepancy in the reported hydrogen occupancy of the small cage (Figure 34), and the mechanism of hydrogen substituting for the THF molecule in the large cage to increase the hydrogen storage capacity had only been studied with Raman and NMR. If there was a possibility of “tuning” other large molecules to increase the amount of hydrogen stored in the clathrate structure, then perhaps a solution for the onboard storage capacity of hydrogen could be suggested. I submitted a proposal with Frans Trouw, the instrument scientist on Pharos, for an ongoing program of neutron inelastic scattering experiments on ice clathrate materials and a follow-up experiment on the Disk Chopper Spectrometer (DCS) instrument at the National Institute of Standards and Technology Center for Neutron Research (NCNR).

3.4 Experimental details- Introduction

Neutron INS measurements on hydrogen adsorbed in d-THF+D₂/D₂O ice clathrate at different energies, temperatures, and compositions (one sample from each of the three regions) were carried out on the Pharos spectrometer at the Los Alamos Neutron Scattering Center (LANSCE) and the Disk Chopper Spectrometer (DCS) at the NIST Center for Neutron Research, National Institute of Standards and Technology, Gaithersburg, Maryland.

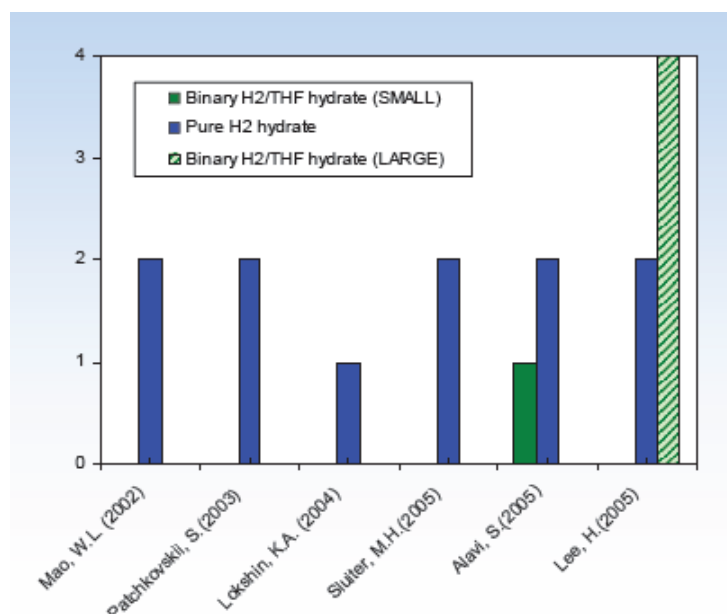


Figure 34. Summary of hydrogen cage occupancies in gas hydrates (http://www.hydrogen.energy.gov/pdfs/review06/bes_st11_sloan.pdf)

3.4.1 Pharos spectrometer

The High-Resolution Chopper Spectrometer, Pharos at LANSCE is a direct-geometry spectrometer and is designed for studies of fundamental excitations in condensed-matter systems (Figure 35). The instrument sits on a chilled-water moderator and uses a high-speed Fermi chopper to obtain monochromatic incident energies in the range from 10 meV to 2 eV. There are 10 m² of meter-long position-sensitive detectors located 4 m from the sample.

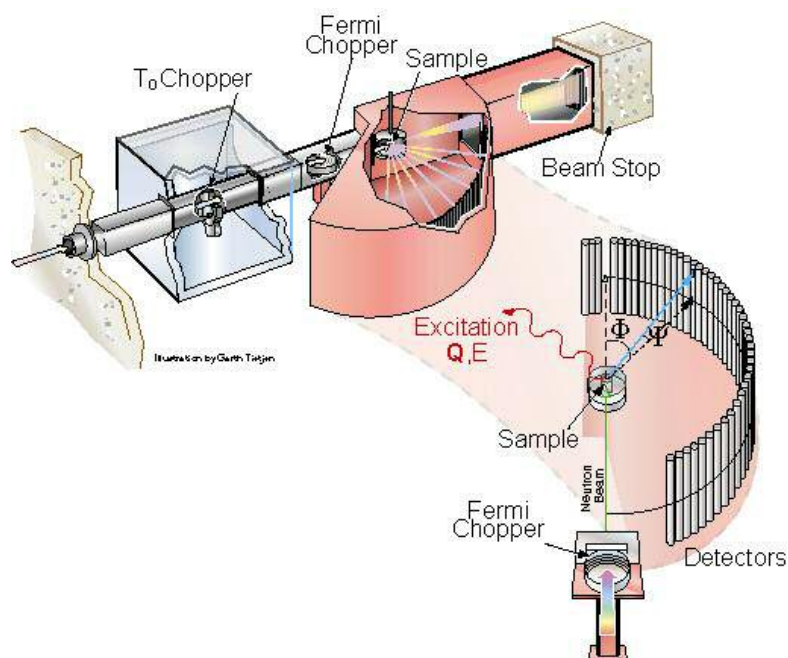


Figure 35. Schematic of the High-Resolution Chopper Spectrometer, Pharos at LANSCE (supplied by LANSCE-Lujan Center).

For the gas hydrate experiments a sample cell needed to be designed for Pharos. We took the existing properties from the cell for diffraction experiments (Al-cell design, gas inlet on the top) and redesigned it for the exceptionally large beam on Pharos (5 cm wide x 7.5 cm high) to maximize sample in the beam. The 7075 cold roll T6 aluminum pressure cell (rated to 10,000 psi with a safety rating of 5x) has seven sample-wells that are separated by 1/10" walls (designed this way for safety reasons). Once the gas is introduced through a 1/16" high-pressure line, the gas is distributed evenly through the cell by a groove in the lid of the cell (Figure 36a and b). The cell and the lid are sealed with an indium wire and 16 screws evenly distributed around the top of the cell.

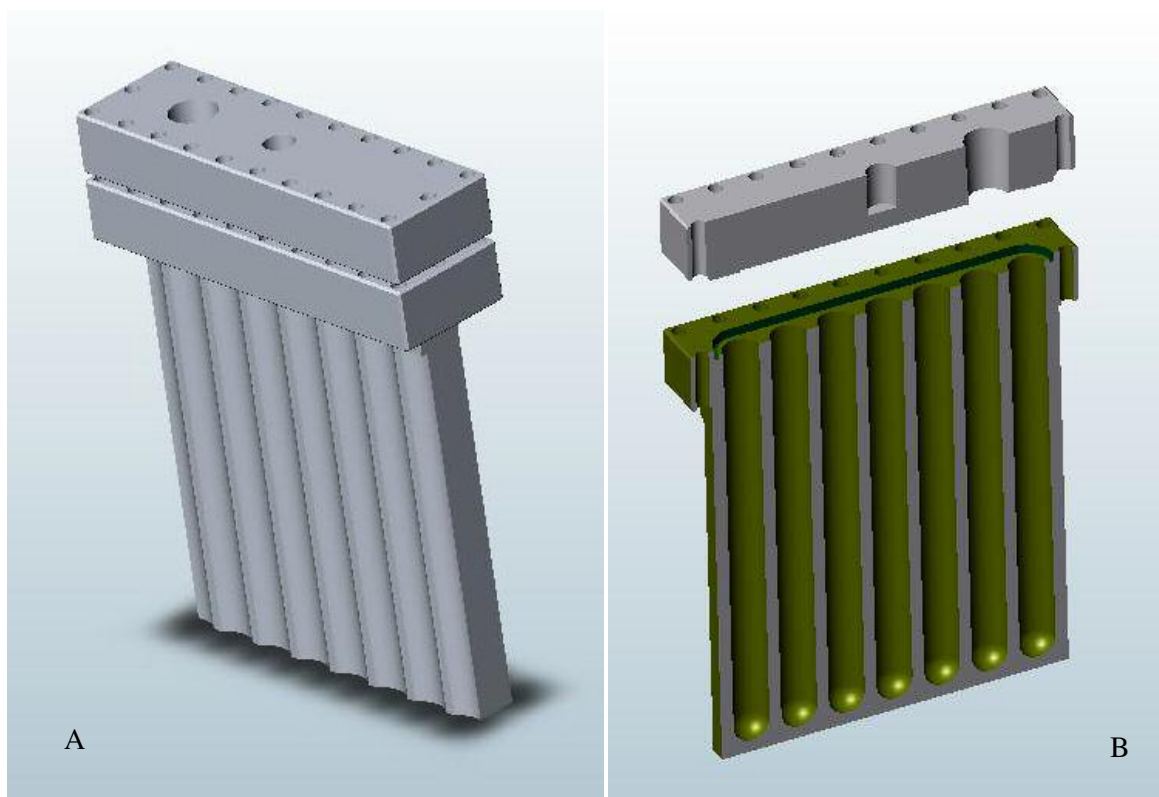


Figure 36a. Schematic of the gas hydrate cell designed at LANSCE for Pharos experiments; 9b. Cutaway view of the internal structure of the cell- seven sample wells, split by 1/10" Al for safety concerns (supplied by M. Taylor, designer from LANSCE).

3.4.2 Pharos experimental details

A 17:1 molar ratio of h-THF (Aldrich 99.8% minimum purity) or d-THF (99.95% D, Aldrich) and D₂O (99.9% D, Aldrich) was prepared under vacuum. The THF solution was then placed in a freezer at approximately 250 K for about 3 days. The resulting hydrate was crushed in a mortar surrounded by dry ice, and approximately 18 g were loaded into a specially designed cell for Pharos measurements (3.35" x 3.25" x 1" to take advantage of the large beam on Pharos). The cell was then attached to a pre-cooled displacer head and inserted

into the Pharos sample chamber and evacuated for the measurements. Thirty-one separate measurements were made of the protonated-THF, deuterated-THF alone and with H₂ gas added at different temperatures and energies, as well as varying THF concentrations in the starting solution (Table 4). When the H₂ gas was added at 270 K, we maintained a fairly steady pressure of 2,000 psi to ensure the clathrate was well within its stability range (Figure 37). Before measurements were conducted, the sample was valved off and cooled to 25 K and subsequently evacuated to remove the free hydrogen gas, and then cooled to base temperature, approximately 8 K. By using isotopic substitution, we were able to isolate certain features of the hydrate that we were interested in- for example, by using D₂O for the gas hydrate cage, d-THF for large molecule, and H₂ gas we are able to “see” the inelastic features of the H₂ guest molecule (all examples, Figure 38).

<u>15 meV, 120 Hz (DAQ window 12.5 to 19.5 ms)</u>	<u>25 meV, 180 Hz (DAQ window 10-15 ms)</u>
Empty can, 8K	Empty can, 8K
h-THF clathrate, 8K	h-THF clathrate, 8K
d-THF/D2O, 8K	d-THF/D2O, 8K
d-THF/D2O, H2 excess removed, 8K	d-THF/D2O, H2 excess removed, 8K
d-THF/D2O, H2 excess removed, 8K	
d-THF/D2O, H2 excess removed, 8K	
d-THF/D2O, H2 excess removed, 8K	
d-THF/D2O, H2 filling, 270K	
d-THF/D2O, H2 excess removed, 90K	
h-THF/D2O 0.7Mol% THF-2, 8K	
<u>40 meV, 240 Hz (DAQ window 8-14 ms)</u>	<u>70 meV, 240 Hz (DAQ window 6-9 ms)</u>
Empty can, base temp	d-THF/D2O, 50K
h-THF clathrate, <10K	d-THF/D2O, absorbing H2, 270K
d-THF/D2O, 100K	d-THF/D2O, H2 excess removed, 8K
d-THF/D2O 0.2Mol%	
h-THF/D2O 0.2Mol%	<u>120 meV, 360 Hz (DAQ window 4-8 ms)</u>
h-THF/D2O 0.7 Mol%	Empty can, base temp
h-THF/D2O high THF sample	h-THF clathrate, 8K
h-THF/D2O 0.7Mol%THF-2, 8K	d-THF/D2O, 8K
h-THF/D2O 0.7Mol% THF-2, 8K	d-THF/D2O, 100K
h-THF/D2O 0.7Mol% THF-2, with H2, 8K	d-THF/D2O, 50K
h-THF/D2O 0.7Mol% THF-2, 8K	

Table 4. Summary of all runs performed over 44 days of beam time on Pharos, organized by the selected incident energy of the experiment.

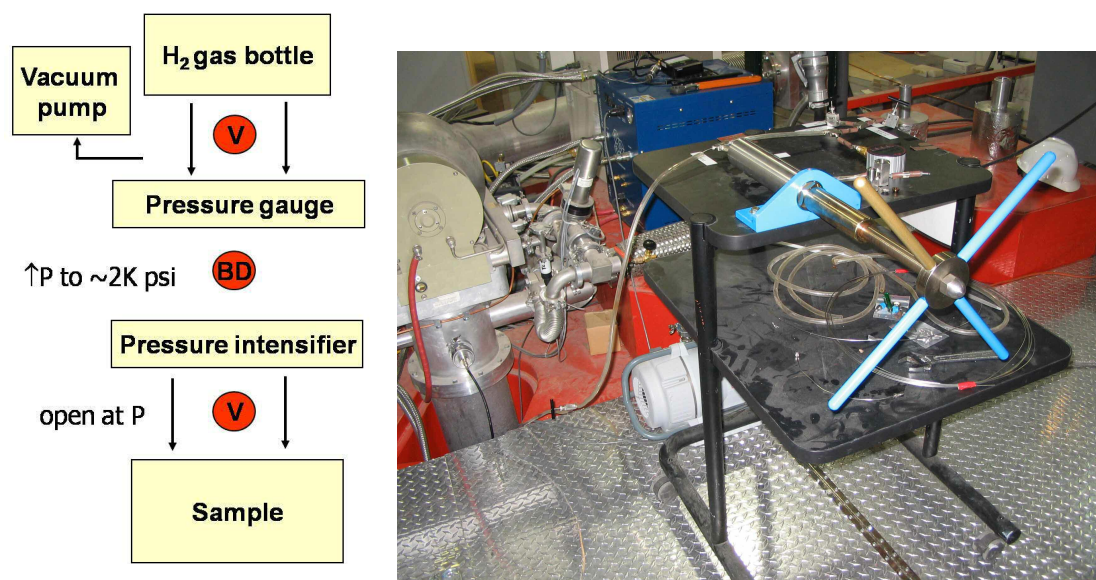


Figure 37. Schematic of gas handling system (V = valve, and BD = burst disk) and picture of actual setup on top of the Pharos instrument.

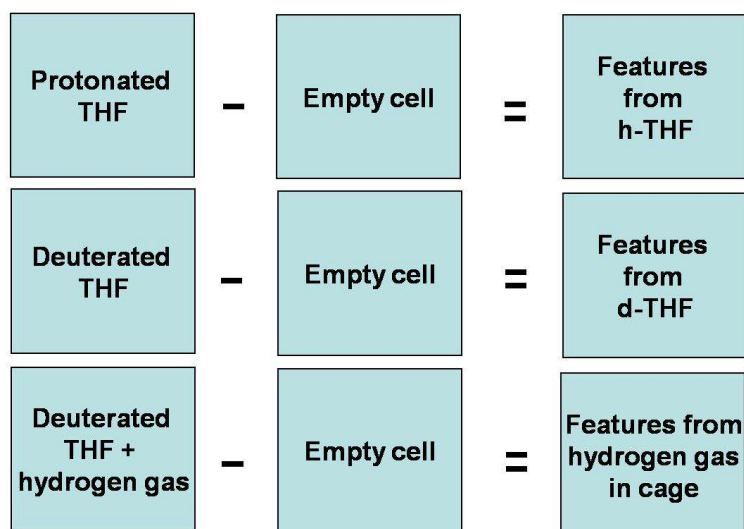


Figure 38. Schematic of isotope substitution of experiments on THF + H₂ on Pharos.

3.4.3 NIST Center for Neutron Research and DCS

The d-THF + H₂ experiment was carried out at the National Institute for Standards and Technology (NIST) Center for Neutron Research (NCNR) in Gaithersburg, Maryland. The NCNR is a reactor source that has 28 experiment stations: six provide high-neutron flux positions for irradiation, and 22 are beam facilities, most of which are used for neutron scattering research.

The Disk Chopper Spectrometer (DCS) is also a direct geometry time-of-flight spectrometer but sits on a cold neutron moderator. High-energy neutrons and gamma-rays are removed using an optical filter supplemented by a cooled graphite filter. This instrument was used because of its ability to obtain better elastic energy resolution compared to Pharos on the DCS instrument at NCNR.

3.4.4 Disk Chopper Spectrometer (DCS) experimental details

The sample was loaded into a cylindrical aluminum sample can with a wall thickness of 12.7 mm and a sample bore of 10 mm and loaded into a standard AS Scientific top-loading ILL cryostat (Figure 39). An incident wavelength of 5.5 Å was used at 5 K, 50 K, 100 K, 150 K and 200 K. The results were very similar to the results from the Pharos experiments and will be further discussed in Appendix C.

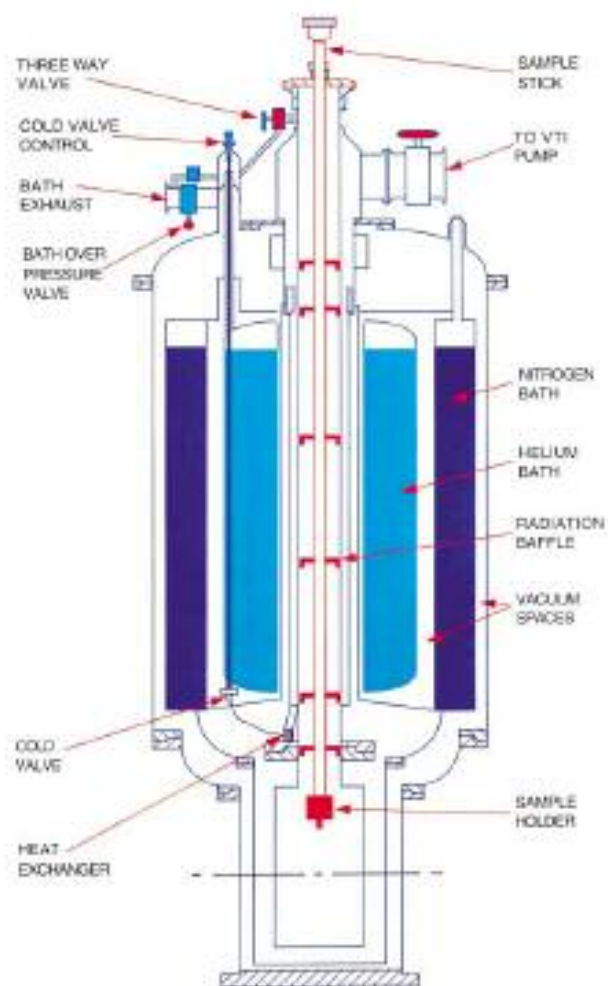


Figure 39. ILL designed liquid helium bath orange cryostat.

Chapter 4

INELASTIC NEUTRON STUDIES OF ETHYLENE OXIDE CLATHRATE

4.1 Motivation

Most gas hydrates grow only slowly and remain stable only under restrictive temperature and pressure conditions, which is the case for the pure methane and hydrogen clathrates. Much effort is currently being devoted to expanding the domain of stability of these clathrates by the addition of other guest molecules that are more readily miscible with water. The question then arises of whether hydrogen (or other gases) can be added to such structures. The preceding chapter demonstrated that this is the case for a structure II clathrate with THF; we now show for the first time evidence that a structure I clathrate with ethylene oxide can act as a host for hydrogen. Ethylene oxide is arguably the most studied gas hydrate due to the miscibility of the gas with water. It is a relatively large molecule for a structure I former, and the resulting clathrate has one of the highest melting temperatures (at atmospheric pressure) of all known clathrate hydrates. Inelastic Neutron Scattering (INS) on the Filter Difference Spectrometer (FDS) at LANSCE was used to study the dynamics of ethylene oxide and hydrogen in ethylene oxide clathrates.

4.2 Structure

Ethylene oxide (oxirane, MW 44.05) is a cyclic ether with a boiling point of 262.5 K (10.7°C) and a melting point of 162.2 K (-111°C). It is highly toxic, very flammable, and a known carcinogen. Ethylene oxide (C₂H₄O, Figure 40) is completely miscible with water.

Below room temperature it forms a cubic structure I clathrate with the approximate composition $C_2H_4O \cdot 6.86H_2O$. At this composition, the clathrate melts congruently at 284.2 K at atmospheric pressure (White et al., 2003). In fact, ethylene oxide is one of a handful of small molecules that can stabilize a hydrate above the freezing point of water. This property eliminates ice formation and mass transfer considerations in experimental work. Large single crystals of the clathrate can be grown without difficulty. McMullan and Jeffrey (1965) determined through X-ray single-crystal diffraction experiments that the cage occupancy factor is 1 for the tetrakaidecahedron cage and approximately 0.2 for the dodecahedra cages. The space group is $Pm\bar{3}m$. The edge of the conventional (cubic) unit cell is $a = 12.03 \text{ \AA}$. Figure 41 shows the structure determined by McMullan and Jeffrey (1965). The cubic unit cell contains 46 water molecules.

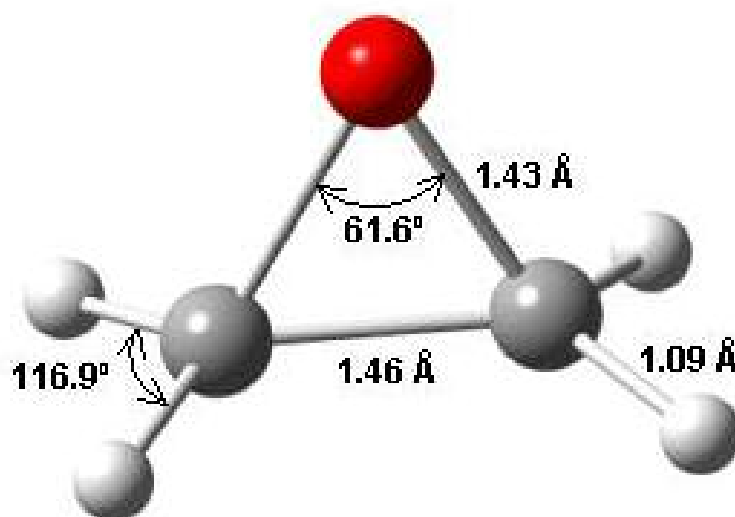


Figure 40. The ethylene oxide molecule. The molecule is significantly larger than methane and is highly polar (dipole moment 1.88 Debye -virtually identical to that of water) owing to the large electron density on the oxygen atom (figure from L. L. Daemen).

In this material, the water molecules form hydrogen-bonded cages, as in other clathrates, but the protons are configurationally disordered and can occupy two possible positions between adjacent oxygen atoms. This disorder is very likely dynamic, with protons moving back and forth between these possible positions. If temperature is sufficiently low, however, the protons get frozen into a disordered state, Figure 41.

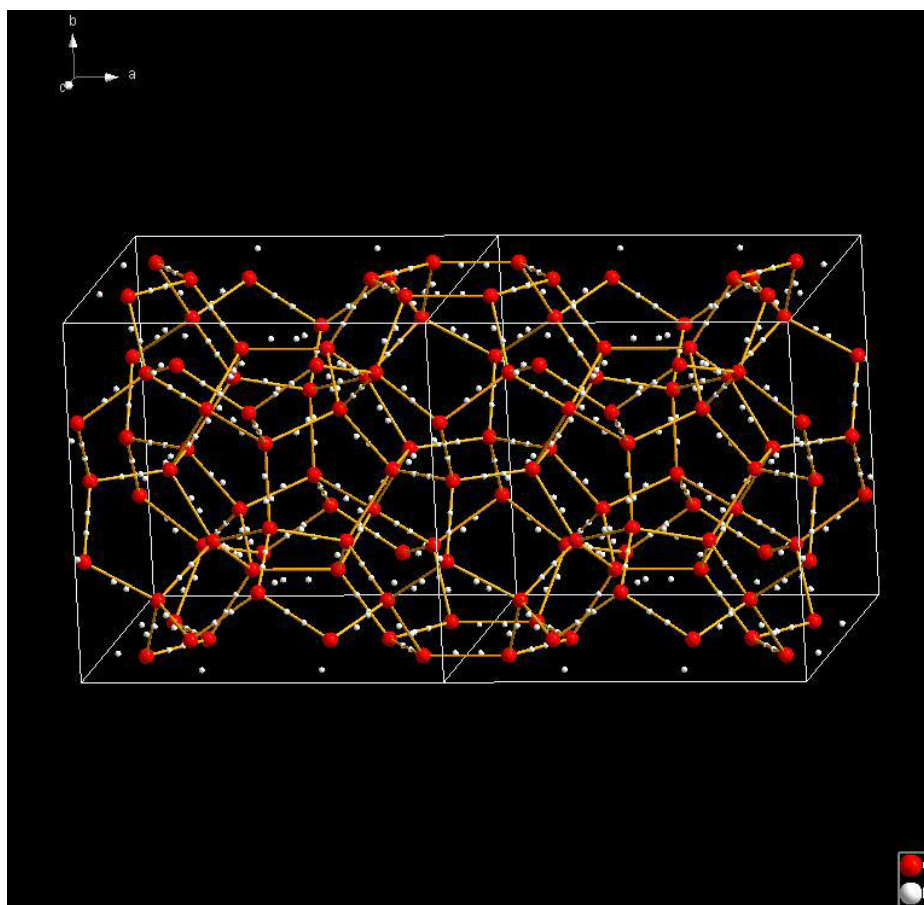


Figure 41. The crystal structure of $C_2H_4O.6.86H_2O$ as determined by McMullan and Jeffrey (1965) by single crystal X-ray diffraction at 243 K. Ethylene oxide is not shown for clarity; each O-O bond shows two sites for hydrogen. Each site has an average occupancy of 0.5 and two unit cells are shown. Two large cages (tetrakaidecahedra) are clearly visible at the center of the figure. Dodecahedra appear at the center of each cubic unit cell.

Figure 42 shows a large tetrakaidecahedron cage with two possible orientations for ethylene oxide. According to McMullan and Jeffrey (1965), the orientation of ethylene oxide is disordered, with the oxygen atom on ethylene oxide pointing at one of the six-membered oxygen rings in the cage.

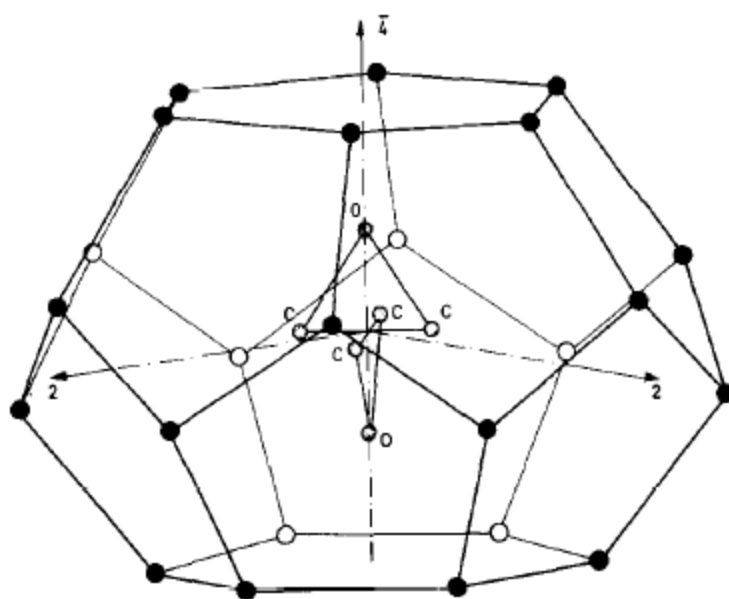


Figure 42. The $5^{12}6^2$ structure I tetrakaidecahedron cage with only the oxygen atoms of the cage shown, with two preferred orientations of the ethylene oxide molecule shown (McMullan and Jeffrey, 1965).

4.3 Dynamics: previous work

The first far-infrared spectra of ethylene oxide clathrates were collected in the seventies by Bertie et al. (1975) at temperatures ranging from 4.3 to 100 K. Those were the first far-infrared spectra of a structure I clathrate at low temperature. The low-frequency part of the spectra is dominated by two contributions:

- translational and rotational motions of the guest (ethylene oxide) and,
- translational motions of the water molecules in the cages.

The latter type of motion produces relatively broad features in the vibrational spectrum. In the inelastic neutron scattering work, the contribution from the cages was decreased deliberately (but not completely eliminated) by deuteration of the water. Table 5 summarizes the features observed by Bertie et al. (1975) in the vibrational spectrum of a deuterated ethylene oxide clathrate sample.

Frequency (cm ⁻¹)	Intensity	Assignment
35.0	strong, sharp	ethylene oxide libration
64.1	strong, sharp	ethylene oxide libration
84.3	strong, broad	water translation
118.9	strong, sharp	water translation
129.0	shoulder	water translation

Table 5. Absorption peaks observed in the vibrational spectrum of C₂H₄O · 6.86D₂O by Bertie et al. (1975) at 4.3 K.

Bertie et al. (1975) report a slight shift with temperature of the peaks listed in Table 5 up to 100 K. All peaks do remain observable up to 100 K. It should be noted that for a vibrational mode to be infrared-active, its associated motion must change (intensity or direction) a dipole moment. Water and ethylene oxide are polar molecules and many, but not all, of their vibrational or librational modes will be infrared-active. It has already been noted that the

dipole moment of water and that of ethylene oxide are virtually identical. Whereas the motion of the ethylene oxide molecule has potentially greater amplitude than that of the hydrogen-bonded water molecules in the cages, there are nearly seven times as many water molecules as there are ethylene oxide molecules. One can thus expect a significant contribution from water to the infrared absorption spectrum. The rotational motion of ethylene oxide can, in principle, be decomposed into librations about the three principal axes of the molecule. However, it is clear that rotation about an axis defined by the oxygen atom and the midpoint between the carbon atoms does not change the dipole moment of the molecule because the dipole moment is parallel to that axis. There remain two librational modes corresponding to rotations about axes perpendicular to the axis just defined. These modes should be infrared-active and are assigned to the two low-frequency peaks at 35.0 and 64.1 cm^{-1} (4.4 and 8.0 meV, respectively) by Bertie et al. (1975). These peaks are not affected by a H_2O to D_2O isotopic substitution and must therefore be associated with ethylene oxide. A word of caution is order; however, librational modes are notoriously difficult to observe by infrared or Raman spectroscopy. The statement made by Bertie et al. (1975) that the modes at 35 and 64.1 cm^{-1} should be attributed to ethylene oxide librational modes is suspect for two reasons. First, these modes appear very strongly in their spectrum, which is unusual in itself. Second, the lack of significant shift upon going from H_2O (molecular weight 18) to D_2O (molecular weight 20) is less than convincing because if the two modes are water translational modes rather than ethylene oxide librations, the entire molecule moves and the frequency of the modes is reduced by a factor of $(20/18)^{1/2}=1.05$.

The 35.0 cm^{-1} mode would shift to 33.3 cm^{-1} (absolute shift of 1.7 cm^{-1}) and the 64.1 cm^{-1} mode would shift to 61.0 cm^{-1} (absolute shift of 3.1 cm^{-1}). Given an instrument resolution of about 2.5 cm^{-1} and rather broad peaks, it is doubtful that such small shifts could be observed with great reliability. Finally, as will be discussed below, the inelastic neutron scattering spectrum collected on FDS shows intensity at 35 and 65 cm^{-1} in addition to sharper modes at other frequencies. The latter are more likely to be the ethylene oxide librational modes. The ethylene oxide "librational" modes observed by Bertie et al. (1975) are very likely to be attributed to translational modes of water in the cages. The last three peaks listed in Table 5 shift to lower frequency when going from H_2O to D_2O and are undoubtedly associated with the water cages. In this case, the isotopic shifts are at least twice the resolution of the instrument used by Bertie et al. (1975) and are more conclusively apparent in the spectra.

An inelastic neutron scattering study was performed by Wegener et al. (1978) on ethylene oxide clathrate at three temperatures, 30 K, 90 K and 214 K. The study was undertaken for two reasons: in contrast to optical spectroscopies, neutron scattering is immune from selection rules and deuteration of the cages could, in principle, reduce the contribution of the cages to the vibrational spectrum. There is a third advantage to neutron scattering, which was not obvious at the time Wegener et al. (1978) collected data, namely the ability (at the time of writing) to calculate quantitatively the neutron vibrational spectrum from *ab initio* or molecular dynamics computer simulations. This is a direct result of the simplicity of the neutron-nucleus interaction at thermal neutron energies, as opposed to the extremely complex electron-photon interactions, which makes a quantitative prediction of

vibrational mode intensities difficult at best. The comparison between the calculated spectrum and the measured spectrum is a powerful tool to assess the validity of a (structural) model of the system under study.

It follows that neutron vibrational spectroscopy should enable one to observe the third librational mode of ethylene oxide and confirm the mode assignments of Bertie et al. (1975). Features in the neutron vibrational spectrum of Wegener et al. (1978) are observable at 30 K (labeled A, B, C and D, Figure 43), but at higher temperatures the features disappear. The A, B, and C peaks (29 ± 2 , 39 ± 4 , and 57 ± 4 cm^{-1}) are assigned to the librations of the ethylene oxide molecules about the three principal axes of inertia (Wegener et al., 1978). Peak A corresponds to the librational mode that is inactive in the infrared spectrum. Peaks B and C are, in principle, those observed by Bertie et al. (1975). The agreement with the values reported by Bertie et al. (1978) is reasonable but far from spectacular. The features in the spectrum are broad, and the uncertainty on the position of the vibrational modes is fairly large. Shoulders appear in the vibrational spectrum that can be attributed to translational (external) modes of water. The peak labeled D in Figure 43 is very likely the mode observed at 84.3 cm^{-1} by Bertie et al. (1978).

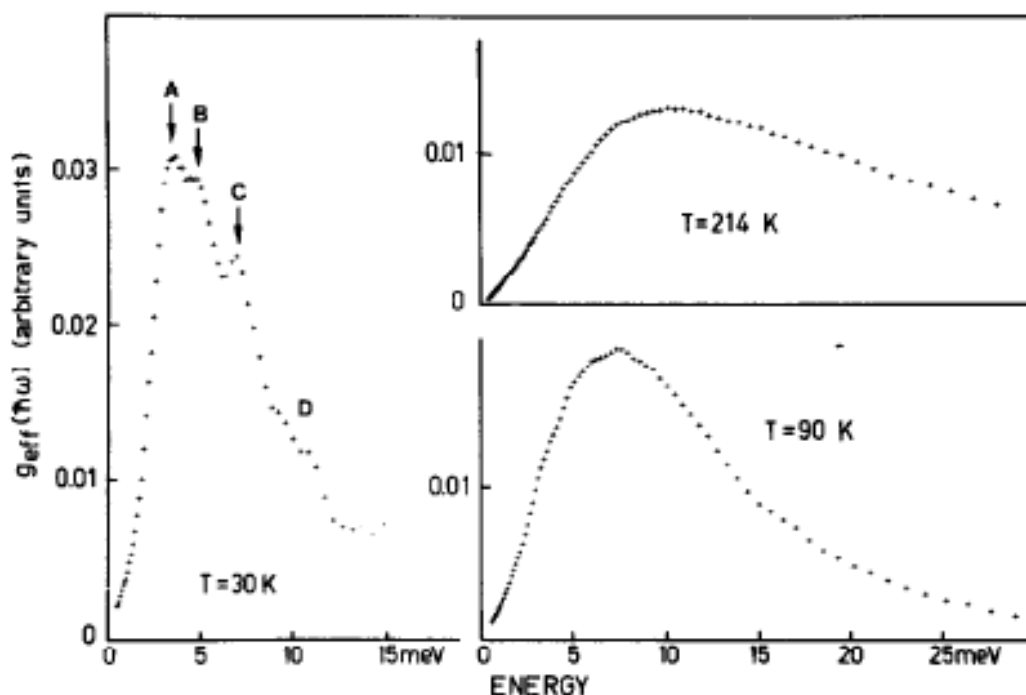


Figure 43. Frequency distributions at 30 K, 90 K and 214 K (Wegener et al., 1978).

4.4 Dynamics: neutron scattering

The poor resolution of the vibrational spectrum obtained by Wegener et al. (1978) leaves open the question of a more precise experimental determination of the librational modes (and therefore, of the associated librational potentials). Given today's computational capabilities, it is also desirable to resolve experimentally some of the water vibrational modes for a direct comparison with *ab initio* or semi-empirical calculations. Finally, a good reference neutron vibrational spectrum was needed to start investigating the possibility of using ethylene oxide to stabilize clathrate hydrates. For all these reasons, it was decided to revisit the problem of the neutron vibrational spectrum of ethylene oxide clathrates. Data were collected at LANSCE on the Filter Difference Spectrometer (FDS).

4.4.1 The Filter Difference Spectrometer (FDS)

The Filter Difference Spectrometer (FDS) at LANSCE is an “inverted geometry instrument” which means a “white” neutron beam (containing a continuous range of neutron wavelengths) is incident upon the sample (Daemen et al., 2006). The instrument sits 13 m from a 283 K water moderator (Figure 44), and incoming neutrons excite molecular vibrations in the sample and then are scattered into symmetrically arranged beryllium or beryllium oxide filters to the detectors.

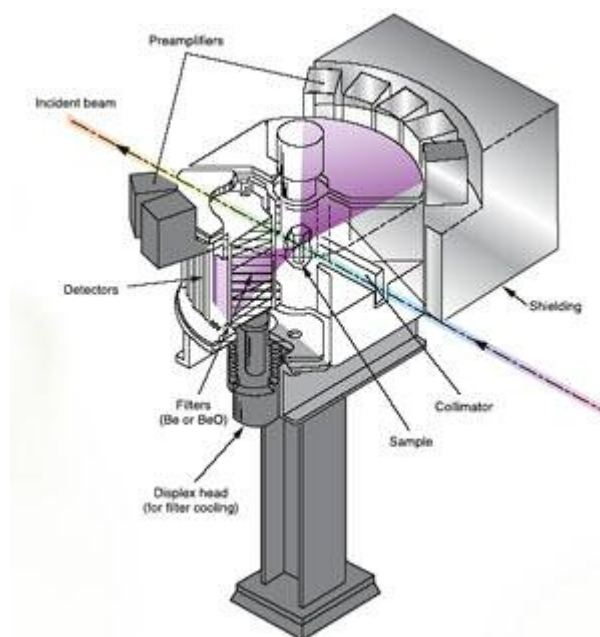


Figure 44. Schematic of the Filter Difference Spectrometer (FDS) at LANSCE (Supplied by LANSCE-Lujan Center).

The final neutron energy is kept fixed (in a direct geometry instrument at a pulsed source, the incident neutron energy is fixed and the final neutron energy is variable).

The *primary spectrometer* is essentially a long evacuated flight tube (rectangular cross section approximately 2.5 cm x 10 cm) surrounded by a large amount of shielding. A series of collimators right before the sample deliver the beam to the heart of the secondary spectrometer. The other important components of the primary spectrometer are the moderator (ambient temperature water, poisoned and decoupled) and a mercury shutter to block the beam during sample changes. The flight path is perpendicular to the moderator surface.

The *secondary spectrometer's* main component is an annular tank containing the Be and BeO filters. Each filter bank covers 90° on each side of the incident flight; each filter wedge covers 15° and is flanked by a detector bank comprising six ^3He tubes for neutron detection. A time-of-flight spectrum is collected for each individual tube, but the spectra can be combined by bank or summed of filter type (Be or BeO). Two expander heads hanging from the bottom of the filter tank are used to cool the filter to approximately 100 K in the evacuated filter tank. Cooling reduces phonon scattering of the transmitted neutrons and improves the data collection rate. The sample is located at the center of the annular tank, usually inside a cooling device.

The *principle of operation* of the spectrometer is relatively simple. The Be and BeO filters in the secondary spectrometer allow neutrons of a fixed energy to pass through the block of filter material. This determines the energy of the scattered neutron (e.g., 4.2 meV for Be). The incident neutron energy is determined by time-of-flight. The difference between the final and initial neutron energy is the energy of the elementary excitation in the

sample. In practice, the Be and BeO filters are not perfect band-pass filters and a finite range of final neutron energies passes through the filters. A simple numerical deconvolution allows one to take this into account during the data reduction stage.

Calibration spectra (uracil and hexamethylenetetramine) are collected at the beginning of a run cycle. The vibrational spectrum of these materials exhibits a large number of sharp lines at well-established frequencies throughout the entire dynamic range of the instrument. These spectra allow one to verify that the conversion from time-of-flight to energy transfer is accurate.

4.4.2 Synthesis of the deuterated ethylene oxide clathrate

FDS relies on the incoherent scattering of neutrons to obtain a vibrational spectrum. Since hydrogen (protium) has the highest incoherent neutron scattering cross section (80.27 barn) of all isotopes, the vibrational spectrum is –to first order– entirely dominated by contributions from hydrogen. Deuterium has a much lower incoherent scattering cross section (2.05 barn) and isotopic substitution can then be used to “highlight” the fragments of a molecular system that contribute to the spectrum. In the case of the ethylene oxide clathrate, the main interest resided with the dynamics of the ethylene oxide molecule rather than those of the cages themselves. It was therefore decided to synthesize a clathrate with protonated ethylene oxide and deuterated water: $C_2H_4O \cdot 6.86 D_2O$. Notice that the molar ratio of D to H is approximately 3.4 : 1. Even though the scattering from D is considerably less than that of H_2 , one can still expect a significant contribution from D_2O .

Given the miscibility of ethylene oxide and water and the potential difficulties associated with handling ethylene oxide, *in situ* preparation of a suitable sample was attempted. FDS is equipped with a small gas handling manifold that permits gas dosing and delivery to a sample holder to which a capillary tube is attached. The sample holder resides in a closed-cycle refrigerator and was held at constant temperature. Without mechanical agitation (which was not possible in the closed-cycle refrigerator), ethylene oxide dissolves only slowly in water, and it became clear rather rapidly that *in situ* preparation would produce unsatisfactory samples.

Laboratory synthesis was then attempted. The synthesis setup is illustrated in Figure 45. In a fume hood, we dosed and condensed the ethylene oxide gas onto a known volume of frozen D₂O. The mixture was allowed to melt. It was stirred thoroughly for a few minutes. We then placed it in an aluminum sample holder and transported it to the closed-cycle refrigerator on FDS. We held this mixture at 270 K for 70 minutes and then 283.2 K for two hours (slightly below the melting point of the clathrate) for sample annealing.

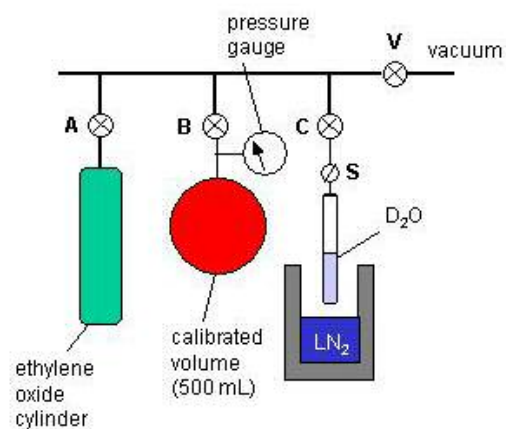


Figure 45. Setup for the synthesis of ethylene oxide clathrates. A carefully measured volume of D_2O is placed in a glass tube connected to valve C. The D_2O is frozen with liquid nitrogen and with valves B, C, S, and V open (A closed) the apparatus is evacuated. Subsequently V, S, and C are closed and with B open, A is opened to fill the calibrated volume connected to valve B. Once the desired pressure of ethylene oxide is reached in the calibrated volume, valve A and B are closed and the apparatus is again evacuated to remove residual ethylene oxide in the apparatus. Valves B, C, and S are then opened to condense the ethylene oxide in the calibrated volume into the glass tube containing D_2O . When the pressure in the calibrated volume falls to zero, valve C and S are closed and the sample tube is disconnected (between C and S) from the vacuum line. Its content is allowed to warm up to room temperature. Gentle mechanical agitation then allows for thorough mixing of D_2O and ethylene oxide. The solution is then transferred to an aluminum sample holder (for neutron scattering) and slowly cooled below its freezing point to form the clathrate.

4.4.3 Ethylene oxide clathrate: Results

Figure 46 shows the low frequency part of the neutron vibrational spectrum of an ethylene oxide clathrate sample, $C_2H_4O \cdot 6.86 D_2O$, measured at 10 K on FDS.

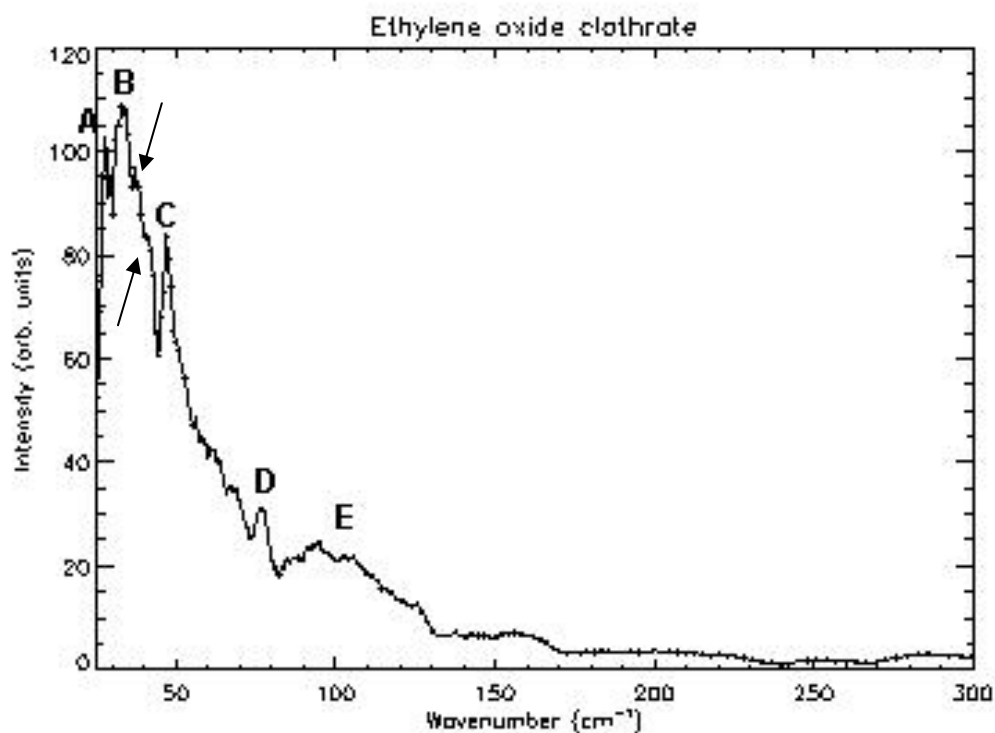


Figure 46. Neutron vibrational spectrum of ethylene oxide clathrate collected at 10 K on FDS. Peaks A, B, and C are the librational modes of ethylene oxide. The labeling corresponds to that used by Wegener et al. (1978) (see Figure 43). Peak D and the broad band E are discussed in the text. The arrows indicate two shoulders that were not present in the Wegener et al. result.

The resolution is significantly improved compared to the result by Wegener et al. Table 6 summarizes the librational frequencies observed on FDS at 10 K. The agreement with Wegener et al. (1978) is reasonable. The difference between our results and those of Wegener et al. (1978) increases with frequency. This suggests perhaps a problem with the conversion from time-of-flight to energy transfer or, more generally, an instrument calibration problem in the data of Wegener et al. (1978). Unfortunately, no details are provided by Wegener et al. (1978) as to where and how the data were collected and

processed. Since FDS passed two stringent calibration tests at the beginning of the run cycle, we stand by our values. It is almost certain that Bertie et al. (1975) observed attributed water translational modes to ethylene oxide librations (see discussion above). Their values are listed in Table 6 for completeness, but they are almost certainly incorrect.

Frequency (cm⁻¹) This work (INS, 10 K)	Frequency (cm⁻¹) Wegener et al. (1978) (INS, 30 K)	Frequency (cm⁻¹) Bertie et al. (1975) (IR absorption, 4.3K)
28.3	29 ± 2	not observed, inactive
34.4	39 ± 4	35.0
48.0	57 ± 4	64.1

Table 6. Librational frequencies of ethylene oxide in ethylene oxide clathrate. Comparison of infrared absorption and inelastic neutron scattering measurement.

FDS resolves some of the water translational modes. The mode at 76 cm⁻¹ (and assigned a frequency of 81 cm⁻¹ by Wegener et al., 1978) is particularly well resolved. The broad 80-170 cm⁻¹ band also exhibits some structure. A maximum entropy analysis of this band produces peaks at 97.5, 136.2, and 155.3 cm⁻¹. Similarly, two shoulders appear between peaks B and C that should be attributed to translational modes of water. These features were not resolved by Wegener et al. (1978) and were not observed by Bertie et al. (1975) in the infrared absorption spectrum. They should prove useful in comparisons with *ab initio* calculations. Notice that the A and C peaks are relatively sharp. Peak B appears to be broader, but this is almost certainly due to the presence of another peak at almost the same frequency. In all likelihood, this is the 35 cm⁻¹ peak observed by Bertie et al. (1975). The FDS spectrum shows a faint shoulder at 65 cm⁻¹, which almost certainly is the 64.1 cm⁻¹

mode observed by Bertie et al. (1978) and has nothing to do with the librational modes of ethylene oxide.

The ethylene oxide molecule comprises $N = 7$ atoms. It should therefore have $3N - 6 = 15$ internal vibrational modes. The vibrational spectrum of ethylene oxide has been measured on numerous occasions, in the gas, liquid, and solid phase by means of infrared absorption (Bertie and Jacobs, 1978), Raman scattering (Lebruman, 1969), and inelastic neutron scattering (Coulombeau and Jobic, 1988). Since each molecule of ethylene oxide is isolated in a cage in the clathrate, intermolecular interactions between ethylene oxide molecules are negligible and the vibrational spectrum of enclathrated ethylene oxide should resemble those of ethylene oxide in the gas phase. Deviations from the gas phase spectrum can be attributed to guest-host interactions. Figure 47 shows the high frequency portion of the ethylene oxide clathrate vibrational spectrum as measured at 10 K on FDS. To the best of our knowledge, this portion of the spectrum of ethylene oxide clathrate has never been investigated. The broad band extending from 400 to 800 cm^{-1} corresponds to the three librational modes (wagging, twisting, and rocking) of water in the cages (Eisenberg and Kauzmann, 1969). Structure is evident in the band. These modes are not observable by means of optical spectroscopy (IR or Raman), but usually appear quite clearly in the neutron vibrational spectrum. The fact that three peaks can just about be distinguished in the band is characteristic of hydrogen-bonded water (free water tends to produce a broad, featureless band). The broad band above 2000 cm^{-1} corresponds to a series of OD stretching modes (Eisenberg and Kauzmann, 1969).

The internal modes of ethylene oxide appear above 800 cm^{-1} . The modes are relatively poorly resolved, probably due to the presence of ethylene oxide in two different cages and the (different) interactions of ethylene oxide with these cages. Our relative intensities are comparable to those in the vibrational spectrum of solid ethylene oxide observed by Coulombeau and Jobic (1988), and this facilitated mode assignment. Table 7 summarizes our findings.

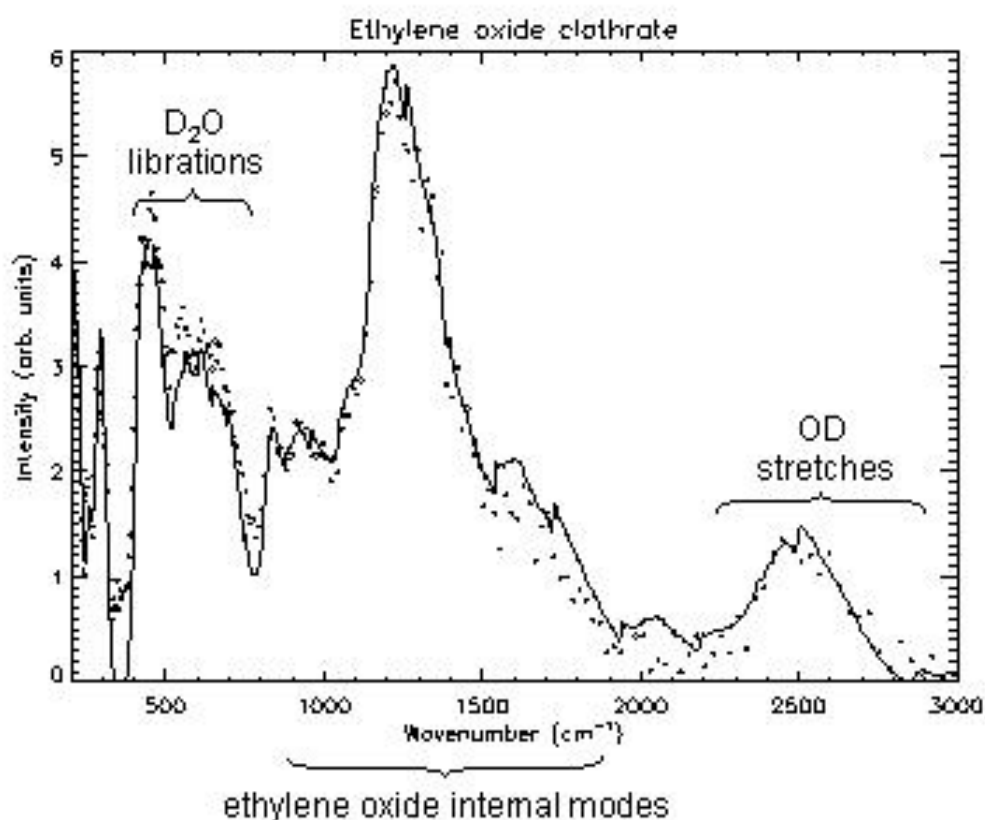


Figure 47. The high frequency portion of ethylene oxide clathrate. The solid line is a maximum entropy reconstruction of the vibrational spectrum.

It is immediately apparent from Table 7 that all the internal modes of ethylene oxide are recognizable in the FDS spectrum. Most of the modes are shifted to higher frequencies compared to the gas phase measurements - a clear indication of strong interactions between the cages and the ethylene oxide molecules. This is not altogether surprising given the large dipole moment (1.88 Debye) of the ethylene oxide molecule and the presence of a large electron density on the oxygen atom (lone electron pairs). So-called solvent shifts effects have long been known in the physical chemistry of solutions. The frequency of vibrational modes is shifted (compared to the gas phase frequency, i.e., in the absence of intermolecular interactions) when a molecule is placed in a solvent. This is the result of solvent-solute interactions. The frequency shifts can be represented as the sum of shifts due to attractive and repulsive interactions:

$$\Delta\nu = \Delta\nu_A + \Delta\nu_R,$$

where $\Delta\nu_A$ is the solvent (frequency) shift due to attractive interaction and is generally negative and $\Delta\nu_R$ is due to repulsive interactions and is generally positive (Benamotz and Herschbach, 1993). Repulsive forces can be thought of in terms of steric effects. Attractive forces result generally from dipole-dipole interactions. The shifts can be related to microscopic (solvent and solute) parameters by means of rather complex theories. Even though ethylene oxide clathrates are solids, it is tempting to draw an analogy with solution chemistry and think of ethylene oxide in the clathrate as being "in solution" in water. Since our observed "solvent shifts" from gaseous ethylene oxide to "solvated" ethylene oxide are positive (blue shifts), repulsive interactions between ethylene oxide and water cages seem to

dominate the attractive solvent-solute interactions. Of course, it is ultimately the equilibrium between the strong hydrogen bonding between water molecules and the attractive guest-host interactions on the one hand and the (steric) guest-host repulsion on the other hand that explains the stability of the clathrate. To the best of our knowledge, clathrate stability has not been described in terms of solvent shifts (and the underlying interactions). This approach could represent a simple description of guest-host interactions in clathrates that is easy to connect with spectroscopic measurements. It could also suggest ways of improving the field of stability of clathrates.

The C-H stretching modes appear above 3000 cm^{-1} in ethylene oxide and are difficult to observe with inelastic neutron scattering due to the low intensity available on a water moderator at these incident energies. They will not be discussed here.

We observe that once again the spectrum shown in Figure 47 should prove useful for comparison with more extensive *ab initio* calculations of the vibrational spectrum. The experimental spectrum must be reproduced quantitatively for the modeling of the guest-host interactions to have any validity.

4.4.4 Adding hydrogen

Since 80% of the small cages in ethylene oxide clathrate are not occupied, it is interesting to ask if they could be filled with a small molecule such as hydrogen. This would not produce a material with large hydrogen storage capacity, but it would result in a clathrate material with thermodynamic stability close to ambient conditions. Notice that in principle the small cage is large enough to accommodate more than one hydrogen molecule.

Frequency (cm⁻¹) This work	Frequency (cm⁻¹) IR absorption, (Spiekermann et al., 1982)	Assignment
single band at 850	821, 840, 857	ring deformation
broad band at 915	877	ring deformation
shoulder at 1060	1020, 1050	CH ₂ rock, CH ₂ twist
broad band at 1205	1142, 1148, 1152	CH ₂ wag
shoulder at 1315	1270	ring breathing
broad peak at 1585	1472, 1498	CH ₂ scissor

Table 7. Internal modes of enclathrated ethylene oxide measured on FDS as well as in the gas phase.

Preliminary inelastic neutron scattering data were collected on a sample prepared by holding a small amount of ethylene oxide clathrate just below the melting point and connecting the sample holder to a tank holding several moles of H₂ at 800 psi (approximately 55 atm). The sample was held at that temperature for an hour, and was then slowly cooled (over a period of 4 hours, approximately 1 K/min) to 40 K. At 180 K, the sample holder was vented to relieve any residual pressure of hydrogen and prevent the condensation of liquid or solid hydrogen at lower temperature.

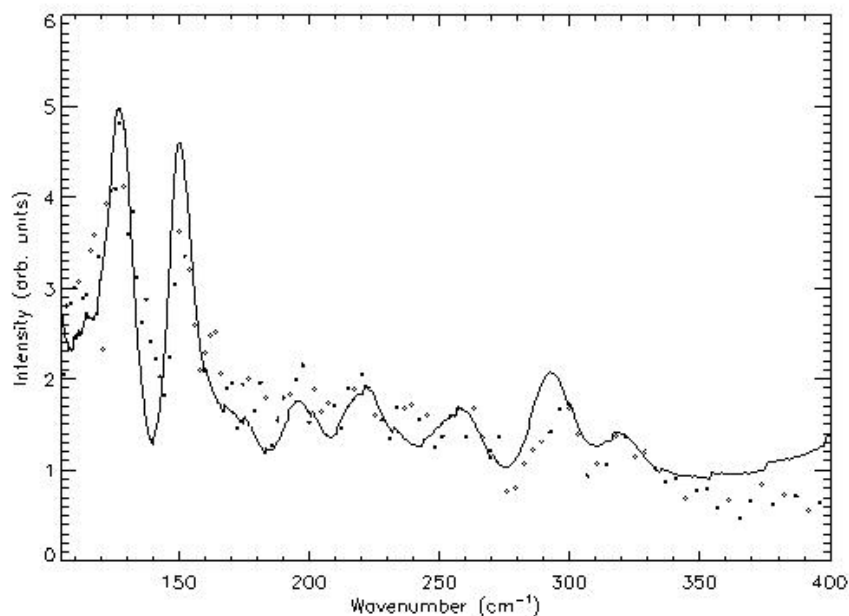


Figure 48. Neutron vibrational spectrum of hydrogen loaded in ethylene oxide clathrate, $T=40$ K. The spectrum from the pure ethylene oxide clathrate was subtracted to highlight the contribution from hydrogen. Two large peaks are clearly visible at 126 and 150 cm^{-1} . The solid line is the Maximum Entropy reconstruction of the spectrum.

Figure 48 shows the result obtained after subtracting the spectrum of pure ethylene oxide clathrate from the neutron vibrational spectrum of the sample loaded with hydrogen. The first rotational level of (free) hydrogen is at 14.7 meV ($= 118.6$ cm^{-1}). The most prominent peak in Figure 48 appears at 126 cm^{-1} -probably a good indication that hydrogen did indeed diffuse in the small cages of the ethylene oxide clathrate. There is a second peak at 150 cm^{-1} . These peaks are tentatively associated with the rotational energy level of hydrogen, shifted by intermolecular interactions either with the cage or with ethylene oxide. Smaller peaks appear at larger frequencies. Detailed molecular dynamics simulations would be necessary for a more detailed interpretation of the spectrum.

4.5 Summary

The present study confirms the results of Wegener et al. (1978), with a higher resolution study of the neutron vibrational spectrum of ethylene oxide clathrate. More accurate values are obtained for the librational modes of enclathrated ethylene oxide and several water translation modes are resolved in the spectrum. This data set should prove useful to computational chemists and physicists.

Our data also show that the mode assignments proposed by Bertie et al. (1975) on the basis of far-infrared absorption measurements on ethylene oxide clathrate are very likely incorrect. The modes in question are best attributed to water translational modes that appear fairly clearly in our neutron vibrational spectrum.

We also report for the first time the internal modes (higher frequencies) of ethylene oxide in ethylene oxide clathrate as measured by inelastic neutron scattering. These modes are (strongly) blue-shifted compared to gas phase ethylene oxide. This reflects strong repulsive guest-host interactions.

Preliminary data were collected for hydrogen in ethylene oxide clathrate. We show convincing evidence (shifted rotational mode of molecular hydrogen) that hydrogen is capable of diffusing in the small cages of ethylene oxide clathrate to produce what is -at the time of writing- probably the most stable hydrogen clathrate material. Further studies are planned on this material.

Appendix A

**METHANOL- INHIBITOR OR PROMOTER OF THE FORMATION OF GAS
HYDRATES FROM DEUTERATED ICE?**

Bobev, Svilen & Tait, Kimberly T. (2004)

Published in the American Mineralogist 89, 1208-1214

Abstract

Kinetic studies are reported of the effect of methanol on the rate of formation of CO₂- and CH₄-hydrates by means of *in situ* time-of-flight neutron powder diffraction. The experiments were carried out at temperatures ranging from 200 to 250 K and pressures up to 7 MPa. The samples were prepared from mixtures of ground, deuterated ice and deuterated methanol (up to 20 vol %), which were transformed *in situ* into CO₂- or CH₄-hydrates by pressurizing the systems with the corresponding gas. The observed rates of formation of hydrates are orders of magnitude higher than the rate of formation from pure deuterated ice under the same pressure and temperature conditions. Glycols and alcohols, methanol in particular, are long known as thermodynamic inhibitors of hydrate formation. Our study indicates that methanol can also act as a kinetic promoter for the formation of gas hydrates. Preliminary data suggest that the kinetics also depend strongly on concentration and the isotopic composition.

Introduction

The crystal structures, thermodynamic models, and engineering applications of CO₂- and CH₄-hydrates have been extensively studied under equilibrium conditions (Sloan, 1998a). Our knowledge of the kinetics of hydrate formation and decomposition on the other hand is rather limited. Studies of the formation and dissociation processes of hydrates are hindered by the complexity of the dynamic process and are often poorly reproducible. Typically, kinetic studies involve measurements of temperature and pressure changes of the gas and liquid phases to infer the properties and rate of structural changes of the hydrate phase. These experimental challenges, as recognized in some recent reviews on hydrate research (Ripmeester and Ratcliffe, 1998; Sloan, 1998b), are to directly measure the hydrate phase using techniques such as diffraction and NMR and Raman spectroscopy (Subramanian and Sloan, 1999). In-depth information about generalized kinetics models will be crucial in assessing such issues as the feasibility of *in situ* production of methane from the methane hydrate deposits at the ocean floor (Herzog et al., 1991; Saji et al., 1992). Kinetic models are eagerly sought for the systems CO₂(l)/water/CH₄-hydrate aiming at the development of the technology to simultaneously extract methane from the ocean-floor reserves and replace it with carbon dioxide. Therefore, studies of nucleation, growth, and dissociation of different hydrates at various conditions have received increasing attention in recent years.

The use of powder diffraction techniques, powder neutron diffraction in particular, proves to be a powerful tool for probing these systems. To date, X-ray and neutron powder

diffraction have been used for thermodynamic studies of carbon dioxide, propane, and methane hydrates, as well as for structural studies of methane and nitrogen hydrates (Davidson, 1984; Koh et al., 1996; Koh, 1997; Koh et al., 2002; Kuhs et al., 1996; Mak and McMullan, 1965; McMullan and Jeffrey, 1965; Stern et al., 1996). In particular, time-dependent neutron diffraction at a variety of temperatures and pressures has been effectively used to research the kinetics of gas hydrate formation and dissociation (Henning et al., 2000). These investigations were aimed at following the kinetics of formation and decomposition of carbon dioxide, methane, and other gas hydrates, using synchrotron X-ray radiation and neutron diffraction. Several publications on time-dependent kinetics of the hydrate formation and dissociation processes have already appeared in the literature (Halpern et al., 2001; Henning et al., 2000; Wang et al., 2002). More recently, the synthesis, structure, composition, and kinetic behavior of carbon dioxide hydrate were discussed in a comprehensive report based on X-ray and neutron diffraction, SEM, and residual gas analysis data (Circone et al., 2003; Staykova et al., 2003).

In the present study, we explore the effects of surfactants on the rate of formation of carbon dioxide and methane hydrate using neutron powder diffraction. This work provides direct observation of the *in situ* formation of carbon dioxide and methane hydrates from polycrystalline mixtures of deuterated ice and methanol, and evidence that methanol, in certain concentrations, accelerates tremendously the rate of the reaction from deuterated ice.

Experimental Details

The experiments were carried out using the High Intensity Powder Diffractometer (HIPD) instruments at both the Manuel Lujan Jr. Neutron Scattering Center (LANSCE-12) at Los Alamos National Laboratory, and at the Intense Pulsed Neutron Source (IPNS) at Argonne National Laboratory. The experiments were conducted in a pressure sample cell, originally designed and fabricated at Argonne National Laboratory (Figure A-1), and later duplicated at Los Alamos National Laboratory. The cell is made of an aluminum alloy and is intended for use with pressures up to 70 MPa at room temperature or below. Details on the sample cell design and fabrication can be found elsewhere (Henning et al., 2000).

Pressurized gas was introduced into the system through stainless-steel tubing that connects to standard gas cylinders with CO₂ (99.9%) and CH₄ (99.5%). The pressure was maintained at the desired level throughout the whole experiment by continual addition of gas. To monitor the pressure accurately, a digital pressure gauge was connected to the pressure cell.

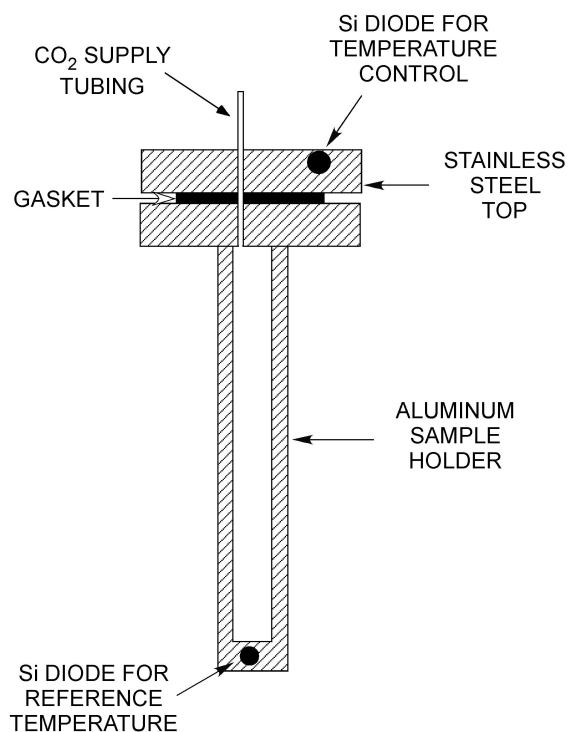


Figure A-1. A schematic drawing of the aluminum pressure cell. The cell is approximately 76 mm long and has an inside diameter of 8 mm.

Polycrystalline ice was prepared by freezing deuterated water (Aldrich or Cambridge-Isotope, 99.9%) and then crushing it with a mortar and pestle. The powder was then sieved through a stainless steel sieve (mesh -48) to obtain ice particles 300 μm and smaller. All these procedures were performed with caution and extreme care at around liquid nitrogen temperature to prevent the ice from melting. The powdered ice (kept submerged in liquid nitrogen to avoid frost deposits) was then inserted into the aluminum pressure cell, which had already been cooled to 77 K. The cell was subsequently closed (while keeping it in a small dewar flask filled with liquid nitrogen), and quickly mounted on the cold stage of a Displex closed-cycle helium refrigerator. Two silicon diodes for temperature control and for

reference (top and bottom of the cell as shown in Figure A-1) were attached and the assembly was then put into the sample chamber of the neutron diffractometer. As previously mentioned, the pressure cell was kept in liquid nitrogen as much as possible to prevent the ice from melting and to discourage condensation buildup on the outside of the cell. This is a concern because the incoherent scattering of the hydrogen would lead to a higher background in the diffraction data.

The same general procedure was followed for the preparation of several frozen water-alcohol mixtures with different concentrations, ranging from 20% by volume to 1% by volume. We started our studies with the most alcohol-rich system ($\text{CD}_3\text{OD}:\text{D}_2\text{O} = 1:4$), again by freezing it in liquid nitrogen. The frozen mixture was then quickly ground, sieved, and transferred into the aluminum cell, which was subsequently closed and attached to the cold finger of the Displex refrigerator (see above). Once the temperature was stabilized at ca. 200 K, a neutron diffraction pattern of the frozen, polycrystalline mixture was obtained to check for the presence of hexagonal ice and to make sure that it had not melted. Limited beam time precluded the completion of the whole series of experiments; those still to be made will be discussed in another paper.

Monitoring of the reaction pathway began with pressurizing the sample cell with CO_2 or CH_4 gas (maximum pressures up to 7 MPa) at temperatures of 250 K or below. Before the gas was introduced into the system, the cell was purged with helium and the gas supply lines were bled to get rid of unwanted air. The sample was allowed to stabilize a few degrees below the desired temperature. The gas was then introduced rapidly, and usually a

temperature increase of ~5–7 K was observed as indicated from the temperature reading difference between the two thermocouples (Figure A-1). The “fluctuation” in the temperature is most likely due to the pressurizing gas being at a higher temperature, along with the heat deposited in the system from the rapid formation of hydrate, which is an exothermic reaction (Henning et al., 2000). The temperature stabilized within a few minutes.

At the same time as the gas was being introduced, the shutters were open and time-of-flight powder diffraction data were obtained virtually in real time by creating a sequence of data collection runs, each with duration of approximately 15 minutes. The high neutron flux from both HIPD instruments allowed for fast data collection times. The spallation neutron source at LANSCE is pulsed at 20 Hz and ~100 μ A power, while the IPNS is pulsed at 30 Hz and ~15 μ A power. The time-of-flight neutron powder diffraction data were obtained by using the 90° data bank(s) on both systems. For comparison, the HIPD instrument at LANSCE-12 has a primary flight path (moderator-to-sample) of 9 m and a secondary flight path (sample-to-detectors) of 1 m. For the HIPD instrument at the IPNS, the sample position is located 5.5 m from the source and the sample-to-detectors distance is 1 m. Data analysis was done using the GSAS software package (Larson and von Dreele, 1994). The structural model employed in the refinements was adopted from an earlier *in situ* neutron diffraction study of CO₂ hydrates (Henning et al., 2000).

Results and Discussion

In nature or in laboratory experiments, gas hydrates typically form around 273 K (0 °C) and under moderate pressure (≤ 70 MPa). When the pressure is released, or the

temperature is increased, the hydrates decompose. The rate of decomposition varies with temperature and the type of guest molecule in the structure. In general, methane hydrates in particular decompose quickly and therefore have to be prepared *in situ* to prevent decomposition during transfer from one sample environment to another. *In situ* data may provide information at the atomic scale on the stability of the hydrate phases, as well as for the formation/decomposition kinetics. Neutron diffraction is a powerful tool for following structural changes that occur under these conditions. Neutrons are particularly useful for analyzing light elements such as hydrogen and O, since their penetrating power and lack of intensity fall-off with scattering angle allow for obtaining precise structural information on atomic positions, interatomic distances, and atomic displacement parameters under a variety of experimental conditions. Moreover, these experiments can be accomplished with much higher precision than can be done with X-ray diffraction methods.

Earlier experiments that utilized this technique have already demonstrated that one could successfully prepare and analyze gas hydrates *in situ* (Halpern et al., 2001; Henning et al., 2000; Wang et al., 2002). We are now extending these studies toward the kinetics of formation of CO₂ hydrate from systems containing methanol or electrolytes, with a long-term goal to prepare other types of gas hydrates, especially methane hydrate.

In abbreviated terms, the *in situ* monitoring of the structural transformations begins with collection a neutron diffraction pattern of the frozen ice or polycrystalline mixture of ice and alcohol stabilized at 200 K. This is done before the sample is pressurized to confirm that the ice (or the frozen mixture) has not melted, and to see if a clean powder pattern can be

observed. Hexagonal ice is clearly present in Figure A-2a, along with peaks from the aluminum sample cell. The positions of aluminum peaks occur at d -spacings of 2.34 Å and lower. After confirming that the ice did not melt during the setup phase, the cell was allowed to equilibrate at the desired starting temperature and then pressurized with CO₂ or CH₄ (pressures up to 7 MPa). Collection of time-resolved data (15–30 minutes) showed that peaks corresponding to type-I hydrate appear almost immediately (Figure A-2b). The reaction between the gas and the ice continues and at the end nearly 100% conversion can be achieved at certain conditions (Figure A-2c). Similar studies conducted at different temperatures have provided useful kinetic information on hydrate formation (Halpern et al., 2001; Henning et al., 2000; Wang et al., 2002).

The short data collection times and relatively low resolution of the HIPD instruments did not allow for a full Rietveld analysis of each data set (Larson and von Dreele, 1994). The lattice parameters of the three phases observed in the diffraction patterns, hydrate, ice, and aluminum were refined in the initial stages but then were fixed since the temperature and pressure of the sample did not change during the data collection. The atomic positions and thermal parameters, as determined in separate experiments for each temperature, were not allowed to vary during the refinements. Besides the six background parameters, only the histogram scale factor, an absorption coefficient, and the phase fractions were allowed to refine. The weight fractions were extracted from each refinement, adjusted for the gain of CO₂ in the solid phase, and the mole fractions of hydrate were calculated (Figure A-3).

As can be seen in Figure A-3, the rate of formation significantly depends on the temperature (Halpern et al., 2001; Henning et al., 2000; Wang et al., 2002). Also, these studies of the conversion of ice to hydrate suggest a two-stage process—initial reaction of CO₂ (or another hydrate-forming gas) with the so-called quasiliquid layer (QLL), followed by diffusion of the gas molecules through the layers of hydrate covering the ice particles (Halpern et al., 2001; Henning et al., 2000; Takeya et al., 2000; Wang et al., 2002). Importantly, direct observation of CO₂ hydrate formation on the surface of ice grains has also been reported by others (Hwang et al., 1990; Staykova et al., 2003; Stern et al., 1998a; Stern et al., 1998b), which supports the hypothesis that after diffusion through the hydrate layer, the gas molecules react with internal water in a QLL or “pre-melting” layer, rather than with ice molecules. This opens up a large area of possible kinetic studies of the CO₂ and other gas hydrate systems.

The next step was to complete similar *in situ* experiments, when instead of pure D₂O ice, a frozen mixture of D₂O with deuterated alcohols, glycols, electrolytes, etc. was reacted with CO₂ gas and the rate of the conversion to a CO₂ hydrate was determined in the same way as before. The accessible experimental data on alcohols and glycols are scarce and large gaps exist in the study of these systems. Furthermore, the latter are known as “thermodynamic inhibitors” of hydrate formation since addition of these compounds in certain concentrations moves the conditions required for hydrate formation toward lower temperatures and higher pressures (Koh et al., 2002; Majumdar et al., 2000; Mei et al., 1996 and references therein; Sloan, 1998a). The cases where thermodynamic inhibition is claimed

are all in V-L-H systems (vapor-liquid-hydrate), not in the V-I-H (vapor-ice-hydrate) systems that are the focus of our study. In fact, the petroleum and gas industry rely heavily on the technology of these “inhibitors” to prevent gas hydrate formation in pipelines. Although alcohols and glycols have been used for many years, little is known about the mechanisms of their inhibition in these V-I-H systems.

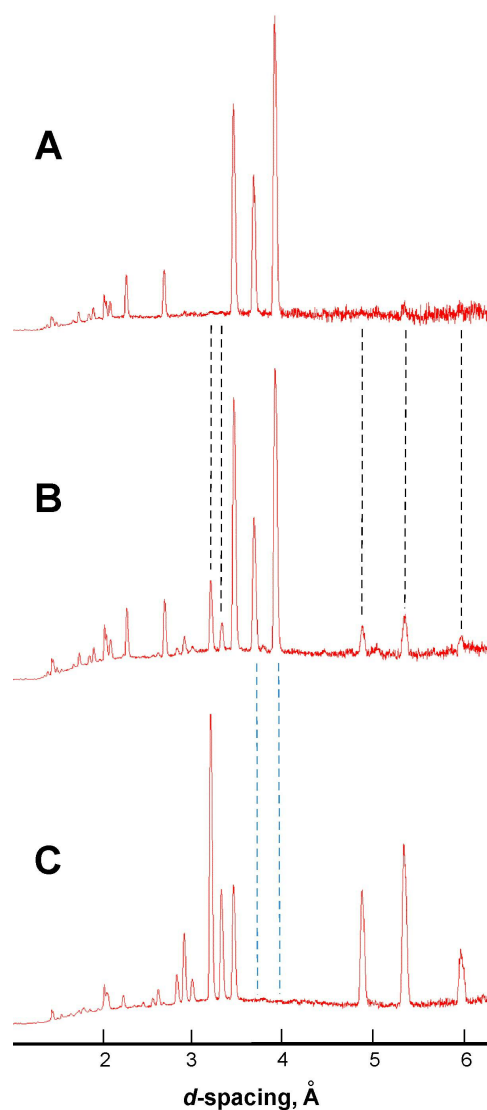


Figure A-2. Virtually real time monitoring (15 minutes per histogram) of the kinetics of formation of CO₂ hydrate from polycrystalline ice by *in situ* neutron powder diffraction. (a) Beginning of the reaction—neutron powder diffraction pattern of the D₂O ice (hexagonal structure, space group *P63/mmc*) at 200 K with no pressure; A-2b. Reaction in progress, system pressurized with either CO₂ or CH₄—neutron powder diffraction pattern of the mixture of hexagonal D₂O ice and type-I hydrate. This pattern can be viewed as a superposition of patterns (a) and (c), with relative intensities corresponding to the mole fractions of the two phases, respectively. A2-c. End of the reaction, i.e., all D₂O ice converted *in situ* to hydrate—neutron powder diffraction pattern type-I hydrate (primitive cubic structure, space group *Pm-3n*) at 200 K and 7 MPa He. The y-axis (not shown) represents the intensity in arbitrary units.

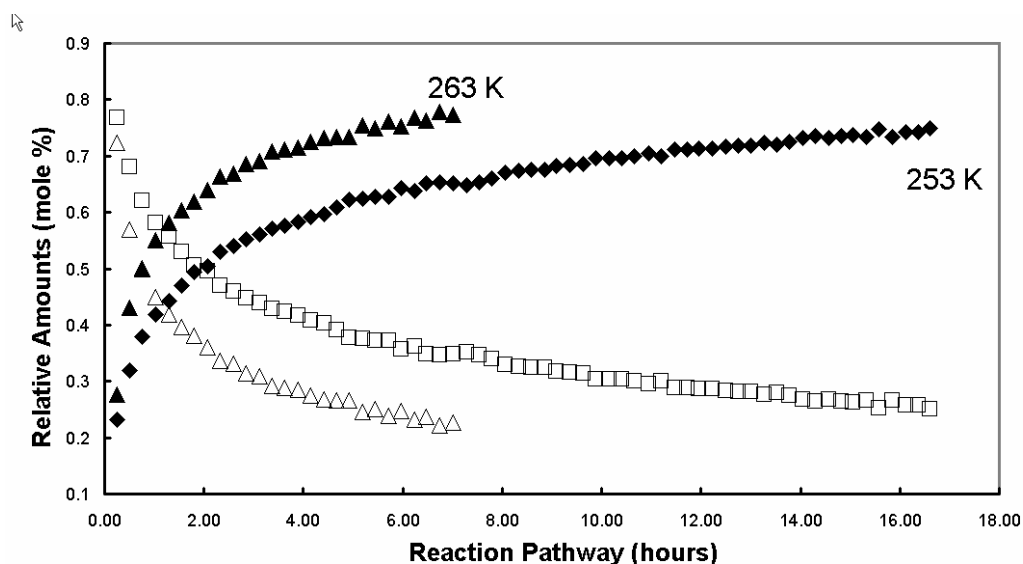


Figure A-3. Conversion of deuterated ice to carbon dioxide hydrate at 6 MPa at temperatures of 263 and 253 K (filled symbols represent the fraction of hydrate, open symbols stand for the fraction of ice). Each data point represents the mole fraction as refined from a 15 min histogram. Data from Henning *et al.* (2000), courtesy of A. J. Schultz.

With those ideas and background in mind, we undertook an *in situ* neutron diffraction experiment, starting with the simplest possible alcohol-methanol. Because hydrogen has a large incoherent scattering cross-section, while its heavier isotope deuterium has a large coherent scattering cross-section, both the water and methanol we used were fully deuterated. The diffraction pattern taken at 200 K, as plotted on Figure A-4a, shows only peaks corresponding to the structure of hexagonal ice. Indeed, this is what one should see at these *P-T* conditions, since the freezing point depression for the system in consideration (20% methanol by volume) is approximately 15°. Methanol on the other hand freezes at ~170 K, i.e., no peaks from solid methanol or other phases, excluding the Al peaks from the cell, should be observed in the powder pattern. Some controversy regarding the possibility of

methanol forming hydrate (just as THF or ethers do) has arisen in recent years. This stemmed from previous work on the water-methanol system, based on molecular spectroscopy and X-ray diffraction. Supposedly at high enough methanol concentrations and sufficiently low temperatures, even without pressure, water and methanol could form type-II hydrate with the methanol molecules occupying the large cages (Blake et al., 1991). Based on molecular dynamic simulations, others have argued ever since that conventional hydrate structures containing methanol as a guest species are inherently unstable at any temperature (Koga et al., 1994), a model which agrees with other experiments that show no evidence for the existence of any type of water-methanol hydrate (Murthy, 1999).

Claims that methanol and water form a monohydrate at liquid nitrogen temperature, and thus are unlikely to form any type of clathrate also exist, in apparent contradiction with FTIR spectra showing mixed methanol hydrates (Williams and Devlin, 1997).

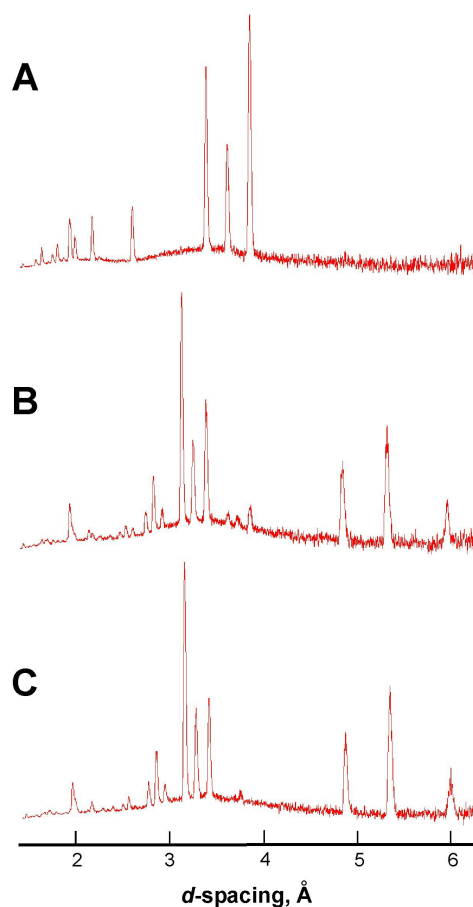


Figure A-4. *In situ* neutron powder diffraction patterns of a frozen $D_2O + CD_3OD$ mixture at 220 K with no pressure (a); and the corresponding patterns 20 minutes (b) and 40 minutes (c) after the system was pressurized with CO_2 at 250 K and 1.7 MPa. Due to the rapid conversion rates, the fractions of ice and hydrate could not be accurately refined. The y-axis (not shown) represents the intensity in arbitrary units.

Our *in situ* neutron diffraction patterns at 200 K unequivocally establish that only hexagonal ice is present in the system at these conditions. This observation might also support the hypothesis that methanol and water form some amorphous co-deposits, with the aim of a help gas at appropriate P - T conditions (Blake et al., 1991). Figure A-4b illustrates the changes in

the system in question only 20 minutes after the cell was pressurized with CO₂ gas at 1.7 MPa. The temperature rose quickly to approximately 250 K and the whole reaction essentially took place within a few minutes at that temperature. As can be seen from the graph, nearly all the ice peaks have disappeared and only the tips of the three strongest (at around *d*-spacings of 3.5 Å) peaks are still visible. After another 20 minutes, virtually only peaks from type-I CO₂ hydrate are present (Figure A-4c). Unfortunately, refining these data and extracting the mole fractions of ice and hydrate from both histograms is not possible because of the rapid conversion rates. Nevertheless, it gives a relative idea of how much faster the reaction is for the CD₃OD:D₂O mixture compared to the rate of the reaction of CO₂ gas with pure D₂O ice at comparable temperatures (253 and 263 K) and even at much higher pressure (Figure A-3). Evidently, it takes more than 20 hours for an 80 mol% conversion in the pure ice-carbon dioxide system, while a similar outcome is observed in the CD₃OD/D₂O-carbon dioxide system within 20 minutes.

To slow down the reaction for the sake of obtaining “time resolved” data, a new set of data was collected for the same system (CD₃OD:D₂O = 1:4), but at lower temperature, 200 K. Since the rate of formation of CO₂ hydrate from pure D₂O ice at 230 K and at 6 MPa has previously been reported (Henning et al., 2000) this low temperature experiment was also done at 6 MPa. This allowed for direct comparison between the results of these two experiments; Figure A-5 shows the conversion rates. The graph clearly demonstrates the dramatic effect of methanol on the rate of the formation—an increase of more than a factor of 3, not taking into account the difference in temperatures. Although the mole fractions were

extracted from the refined data, their standard uncertainties are large and this comparison is qualitative. The “error-bars” (not shown) are on the high side because, even at 200 K, the reaction takes place rapidly and the data from each of these seven 20 minute runs illustrate the average change. From that point of view, methanol, the long believed “thermodynamic inhibitor,” which is of immediate relevance to many branches of chemical technology, turns out to be an effective “kinetic promoter” of hydrate formation from polycrystalline ice.

Studies of thermodynamic and kinetic properties of various alcohol-water mixtures in the liquid phase are also receiving increasing attention. This interest has arisen from the proposed micelle-like structures of these systems, which are of biological significance (Koga et al., 1990; Mittal, 1977; Myers, 1988; Roux et al., 1978). However, information on the kinetic behavior of aqueous solutions of alcohols is scarce and incomplete, mostly due to the long crystallization times.

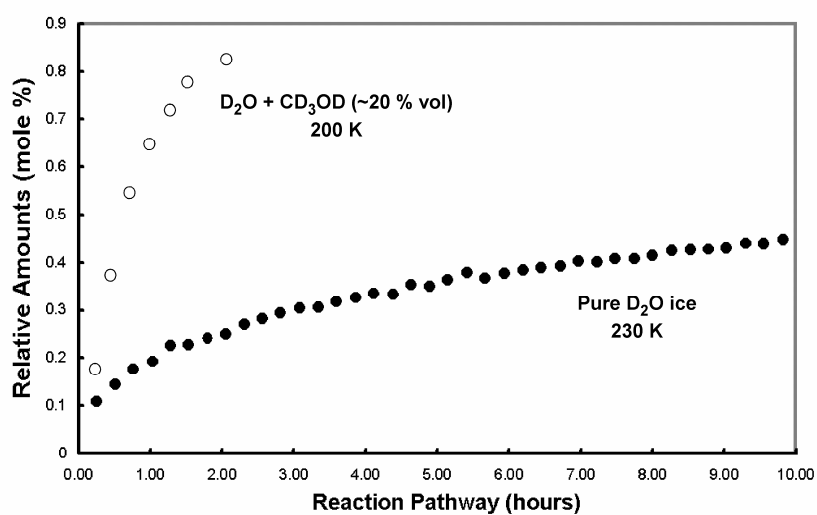


Figure A-5. Comparison between the rate of conversion of deuterated ice to carbon dioxide hydrate at 6 MPa and at 230 K and the rate of conversion of a mixture of deuterated ice and deuterated methanol to carbon dioxide hydrate at the same pressure and at a temperature of 200 K.

The limited availability of neutron beam time, along with technical difficulties precluded more detailed temperature-, concentration-, and/or isotope-dependent studies. Therefore, no general kinetic model can be proposed at this point. Our preliminary results suggest strong isotope and concentration effects, although these experiments suffer from relatively poor reproducibility. After all, as summarized in Sloan's section on kinetic inhibition (Sloan 1998a), the literature indicates that kinetic studies often appear to be system dependent. Hence, all these controversial and poorly reproducible results might be due to differences in the preparation techniques, small changes in the experimental conditions, and/or isotope effects (H vs. D). In our case, however, this often speculated possibility for "system dependence" as a possible reason can be ruled out. All experiments reported herein

were carried out more than once at different neutron sources and using different experimental setups. A more likely reason for the “system dependence” seems to be the lowered melting point of the $\text{CD}_3\text{OD}/\text{D}_2\text{O}$ mixture, which may cause melting (or rather softening) of the cell contents, especially the top part, during the processes of sealing and mounting on the cold finger of the Displex-refrigerator. Upon the subsequent active cooling (note that the top of the cell is directly attached to the cold finger), that part may freeze in the form of a “plug” and thus prevent the hydrate-forming gas from distributing freely within the volume of the whole cell. Subsequently, the substantial heat of hydrate formation, released within the first few minutes, causes large fluctuations in the temperature, and may contribute to unwanted melting of ice particles.

The direct comparison of the rates of formation from systems with partially and fully deuterated methanol seems to indicate that at similar concentrations, the partially deuterated reagent does not have the same influence over the kinetics as the fully deuterated one. Hydrogen-bonding effects certainly play an important role and substantial bonding of the methanol molecule might occur with the “cage wall,” presumably to the O atoms so that the guest species assumes a particular orientation within the hydrate cage. Williams and Devlin (1997) drew similar conclusions from their FTIR experiments of the formation of double hydrates of methanol and ether and ethanol and THF at cryogenic temperatures. Their work also reveals indications for substantial O-H and O-D interactions within the cages, much stronger than presumed by the van der Waals model for hydrate formation.

Deuterium, as discussed already, has a large coherent scattering cross-section while hydrogen absorbs strongly and scatters incoherently and hence is less suitable for neutron diffraction experiments. The necessity to work with deuterium-enriched samples is demonstrated in our first round of experiments on the effect of methanol on the kinetics of formation of methane hydrate at similar P - T conditions. These tested the feasibility of similar kinetic studies, when methane is used in place of carbon dioxide. Since commercial deuterated methane is expensive, regular and hydrogenous methane was used. These preliminary results, aside from the slightly higher background, as shown in Figure A-6, are encouraging and demonstrate again a high conversion rate, even at a temperature of 200 K and a pressure of 1.7 MPa. Previous *in situ* neutron diffraction experiments using regular CH_4 and pure D_2O ice revealed that the formation of methane hydrate from deuterated ice obeys the same general kinetic behavior, although at significantly slower rates (Wang et al., 2002).

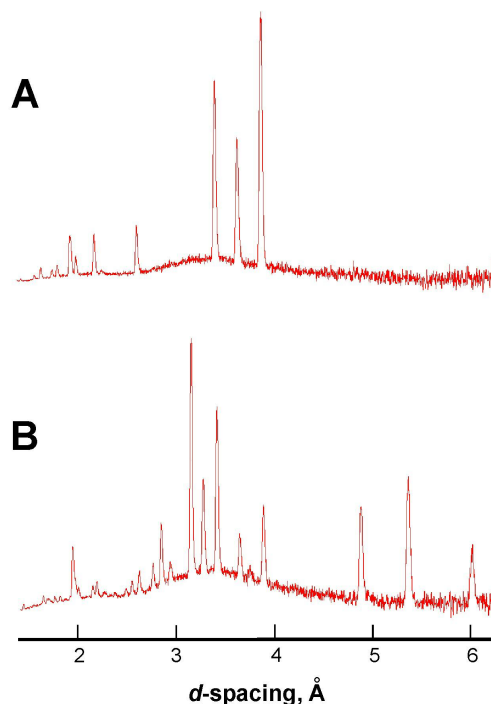


Figure A-6. *In situ* neutron powder diffraction patterns of a frozen $D_2O + CD_3OD$ mixture at 200 K with no pressure (a); and the corresponding pattern 90 minutes (b) after the system was pressurized with CH_4 at 200 K and 1.7 MPa. The higher background is due to the presence of H (large incoherent scattering cross-section). The y-axis (not shown) represents the intensity in arbitrary units.

That study reported 70% conversion after 24 hours at a CH_4 pressure of 7 MPa, and at 273 K, while our experiment with the frozen CD_3OD/D_2O mixture (1:4 by volume) realizes nearly the same conversion efficiency in only 90 minutes at a temperature of 200 K and a pressure of 1.7 MPa!

In contrast to the preceding experiment with regular CH_4 and pure D_2O ice (Staykova et al. 2003; Wang et al. 2002), our data was hampered by high backgrounds, so that the subsequent Rietveld refinements are not of good quality. Sample decomposition also seems to be rapid and all hydrate peaks completely disappear within minutes.

Although the effect of methanol on the kinetics of formation and decomposition of CO₂ and CH₄ hydrates is clearly observed, many questions still remain to be answered, of which the most important one is: where are the methanol molecule(s) in the hydrate structure? It is unlikely that the enhanced kinetics are due to localized melting during the exothermic reactions (e.g., locally elevated temperatures and reaction of gas with liquid water-methanol/ice mixture/slurry instead of with solid ice), yet the possibility for that and for the presence of liquid methanol cannot be completely excluded. One might also speculate that if the ice and methanol formed some sort of composite crystalline or amorphous phase at liquid nitrogen temperatures, then raising the temperature to a point where the methanol melts might leave behind a highly porous residual ice structure. In this case, the apparent increase in kinetics could simply be due to a much higher surface area of the ice sample (i.e., the rate depends on the texture of the ice, which in turn is affected by how it was made and handled). Other mechanisms for the promoted kinetics might include mass transfer of guests to the growing hydrate or heat transfer away from the growing crystals. Thus, the apparent increase in the conversion rate of the frozen methanol-water mixture could be due to an increased heat capacity in the system. In this scenario, addition of methanol increases the heat capacity of the overall system, and as a consequence, the heat of formation is deposited into the methanol-rich phase. If the global rate were governed by heat removal, then there would be an apparent increase in the rate since the heat of formation need not be transferred to the system boundary for hydrates to form. Along these lines, if liquid methanol is in contact with the vessel walls, then the heat transfer coefficient could be

increased leading to a higher heat flux (and more rapid apparent kinetics). We cannot eliminate this possibility, because we do not have strong evidence that methanol is frozen at the P - T conditions of the experiment. However, the heat capacities for ice and methanol are not sufficiently different to explain why simply absorbing the hydrate heat of formation has such a strong promoting effect on the methanol.

Another explanation for these rapid rates of formation when methanol is present in the system is to assume methanol is a “help gas.” Some previously mentioned FTIR experiments indicate a substantial bonding of the methanol molecule with the “cage walls” (Williams and Devlin 1997). These hydrogen bonds, presumably to the O atoms that make up the hydrate frameworks might constrain a particular orientation of the methanol molecule within the hydrate cage. These interactions within the cages will be much stronger than the typical van der Waals bonding in simple hydrates and may contribute to the spectacular magnitude of the promoting effect.

Appendix B
HIGH-P/LOW-T NEUTRON SCATTERING OF HYDROGEN INCLUSION
COMPOUNDS—PROGRESS AND PROSPECTS

Yusheng Zhao,^{1*} Hongwu Xu,^{1,2} Luke L. Daemen,¹ Konstantin Lokshin,^{1,4} Kimberly T. Tait,¹ Wendy L. Mao,¹ Junhua Luo,¹ Robert P. Currier,³ and Donald D. Hickmott²

¹ Los Alamos Neutron Science Center

² Earth and Environmental Sciences Division

³ Chemistry Division

Los Alamos National Laboratory

Los Alamos, NM 87545, U.S.A.

⁴ Department of Materials Science and Engineering,
University of Tennessee, Knoxville, TN 37996

*Corresponding author: yzhao@lanl.gov

Submitted to the *Proceedings of the National Academy of Sciences*

December 2006

Abstract

Alternative energy resources such as hydrogen and methane gases are becoming increasingly important for the future economy. To realize their industrial-scale utilization, however, major scientific and engineering breakthroughs are needed. For example, a major challenge to use hydrogen is to develop suitable materials to store it at a variety of conditions. This requires systematic studies of the structures, stability, and kinetics of various hydrogen-storing compounds. Neutron scattering is particularly useful for these studies, because of the much larger scattering capability of hydrogen (and deuterium) and other light elements by neutrons than by X-rays. We have developed high-pressure (P) low-temperature (T) gas/fluid cells in conjunction with neutron diffraction and inelastic neutron scattering instruments at the Los Alamos Neutron Science Center (LANSCE). These techniques enable *in-situ* and *real-time* examination of gas uptake/release processes and allow high-resolution time-dependent determination of changes in crystal structure and related reaction kinetics. We have successfully used these techniques to study the formation of methane and hydrogen clathrates, a group of inclusion compounds consisting of host frameworks of hydrogen-bonded H_2O molecules with guest hydrogen molecules trapped inside the cages. Our results reveal that clathrate can store up to four hydrogen molecules in each of its large cages (and one molecule in the small cages) with an intermolecular H_2 - H_2 distance of only 2.93 Å. This distance is much shorter than that in the solid/metallic hydrogen (3.78 Å) obtained at higher pressure and/or lower temperatures, suggesting a strong densification, or pressurizing/freezing, effect that the clathrate framework may exert on the

enclosed hydrogen molecules. The framework-pressurizing effect is striking and may exist in other inclusion compounds such as the recently discovered metal-organic frameworks (MOFs). Owing to the enormous variety and flexibility of their frameworks, inclusion compounds may offer superior properties for storage of hydrogen and/or hydrogen-rich molecules (such as $\text{CH}_4(\text{H}_2)_4$), relative to current state-of-the-art hydrogen storage compounds. We have begun investigation of the hydrogen storage properties of MOFs using high- P /low- T neutron scattering methods, and our preliminary results on two MOF compounds, $\text{Cu}_3[\text{Co}(\text{CN})_6]_2$ and $\text{Cu}_3(\text{BTC})_2$ (BTC = benzenetricarboxylate), demonstrates that these techniques are equally well suited to study MOFs and other inclusion compounds, especially for locating the incorporated D_2 molecules and characterizing their interactions with the host frameworks.

Introduction

Ever-increasing fossil energy consumption and associated global environmental concerns have provoked intensive searches for alternative energy resources. Gas hydrates (clathrates) have been proposed as one of these sources of energy; they are crystalline compounds in which a gas molecule guest is physically incorporated into hydrogen-bonded, cage-like ice host frameworks. Natural clathrates have been found worldwide in permafrost and in ocean floor sediments, as well as in the outer solar system (the moon, comets, Mars, satellites of the gas giant planets) and contain primarily methane (CH_4), as well as minor amounts of ethane (C_2H_6), propane (C_3H_8), and other gases (isobutene, normal butane, nitrogen, carbon dioxide and hydrogen sulfide) (Sloan, 1998a). Naturally-occurring hydrates are difficult to study, and much remains to be learned about their crystal structures, bonding mechanisms, thermodynamics, chemical and mechanical stability, reaction with sediments and kinetics of formation and decomposition. Hydrogen in the form of H_2 , the most abundant gas in the universe, is considered to be one of the most promising alternatives to fossil energy, because it burns cleanly and has high energy efficiency (Schlapbach and Zuttel, 2001). However, incorporation of large amounts of hydrogen into a material that ensures both safe storage and ease of release for energy conversion is one of the most daunting challenges to the realization of the hydrogen economy. The Department of Energy has set targets for hydrogen storage of 6.0 wt% and/or 1.5 kWh/Liter by 2010 and 9.0 wt% and/or 2.7 kWh/Liter by 2015. Conventionally, hydrogen has been stored as compressed gas or cryogenic liquid. However, compressed gas stores low contents of hydrogen (only ~1

wt% at 200-300 bars), and cryogenic liquid requires significant energy (i.e. high cost) to maintain cryogenic conditions. In addition, both methods have safety issues and are not yet practical for mobile applications. Solid-state storage is also being considered as a possible safe and effective way of routinely handling hydrogen, e.g., in the form of metal hydrides (such as LiBH_4) (e.g., Grochala and Edwards, 2004) and via carbon nanotube absorption. Solid-state forms have different properties in terms of balancing high energy density with easy reversibility of adsorption/desorption. For instance, the hydrogen content of LiBH_4 is high (18 wt%), but it can only release hydrogen at high temperatures (as high as 900 K). As an alternative, we focus on three-dimensional frameworks of inclusion compounds with cages/cavities that can host hydrogen molecules. Particularly, we emphasize *absorption* rather than *adsorption* such that H_2 -storage materials may be operational at ambient conditions once stabilized. Inclusion compounds are promising materials due to the vast variety of possible structures and the ability to manipulate their hydrogen storage properties. In addition to energy applications, studying storage of hydrogen in inclusion compounds (specifically clathrates) may provide insights into the nature of hydrogen-rich atmospheres in the large-body interstellar ice embryos postulated to exist during planet formation (Sandford et al., 1993; Stevenson, 1999). Moreover, unraveling the gas encapsulation mechanisms in natural systems (such as methane clathrate) may lay the foundation for designing new synthetic materials for storage of hydrogen and other gases.

As the lightest element, the hydrogen atom contains only one electron and thus has the weakest X-ray scattering cross-section of all the elements. In contrast, the scattering

power of neutrons does not vary with the number of electrons in an element, and neutron diffraction is much more sensitive to the positions of hydrogen (or its isotopes, such as deuterium) and other light elements, making neutron scattering well suited for studying hydrogen- or other gas-containing materials. In addition, as neutrons are more penetrating than X-rays, one can probe samples inside high-pressure vessels, within refrigerators and furnaces, or measure deeply buried local structures within a bulk host material. Hence, neutron scattering in conjunction with variable temperature and pressure capabilities is a powerful tool to monitor the gas uptake/release processes in inclusion compounds.

Here we report neutron diffraction studies of clathrate hydrates, a class of framework compounds consisting of hydrogen-bonded water molecules (Lokshin and Yusheng, 2005; Lokshin et al., 2004; Mao et al., 2002; Sloan, 1998a). We also report preliminary results on hydrogen storage measurements of $\text{Cu}_3[\text{Co}(\text{CN})_6]_2$ and $\text{Cu}_3(\text{BTC})_2$ (BTC = benzenetricarboxylate), two metal-organic framework (MOF) compounds, and discuss prospects for extending neutron diffraction studies to other inclusion compounds (e.g., Rowsell and Yaghi, 2005).

Results and Discussion

We carried out *in-situ* and *real-time* neutron diffraction and inelastic neutron scattering using High-Pressure Preferred-Orientation (HIPPO) diffractometer and Filter Difference Spectrometer (FDS), respectively, at LANSCE. Earlier experiments were to investigate the stability and crystal structures of natural gas hydrates; especially methane, ethane and mixed gas hydrates at various pressure and temperatures, synthesized both *in situ*

and *ex situ* (Figure A-7). For *in situ* measurements, polycrystalline ice was prepared by freezing water, crushed with a mortar and pestle at liquid nitrogen temperatures and then sieved through a stainless steel mesh to obtain ice particles 300 μm or smaller. The powdered ice was then inserted into the pressure cell; the gas was introduced to the ice and experiments at various pressures and temperatures were performed. To avoid incoherent scattering of H, which contributes to the backgrounds of diffraction patterns, deuterated water and gases were used for the experiments. For example, methane clathrate has been synthesized *in situ* at various pressure/temperature/time conditions (Figure A-7, insert).

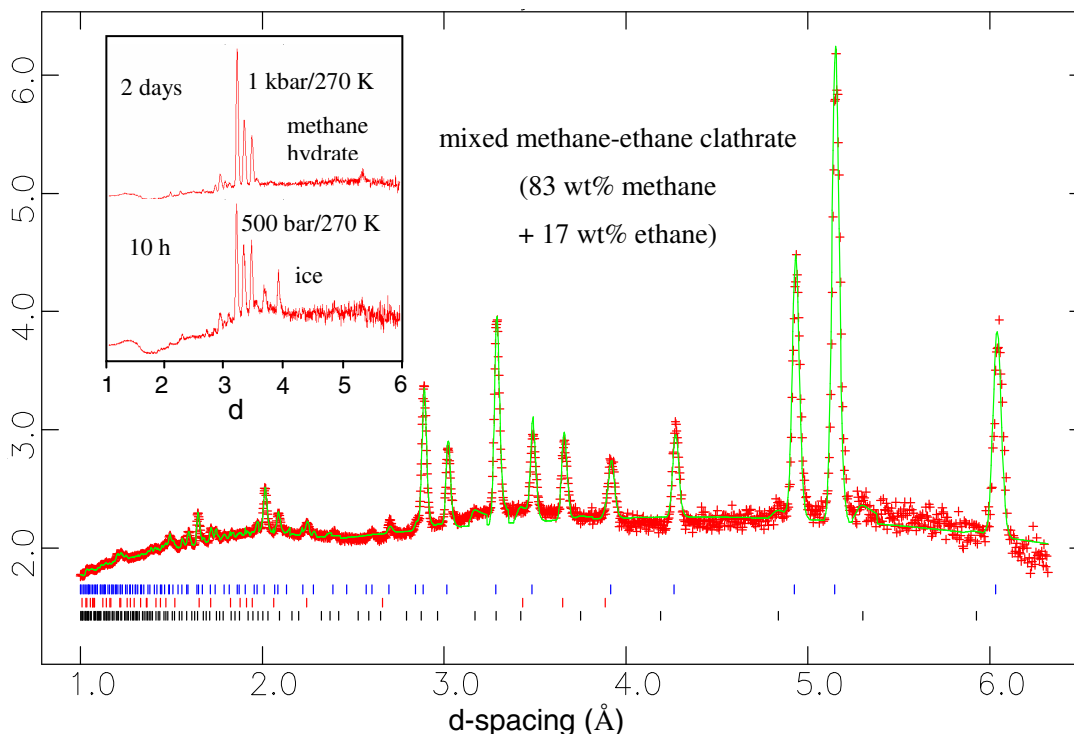


Figure A-7. Fitted neutron diffraction pattern of a mixed methane-ethane sI clathrate (82.93 wt% methane + 17.07 wt% ethane) with minor sII phase and D₂O ice. Data are shown as red plus signs, and the green curve is the best fit to the data. Tick marks below the pattern show the positions of allowed reflections (blue – sI phase; red – ice; black – sII phase). The insert shows neutron patterns of methane clathrate formed from ice and D₂ *in situ* in the Al pressure cell. Note that formation of methane clathrate was not complete even after 10 h at 500 bar and 270 K, indicating sluggish formation kinetics compared with hydrogen clathrate (see below).

Our results indicate that the formation kinetics of methane clathrate is much more sluggish than that of hydrogen clathrate (see below). Another method was to synthesize the samples *ex situ* in a high-pressure synthesis apparatus and then load them into the pressure cell. This method reduces the time needed in the neutron beam and additionally portions of the samples could be used for other analyses, such as electron microscopy, mass

spectrometry, Raman spectroscopy and X-ray diffraction. A methane-ethane clathrate sample (Figure A-7) was prepared *ex situ* in an apparatus described previously (Stern et al., 1996) over 26 hours with a temperature range of 254-290 K and a pressure range of 20-35 MPa. The sample was then measured on HIPPO at 200K and ambient pressure. The final gas concentrations (methane 82.93 wt %, ethane 17.07 wt %, normalized) were measured by gas chromatography, which varied slightly from the initial gas of 80 wt % methane and 20 wt % ethane.

We conducted *in situ* synthesis of deuterium clathrate D_2 - D_2O and monitored its stability as a function of pressure and temperature (Lokshin et al., 2004). Deuterium clathrate was obtained under 220 MPa of D_2 pressure in the temperature range 200-270 K, and neutron data were collected during cooling from 200 to 40 K and during heating from 40 to 200 K at ambient pressure. We also used powdered ice (500 μm in diameter) instead of water as a source of D_2O , and our results showed that the formation of deuterium clathrate from ice powder is rapid due to its larger surface area and framework porosity (Figure A-8) (Lokshin & Zhao, 2005) (Given the formation of hydrogen clathrate at relatively low pressures, it is possible that large amounts of molecular hydrogen may be entrapped in interstellar ices in the form of the clathrate). The deuterium clathrates synthesized have sII structure space group $Fd3m$), and all the patterns were analyzed using the Rietveld method. The sII framework contains eight hexakaidecahedral (6^45^{12}) cages and 16 smaller dodecahedral (5^{12}) cages per unit cell. The number of D_2 molecules and their distribution in the cages vary systematically with temperature and pressure (Figure A-9). Below 50 K, the

guest D_2 molecules are localized; with one D_2 occupying each of the small cages and four D_2 molecules in each large cage arranged in a tetrahedral geometry with a D_2 - D_2 distance $2.93(1) \text{ \AA}$. Interestingly, the four D_2 molecules in the large cages are oriented towards the centers of the hexagons formed by the framework water molecules, presumably due to the energetic need of minimizing electrostatic repulsion. On the other hand, the distance between the four tetrahedrally arranged D_2 molecules (2.93 \AA) is small – much shorter than that for solid/metallic hydrogen (3.78 \AA) (Ishmaev et al., 1983). With increasing temperature, D_2 molecules become delocalized, as represented by a uniform distribution of their scattering densities on the surface of a sphere. Correspondingly, the number of D_2 in the large cage gradually decreases to $2.0(2)$ as temperature rises to 163 K at atmospheric pressure. In contrast, the occupancy of the small cage is constant at one D_2 molecule throughout the temperature range, which is believed to be required for stabilization of the clathrate structure. The clathrate structure tends to collapse as the D_2 starts to escape from the small cage. Upon cooling at 200 MPa , formation of the tetrahedral D_2 cluster in the large cage is complete at 180 K , consistent with the fact that increasing pressure stabilizes clathrate hydrates. Moreover, the distribution of the four D_2 molecules appeared to be similar to that at atmospheric pressure below 70 K , when the maximum amount of D_2 was incorporated into the clathrate framework.

This localization-delocalization behavior of D_2 in clathrates is unusual. In particular, multiple D_2 molecules occupying one cage can be delocalized into freely rotating state with increasing temperature. Further, the intermolecular distance between the four localized D_2

molecules (2.93 \AA) is even smaller than that in solid/metallic hydrogen (3.78 \AA) that was produced at extremely low-temperatures and/or high-pressures. This D_2 -densification behavior is striking and suggests a strong pressurizing effect that the clathrate framework exerts on the enclosed hydrogen. Similar behavior has been revealed in H_2 -adsorbing metal-organic frameworks (MOFs), where the intermolecular H_2 distance, obtained by theoretical simulation, can be as short as 3.0 \AA (Yildirim and Hartman, 2005).

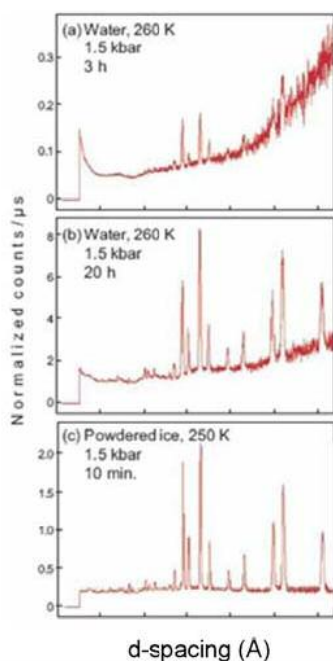


Fig. 2

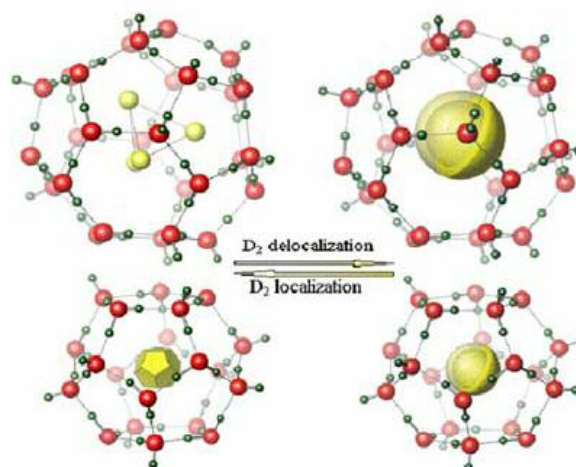


Fig. 3

Figure A-8. Neutron diffraction patterns of deuterium clathrates produced from (A, B) water and (C) powdered ice, at approximately the same P - T conditions (Lokshin & Zhao, 2005). Note that the formation kinetics of D_2 -clathrates formed from ice powder is much faster than from water.

Figure A-9. Structural view of D_2 distribution in the large (top) and small (bottom) cages of deuterium clathrate (Lokshin et al, 2004). Oxygen atoms are shown as red spheres, deuterium framework atoms—green, and guest D_2 molecules—yellow. Note that the $D_2 \cdots D_2$ separation is the distance between the centers of mass of the two D_2 molecules. Below 50 K , the guest D_2 molecules are localized (left). With increasing temperature, the D_2 molecules can rotate more freely, yielding a nearly spherical D_2 density distribution (right).

Moreover, a recent high-resolution transmission electron microscopy (HRTEM) study shows that materials (e.g., iron carbide, iron and cobalt) encapsulated in carbon nanotubes exhibit severe lattice deformation similar to that under pressures of up to ~40 GPa (Sun et al., 2006; Wang and Zhao, 2006). Hence, the pressurizing effect may exist in many materials that have nanosized cages/tubes/cavities in which guest phases are encapsulated. Since storage of H₂ usually requires pressure (e.g., compressed H₂ gas), this phenomenon suggests that it is possible to pressurize H₂ into the nanopores of inclusion compounds via *absorption*, and ideally the frameworks themselves can be stabilized at ambient conditions. The absorptive (versus adsorptive) nature of H₂ with appropriate binding energies would allow incorporation of more H₂ into the frameworks while still maintaining relative fast kinetics of H₂ uptake/release. Hence, inclusion compounds with appropriate topologies and cavities may offer a new methodology for H₂ storage.

Our *in situ* neutron diffraction studies of hydrogen clathrates have demonstrated the great potential of using the nanocages within inclusion compounds as hosts for hydrogen. Since the conventional clathrate hydrates have only a limited number of framework types (*i.e.*, sI, sII and sH) (Sloan 1998), this limits the ability to tune their cages to encapsulate hydrogen and hydrogen containing molecules (e.g., CH₄(H₂)₄). However, structural variations in clathrate hydrate frameworks are known. One important class of clathrate-variants is the semi-clathrates, in which, a portion of the guest molecule chemically binds to the host framework, effectively replacing a water molecule in the lattice. The remainder of the guest is then free to interact with the lattice through *van der Waals* forces and/or

hydrogen bonding. For example, many of the short chain (alkyl) quaternary ammonium salts form stable, ambient pressure semi-clathrates (tetra-n-butylammonium fluoride forms a semi-clathrate that melts at 298 K; and tetra-n-butyl ammonium hydroxide semi-clathrate melts at 303 K). The increased guest-lattice interactions in the semiclathrates not only enhance thermodynamic stability; it also creates extended structures around the central cage containing sites that can be exploited for hydrogen enclathration. The distorted and enlarged cages are able to trap more hydrogen molecules so that the semi-clathrates will be effective as hydrogen storage materials, due to enhanced stability and capacity.

We are also exploring other families of inclusion compounds, including the recently discovered metal-organic frameworks (MOFs), which are among the most promising hydrogen storage candidates (e.g., Rowsell & Yaghi, 2005). Through systematic tuning of organic ligands and metal-oxygen clusters at various synthesis conditions, one may obtain framework types with various sizes and shapes of nanopores. Compared to aluminosilicate zeolites, MOFs are much lighter (with densities as low as 0.2 g/cm^3) and, in many cases, more porous (with specific surface areas of up to $4500\text{-}8000 \text{ m}^2/\text{g}$). Moreover, the organic functional groups possess such surface/interface properties as chirality and hydrophilicity, which create favorable sites for hydrogen uptake. Likewise, incorporation of “naked” metal cations (such as Mg^{2+} and Cu^+) makes the originally neutral MOF frameworks ionized, thereby polarizing the dihydrogen molecules and resulting in enhanced H_2 sorption. The hydrogen binding energy for these sites are approximately 5 kJ/mol (e.g., Sagara et al., 2005), small enough to enable fast hydrogen uptake/release. In addition, unlike clathrates,

the nanoporous frameworks of MOFs are fairly robust – even stable at ambient pressure and high temperatures (*e.g.*, 673 K for MOF-5, $\text{Zn}_4\text{O}(\text{BDC})_3$, BDC= benzenedicarboxylate). Thus these compounds are inherently superior as hydrogen storage materials for mobile applications. A number of MOFs have been found to uptake high amounts of H_2 at low temperature (> 77 K) and/or high pressure (< 10 MPa). For example, MOF-5 can hold up to 4.5 wt% hydrogen at 78 K (Rosi *et al.*, 2003). Further studies are still needed to unravel the mechanisms of hydrogen uptake/ release in these materials (*e.g.*, the relative roles of absorption *vs.* adsorption). *In-situ* neutron scattering of MOFs with various pore sizes and shapes at different pressure/ temperature conditions will be particularly useful.

Using the high-*P*/low-*T* cell designed for the clathrate studies, we have recently conducted neutron diffraction experiments on $\text{Cu}_3[\text{Co}(\text{CN})_6]_2$, an MOF compound, at 10 MPa of D_2 from 40 to 200 K (Figure A-10). This compound is a Prussian blue analogue (space group *Fm-3m*), in which 1/3 of the $[\text{Co}(\text{CN})_6]_3^-$ sites are vacant, resulting in an aperiodic system of nanopores throughout the structure (Figure A-10B).

Rietveld analysis (Figure A-10A) shows that the cell volume increases from 990.5(4) \AA^3 under vacuum to 993.5(3) \AA^3 at 10 MPa both at 100 K (Figure A10-A, insert), implying incorporation of significant amounts of D_2 into the nanoporous framework. Furthermore, difference Fourier nuclear density maps reveal that the D_2 molecules mainly occupy the interstitial ($1/4, 1/4, 1/4$) water sites (Figs. A-10B, A10-C and A10-E) with some possibly associated with the exposed Cu cations (Figure A-10D, although data with higher resolution

are needed to locate these Cu-related sites). We have also studied the interaction of H₂ with another MOF, Cu₃(BTC)₂, at 40-100 K using inelastic neutron scattering (Figure A-11).

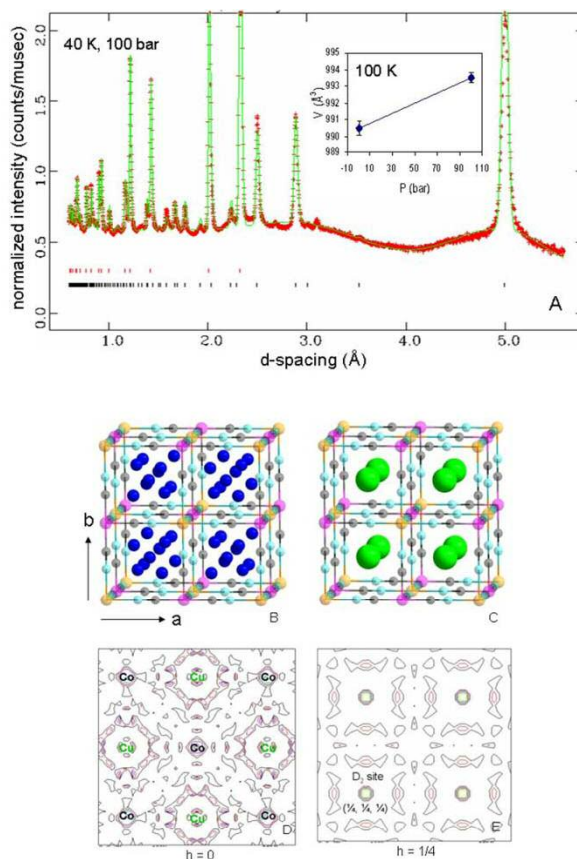


Figure A-10 (A) Fitted neutron diffraction pattern of Cu₃[Co(CN)₆]₂ at 40 K and 10 MPa of D₂ pressure. Data are shown as red plus signs, and the green curve is the best fit to the data. Tick marks below the pattern show the positions of allowed reflections (first row – Al cell; second row – sample). The insert shows increased unit-cell volume under 10 MPa of D₂ pressure at 100 K. (B) Crystal structure of Cu₃[Co(CN)₆]₂·9H₂O at ambient condition (brown – Cu; pink – Co; black – C; light blue – N; dark blue – water). (C) Crystal structure of Cu₃[Co(CN)₆]₂·nH₂ (green – H₂) showing H₂ at the (1/4, 1/4, 1/4) site (the relatively large green sphere illustrates free-rotation of H₂ molecules in the cages). (D,E) Difference Fourier nuclear maps showing that the incorporated D₂ molecules mainly occupy the original water site (1/4, 1/4, 1/4) (D) with some possibly associated with Cu (E). The residual intensities at the Co and Cu sites are due to the limited resolution of our data and the strong scattering of Co and Cu.

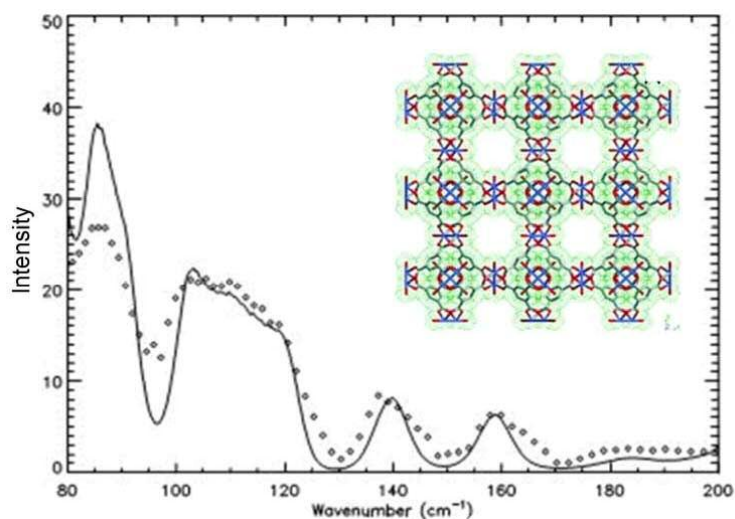


Figure A-11. Low frequency neutron vibrational spectrum of $\text{Cu}_3(\text{BTC})_2$ with its crystal structure shown as an insert. $\text{Cu}_3(\text{BTC})_2$ has three H_2 equivalents adsorbed at 40 K. The curve is a maximum entropy reconstruction of the spectrum. It enhances some details that are present in the data (dots) but may be not easy to see.

This framework is composed of di-copper and BTC units via corner-linking, forming nanosized channels along the a -axes (see the insert in Figure A-11). The most striking feature of the neutron vibrational spectrum is the displacement of the rotational level of hydrogen from 118 cm^{-1} down to 86 cm^{-1} – a result of guest-host interactions between H_2 and the framework. Hindering of the $0 \rightarrow 1$ rotation in molecular hydrogen upon adsorption in a number of MOFs (IRMOF-1, IRMOF-8, IRMOF-11, MOF-177) has been observed previously (Rowsell et al., 2005), with shifts from the free rotor value (118 cm^{-1}) to the $80\text{-}90 \text{ cm}^{-1}$ range. This large shift corresponds to the largest barrier to rotation and the strongest binding site for molecular hydrogen. The broad band from 95 cm^{-1} to 125 cm^{-1} is resolved into at least three peaks and corresponds to the occupation of other, weaker binding sites for which the $0 \rightarrow 1$ transition is less strongly hindered. The peak around 160 cm^{-1} has been

reported by previous workers (e.g., ref Rowsell et al., 2005) and its origin is obscure. It is possible that the 0->2 rotational transition might occur below twice the frequency of the fundamental owing to the existence of the rotational barrier which affects dramatically the energy level spacings compared to the free rotor situation (Nicol et al., 1988). Additional vibrational spectra of this compound are being collected with hydrogen injected at high pressure, and more rigorous analysis will yield the binding energies of H₂. Hence, *in situ* neutron diffraction and inelastic scattering are complementary and are well suited for studies of MOFs and other hydrogen bearing inclusion compounds.

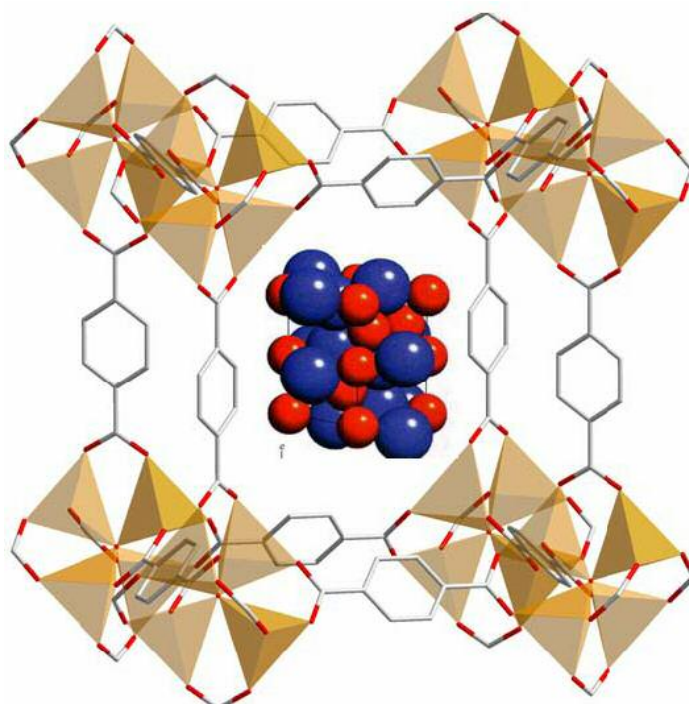


Figure A-12. Structure diagram of a potential hybrid material of the metal-organic framework (MOF) with the $\text{CH}_4(\text{H}_2)_4$ molecular compound encapsulated into its cage. MOF consists of metal-oxygen clusters (tetrahedra) on the vertices of the lattice and organic linker molecules (hexagons) along its edges, which largely define the size and shape of the cage. Blue balls in $\text{CH}_4(\text{H}_2)_4$ represent CH_4 , and red balls represent H_2 .

Another area of future research is to develop hybrid hydrogen storage materials with *absorptive* hydrogen binding. Recent studies using the diamond-anvil cell technique indicate that hydrogen can react with other simple molecular systems (such as CH_4) to form *van der Waals* compounds at moderate pressures (Mao and Mao, 2004). One compound, $\text{CH}_4(\text{H}_2)_4$, forms at 360 MPa and 86 K and contains 33.4 wt% hydrogen, the highest hydrogen content of any known compound (Mao et al., 2005). Rather than using the external pressure to produce this compound, one may be able to rely on the inner pressure within the cavity of

MOFs (Figure A-12). The same approach may be used for incorporation of other alkane and hydrocarbon molecules into MOFs. The strong pressurizing effect within the nanopores of these hybrid phases increases the likelihood of their stability at more accessible P - T conditions, and thus their use for practical hydrogen storage. Of course, the technical challenge is to design MOFs that have cages suitable in both size and shape for $\text{CH}_4(\text{H}_2)_4$ and other molecules. Given the flexibility of the synthetic chemistry of MOF systems, the successful preparation of hybrid compounds is likely. As in the case of hydrogen clathrates, studies of hybrid hydrogen-storage phases require detailed analyses of their structures, kinetics and stability relations, where *in situ* neutron diffraction under high- P and low- T conditions is valuable.

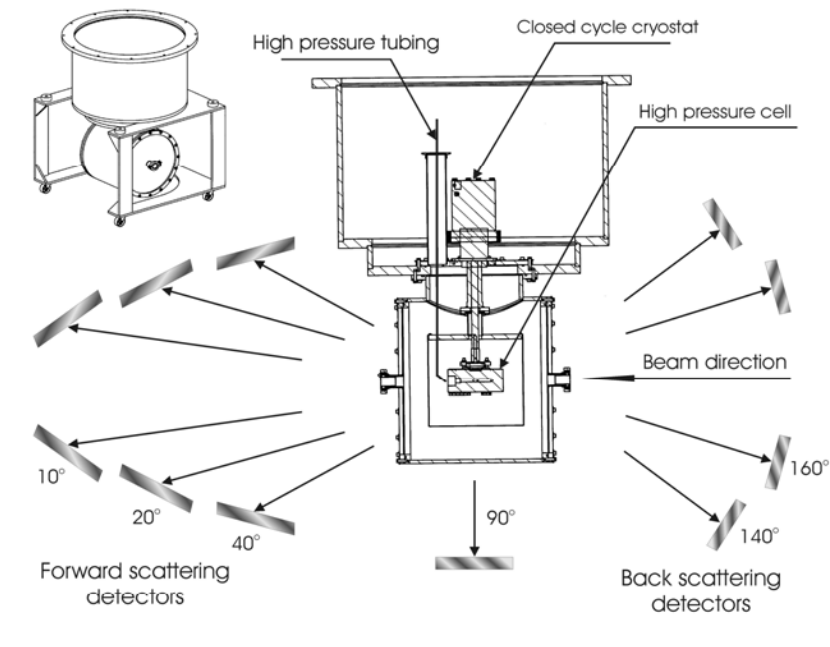


Figure A-13. Schematic general view (in the top-left corner) and the enlarged sectional view of the experimental setup designed for *in situ* high- P low- T neutron diffraction at LANSCE (Lokshin & Zhao, 2005).

Experimental Techniques

We developed a high- P low- T fluid/gas cell to perform *in-situ* and *real-time* neutron diffraction and inelastic neutron scattering at LANSCE's HIPPO and FDS beamlines, respectively (Figure A-13) (Lokshin & Zhao, 2005). The pressure cell was constructed of Al-7075 alloy since aluminum has a small cross section for neutron scattering and it maintains reasonably high strength under hydrogen pressures. This cell is powered with a gas/fluid pressure intensifier and a double-stage displacer cryostat reaching liquid He temperature. It can hold pressures up to 700 MPa and maintain temperatures down to 20 K

on samples as large as 5 cm³. HIPPO covers a wide range of Q (scattering vector, 0.13-52.4 Å⁻¹) values, and its multiple detectors are configured to provide high counting rates at different diffraction angles. FDS measures vibrational spectra in the wavenumber range 40-4000 cm⁻¹ with a resolution of 3-5% (using maximum entropy methods for data analysis) and offers several advantages over optical methods (infrared, Raman) such as greater sensitivity to hydrogen and no selection rules. These setups are thus ideal for *in-situ* realtime studies of formation/decomposition of hydrogen inclusion compounds as time evolves at various pressure and temperature conditions.

Appendix C
INELASTIC NEUTRON SCATTERING STUDY OF HYDROGEN IN D₈-THF/D₂O
ICE CLATHRATE

Kimberly T. Tait^{1,3}, Frans Trouw¹, and Yusheng Zhao¹, Craig M. Brown² & Robert T.
Downs³

1. Manuel Lujan Jr. Neutron Center, Los Alamos National Laboratory, Los Alamos, NM
87545
2. Indiana University Cyclotron Facility, Indiana University, 2401 Milo B. Sampson Lane,
Bloomington, IN 47408 and National Institute of Standards and Technology, Gaithersburg,
MD 20899
3. Department of Geosciences, University of Arizona, Tucson, AZ 85721

Submitted to the *Journal of Chemical Physics*

February 2007

Abstract

In situ neutron inelastic scattering experiments on hydrogen adsorbed into a fully deuterated tetrahydrofuran water ice clathrate show that the adsorbed hydrogen has three rotational excitations (transitions between $J = 0$ and 1 states) at approximately 14 meV in both energy gain and loss. These transitions could be unequivocally assigned the expected slow conversion from ortho- to para-hydrogen resulted in a neutron energy gain signal at 14 meV, at a temperature of 5 K ($kT = 0.48$ meV). A doublet in neutron energy loss at approximately 28.5 meV are interpreted as $J = 1 \rightarrow 2$ transitions.

In addition to the transitions between rotational states, there are a series of peaks that arise from transitions between center-of-mass translational quantum states of the confined hydrogen molecule. A band at approximately 9 meV can be unequivocally interpreted as a transition between translational states, while broad features at 20 meV, 25 meV, 35 meV and from 50 meV to 60 meV are also interpreted in terms of the translational quantum states.

A detailed comparison is made with a recent 5D quantum treatment of hydrogen in the smaller dodecahedral cage in the structure-II ice-clathrate structure. Although there is broad agreement regarding the features, such as the splitting of the $J = 1$ degeneracy, the magnitude of the external potential is overestimated. The numerous transitions between translational states predicted by this model are in poor agreement with the experimental data.

Comparisons are also made with three simple exactly solved models, namely a particle in a box, a particle in a sphere, and a particle on the surface of a sphere. Again, there are too many predicted features from the first two models, but there is reasonable agreement

with the particle on a sphere model. This is consistent with published quantum chemistry results for hydrogen in the dodecahedral 5^{12} cage, where the center of the cage is found to be energetically unfavorable, resulting in a shell-like confinement for the hydrogen molecule wave function. These results demonstrate that translational quantum effects are very significant, and a classical treatment of the hydrogen molecule dynamics is inappropriate under such conditions.

Introduction

Understanding the mechanism of hydrogen adsorption in novel materials is of considerable interest from the perspective of hydrogen storage for a future hydrogen fuel economy. The discovery of hydrogen-water ice clathrate (Mao et al., 2002) demonstrated that at high pressures (200 MPa) hydrogen can act as a templating agent for clathrate formation. A subsequent study (Florusse et al., 2004) showed that a ternary clathrate could be formed between hydrogen, tetrahydrofuran (THF), and water at a much reduced hydrogen gas pressure. This reduction in pressure is attractive from an engineering perspective for hydrogen storage applications.

There has been some ambiguity regarding the location and quantity of hydrogen adsorbed in THF-clathrate. The large cages are all filled by the THF, and so the hydrogen is expected to reside in the smaller dodecahedral (5^{12}) cavity. Mao et al. (2002) indicates that there is a double occupancy of the small cage in the pure hydrogen clathrate though this conclusion has been the subject of some controversy, and a recent study reported by Hester et

al.(2006) concludes that there is only single occupancy of the small cage in THF-ice clathrate.

Neutron spectroscopy has been extensively used to characterize the dynamics of hydrogen adsorbed in a wide variety of materials, such as alkali metal graphite intercalation compounds (Smith et al., 1996) and zeolites (Tam et al., 2004) and in the octahedral interstitial sites in solid C_{60} (FitzGerald et al., 1999).

At low temperatures, it is straightforward to measure the quantum rotor states and center-of-mass modes of the hydrogen molecule, while quasi-elastic scattering occurs when there is diffusive rotational or translational motion. Hydrogen has a relatively large neutron scattering cross section, and the relative contribution from the hydrogen can be further enhanced by deuterating other components.

This study is an inelastic neutron scattering study of the dynamics of hydrogen in the ternary clathrate formed between water, THF, and hydrogen. The ternary clathrate was formed *in situ* by adsorbing hydrogen in THF-ice clathrate close to melting point. The results show that the quantum rotor motions are only perturbed to a small extent upon adsorption, while the translational quantum states are significantly perturbed by confinement in the clathrate cage.

Methods

Neutron inelastic scattering measurements were made on the Pharos spectrometer located at the Lujan Center, Los Alamos National Laboratory and on the (DCS) instrument at the National Institute of Standards, National Center for Neutron Research (NCNR, NIST).

These are complementary instruments as Pharos is designed for thermal neutron experiments using incident energies, while DCS uses cold neutrons (e.g. 3 meV) to attain a much better elastic energy resolution. The Pharos experiment therefore focused on relatively large neutron energy loss scattering, while the DCS was used to look for low energy excitations on the order of 1 meV and for evidence of quasi-elastic neutron scattering.

Pharos: The Pharos spectrometer is on a pulsed neutron source, viewing a room temperature water moderator. Per-deuterated THF (99.95% D, Aldrich) and D₂O (99.9% D, Aldrich) were mixed in the mole ratio 1:17 and frozen to form a fully deuterated THF-ice clathrate. This was crushed using a mortar and pestle in a helium atmosphere, and then transferred to the aluminum scattering container. All of the equipment and the clathrate were kept cold using dry ice.

The aluminum sample container is a pressure vessel with 8 parallel cylindrical channels 5mm in diameter cut into a flat piece of aluminum, with some of the excess aluminum removed between the channels. The channels are connected via a common channel formed between the lid and the body of the cell. The lid has a connection to a capillary gas line for the application of gas pressure to the sample.

After filling, the cell was quickly mounted on the tip of a helium closed-cycle refrigerator at approximately 250 K. This was then placed in the sample chamber and the chamber evacuated to at least 10^{-3} Pa. The sample container was then warmed to 265 K in order to remove any residual ice on the external surface of the sample container.

Hydrogen at a pressure of approximately 14 MPa was then applied to the THF-ice clathrate at 270K. The sample was subsequently valved off from the hydrogen source and the pressure monitored to see if the pressure dropped due to incorporation of the hydrogen into the clathrate. This drop in pressure was observed, but there was clearly also a small leak into the sample chamber and so the pressure drop data is ambiguous. The valve to the hydrogen bottle was periodically opened to maintain a hydrogen pressure greater than 10 MPa.

After several hours, the sample was cooled to 100 K while maintaining the hydrogen pressure at 14 MPa, and then the excess gaseous hydrogen was pumped off assuming that all of the hydrogen in the clathrate was trapped at that temperature. The sample was further cooled to 8 K and the inelastic scattering was measured using incident energies of 70 meV, 40 meV, 25 meV, and 15 meV. Measurements were also carried out at temperatures of 50 and 100 K at a variety of incident energies ranging from 40 meV to 120 meV.

DCS: Preparation of a d-THF-D₂ sample was carried out in a similar manner and this was loaded into a cylindrical aluminum sample cell with a wall thickness of 12.7 mm and a sample bore of 10 mm. The sample cell was put into a standard helium top-loading ILL cryostat and the scattering from the THF clathrate was measured at 5 K, 50 K, 100 K, 150 K and 200 K.

Hydrogen was then added in a similar manner to the Pharos experiment, and the excess gas pumped off at 100 K. Scattering measurements were then made at sample

temperatures of 5, 50 K, 100 K and 150 K. An incident wavelength of 5.5 Å was used, yielding an elastic energy resolution of 90 meV full-width at half-maximum.

Results

The experiments on the Pharos and DCS spectrometers yielded very similar results, which demonstrated the reproducibility of the sample preparation. Even with a monochromatic incident neutron beam, it was possible to measure a useful *in situ* diffraction pattern from the samples since both instruments have detectors covering a wide range of 2θ . An example of the diffraction patterns measured on DCS is shown in Figure A-14.

The diffraction pattern shows strong peaks from the clathrate, in addition to the characteristic triplet from water ice in the range 3.4 Å to 4 Å. Although some ice is present, it is a minor component of the sample and in any case not important from the perspective of this experiment, as it will not absorb any hydrogen at 14 MPa.

The diffraction pattern from the ternary clathrate is expected to be very similar. Inspection of the neutron diffraction pattern for the fully filled D₂/d₈-THF/D₂O clathrate published by Hester et al. (2006), shows that the most visually resolved difference upon deuterium adsorption is the change in intensities in the two peaks around 2.75 Å. These cannot be seen in the diffraction pattern in Figure A-14, as the d-spacing cutoff for DCS operated with a wavelength of 5.5 Å is just above that at about 2.9 Å. It was also not possible to resolve this feature in the Pharos data since the instrument has poor resolution when operated in constant wavelength mode. Nevertheless, the diffraction patterns before and after hydrogen adsorption are very consistent with an unchanged residual fraction of ice.

Figure A-15 shows a comparison between the inelastic scattering spectrum for the THF-clathrate before and after the addition of the hydrogen as measured on Pharos. There is extra scattering from the hydrogen on both the neutron energy gain and loss side as is expected with a mix of para- and ortho-hydrogen. The two spectra were scaled by the integrated number of protons on the spallation target which is proportional to the total number of incident neutrons for each measurement.

A detailed analysis of the scattering from the hydrogen (THF-clathrate scattering has been subtracted) are shown in Figures A-16 and A-17. On the neutron energy gain side, a model incorporating three Gaussians and a sloping background was fitted to the extra scattering, while a total of 7 Gaussians and a sloping background was fitted to the neutron energy loss data.

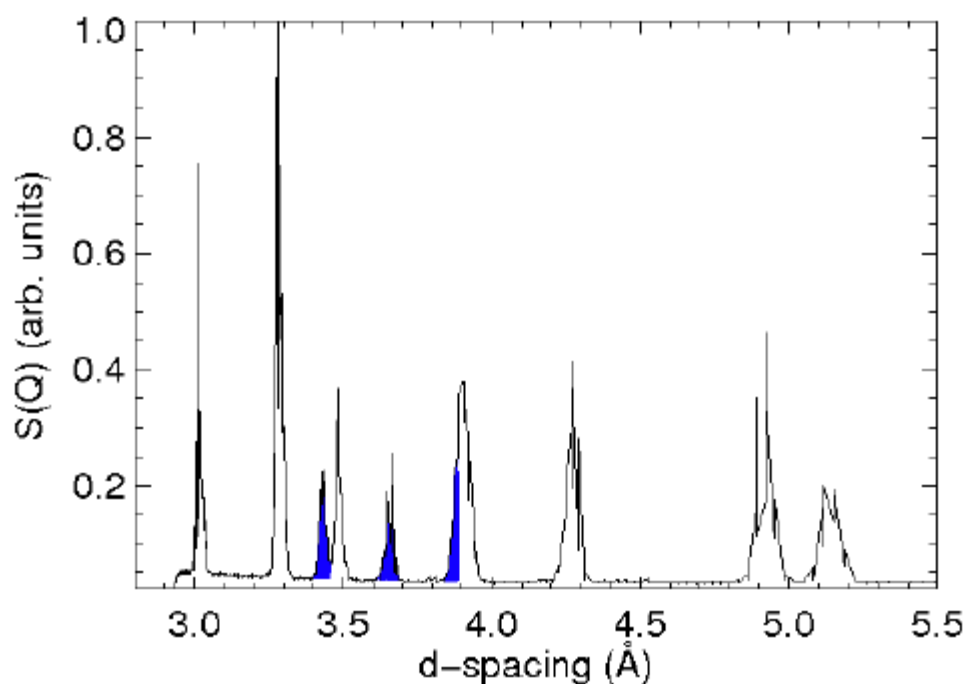


Figure A-14: Diffraction pattern from ternary clathrate $\text{H}_2/\text{d}_8\text{-THF}/\text{D}_2\text{O}$ at 5 K measured on DCS with an incident wavelength of 5.5 Å. The three shaded peaks are from residual ice in the sample.

Similar results were obtained on the DCS spectrometer, though this instrument is primarily designed to operate with cold neutrons and so the neutron energy loss range is typically reduced to a few meV. The neutron energy gain spectra for the ternary clathrate at 5 K and 50 K are shown in Figure A-15. There is shift in intensity to a higher energy transfer shoulder at 50 K, which is consistent with an increased population of a higher energy state.

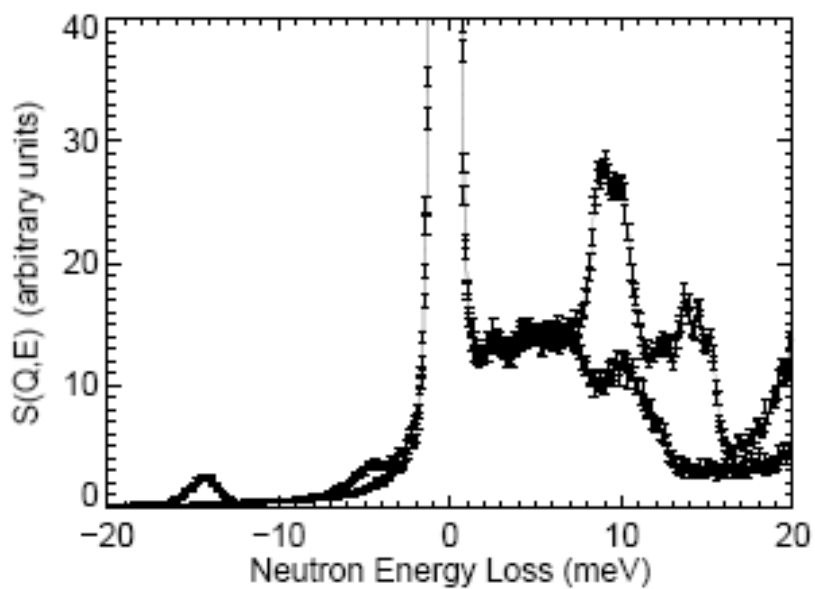


Figure A-15: Inelastic scattering spectrum from THF-ice clathrate before and after the addition of hydrogen measured at 8 K.

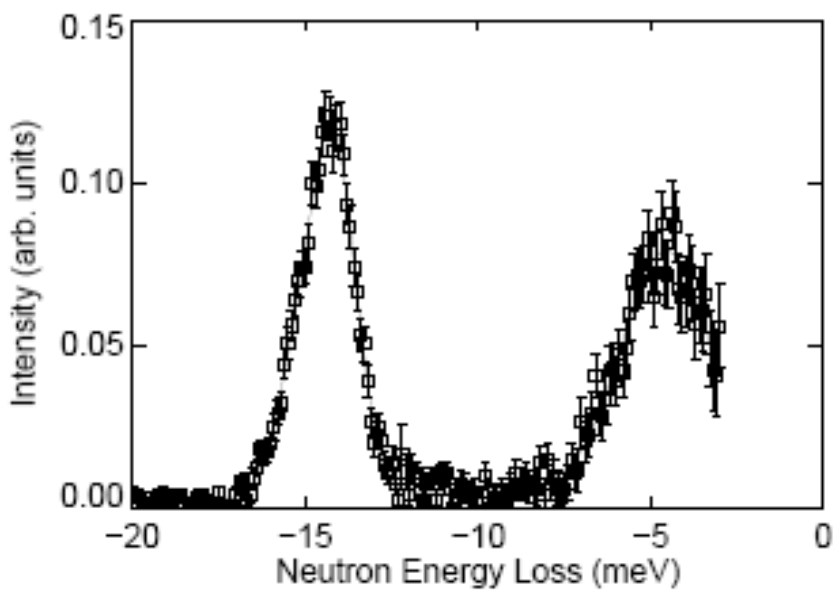


Figure A-16: Model fit using multiple Gaussians and a sloping background for the neutron energy gain data measured on Pharos at 8 K.

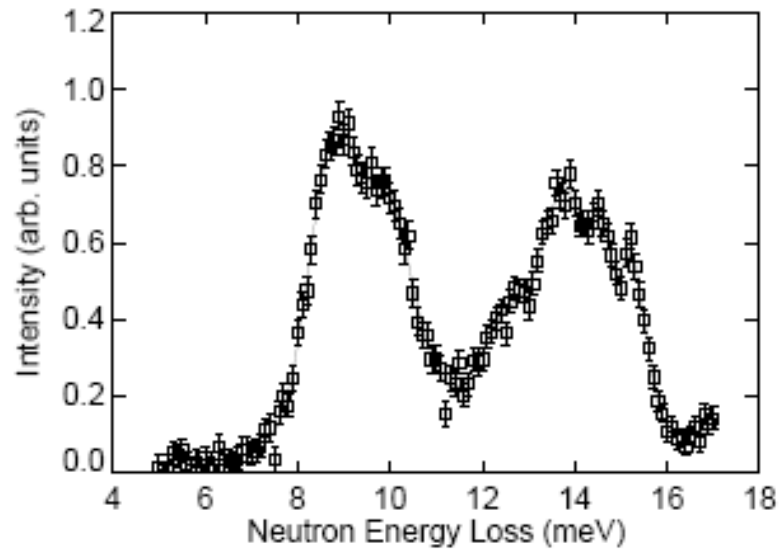


Figure A-17: Model fit using multiple Gaussians and a sloping background for the neutron energy loss data measured on Pharos at 8 K.

	Position (meV)	Intensity (arb. units)	FWHM (meV)
Neutron Energy Gain	-15.33	0.030	0.62
$\chi^2 = 0.74$	-14.19	0.108	0.65
	-4.58	0.071	1.26
Neutron Energy Loss	8.71	0.47	0.47
$\chi^2 = 0.84$	9.58	0.54	0.96
	10.04	0.17	0.38
	12.58	0.33	0.65
	13.84	0.61	0.49
	14.57	0.34	0.21
	15.22	0.46	0.31

Table A-1: Results from fitting the H₂ scattering data measured at 8 K.

A good fit of these spectra is obtained using two Gaussians at 5 K and three Gaussians at 50 K (both fits include a sloping linear background). The positions of the Gaussians at 5 K are -15.15 meV and -13.96 meV, while at 50 K the centers are at -15.10 meV, -13.93 meV and -10.32 meV (last peak compensates for increased scattering at lower energies at 50 K). The 15.1 meV peak is consistent with the neutron energy loss results, and the 13.9 meV peak is likely an unresolved combination of the three neutron energy loss peaks at 14.5 meV, 13.7 meV, and 12.8 meV. There are additional higher energy features in the spectra from the ternary clathrate at 8 K on Pharos, which are not present in the THF-ice clathrate spectrum (Figure A-16). There are two sharp peaks next to each other at approximately 28 meV, and some broader features at 20 meV, 23 meV, and 36 meV. The two sharper peaks show quite different Q-dependence, with the higher energy excitation peaking in intensity before the lower energy peak.

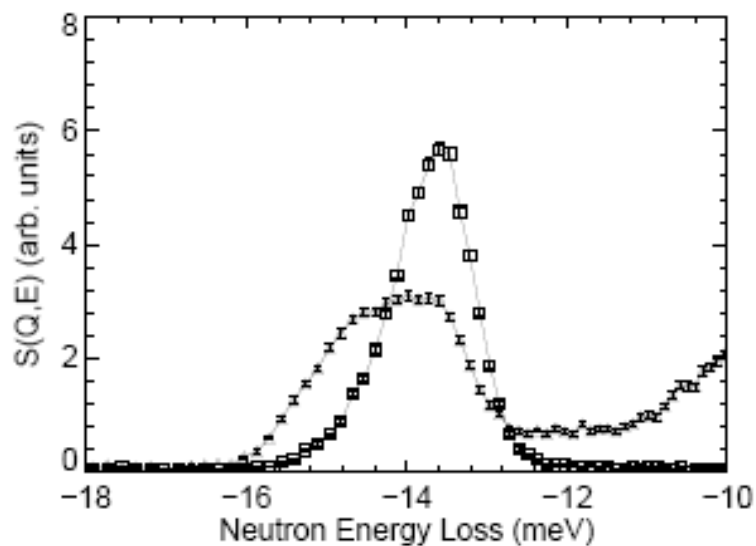


Figure A-18: Neutron energy gain peaks observed on DCS at 5 K (squares) and 50 K (triangles).

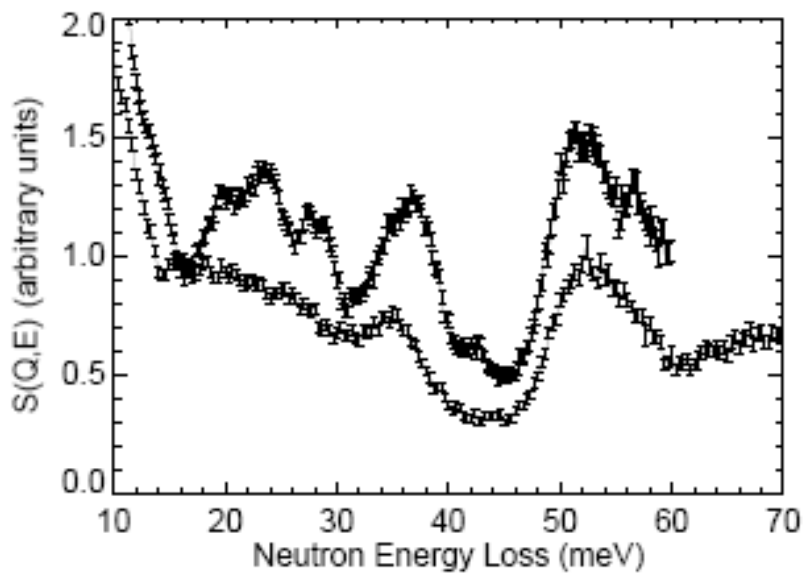


Figure A-19: Upper trace is $H_2/d\text{-THF}/D_2O$ measured at 8 K using an incident energy of 70 meV on Pharos. Lower curve is the equivalent spectrum measured for TDF/D_2O at 8 K using an incident energy of 120 meV. Both curves are a sum of $S(Q,E)$ for $Q=1-5 \text{ \AA}^{-1}$.

Discussion

A. Rotational Quantum States

It is not possible to assign four peaks to transitions between the $J = 0$ and $J = 1$ quantum states, as the $J = 1$ state has a degeneracy ($2J + 1$) of 3, and the ground state is singly degenerate. The options to rationalize this are: (1) distinct types of hydrogen molecular adsorption sites; (2) transitions from the $J = 1$ to a state approximately 12 meV higher in energy; or (3) one of the peaks fitted to the neutron energy loss spectrum is not a rotational transition. Option (2) is very unlikely in view of the small splitting of the $J = 1$ state (0.6 - 1 meV), indicative of a small hindering potential and correspondingly small perturbation of the $J = 2$ state which is at 44.1 meV (i.e. gap of 29.4 meV) for an unperturbed hydrogen molecule.

Assignment of the four peaks to states for two adsorption sites is challenging. Fortunately the temperature dependence is helpful in this respect. At 5 K, kT is approximately 0.5 meV and this increases to approximately 5 meV at 50 K. As the 15.1 meV is only marginally populated at 5 K, the separation between the states must be closer to 2.5-3 times 0.5 meV. This argues for a combination of the 12.8 meV and 15.1 meV states to be two of the split $J = 1$ states for one site. This would make the 12.8 meV state the favored one at 5 K. However there is little intensity at 12.8 meV in the spectrum taken at 5 K (Figure A-17). This argues in favor of a 13.7 meV lowest energy state derived from the free molecule $J = 1$ state (option 3).

This implies that there is a single hydrogen adsorption site with a split $J = 1$ triplet at

13.7 meV, 14.5 meV, and 15.1 meV. This is also consistent with the higher energy centroid for the neutron energy gain peak at 8 K measured on Pharos as compared to the DCS data taken at 5 K. A consequence of this assignment is that there should be excitations in neutron energy gain at 1.7 meV and 2.3 meV. Careful examination suggests that there may be extra intensity in that region of the spectrum, but there is significant intensity from the host clathrate modes in that region and the intensity of these features is expected to be weak since they originate from ortho-hydrogen.

Unfortunately, it is not possible to determine which of these excitations represent transitions between rotational states as there is no equivalent feature expected to be present in neutron energy gain (i.e. all the molecules will be in the lowest lying $J = 1$ or $J = 0$ states at 8 K).

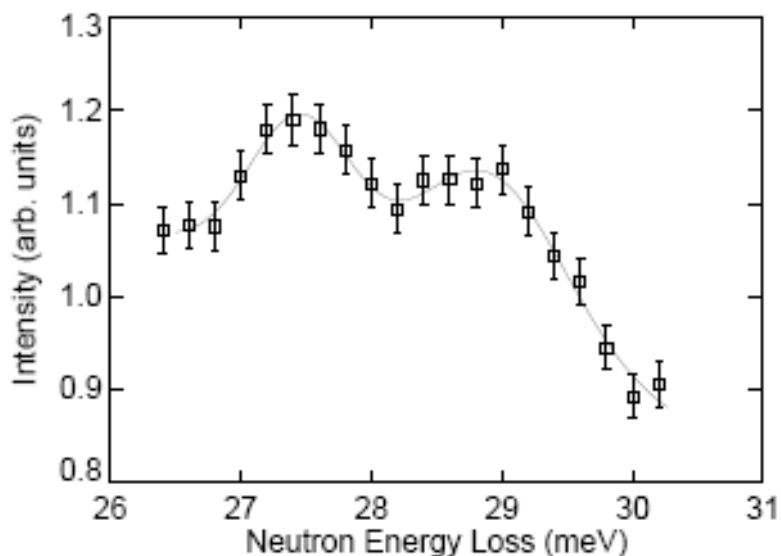


Figure A-20: Two Gaussian plus sloping background fit of the Pharos data measured at 8 K with 70 meV incident neutrons.

For the free hydrogen molecular rotor, the $J = 2$ state is expected to lie 42.81 meV (6B) above the energy of the $J = 0$ ground state. As the external potential is weak (small perturbation of the $J = 1$ states) it is tempting to assign the broad feature at approximately 37 meV to some of the $J = 2$ states (5-fold degeneracy in the free molecule). This would imply that the other features arise from translational quantum states of the confined molecule. It should also be noted that the hydrogen molecule can “ride” along with any collective excitation in the THF-ice lattice and thereby enhance the intensity of existing features present in the binary clathrate.

At the higher energies, there is considerable scattering in neutron energy loss between 20 meV and 60 meV. As can be seen from Table A-2, there are many translational states in the energy range considered in the theory paper (up to 28 meV). The interpretation of these features is therefore that they represent many transitions to excited translational states of both ortho- and para-hydrogen, in addition to a weakly split series of $J = 0 \rightarrow 2$ transitions in the vicinity of 43 meV [expected to be weak (Young and Koppel, 1964)] and $J = 1 \rightarrow 2$ around 28.5 meV. Indeed, there are two relatively sharp peaks at 27.47 and 28.9 meV (Figure A-20), and this doublet is therefore assigned to the $J = 1 \rightarrow 2$ transitions. As expected, there is a feature in the vicinity of 42 meV which is interpreted as the weak $J = 0 \rightarrow 2$ transition.

B. Analysis of translational quantum states

Neutron diffraction has shown that a single hydrogen molecule resides in the smaller 5^{12} cage in the THF-ice clathrate (Hester et al., 2006). There are two consequences of this confinement, the effect of an anisotropic external potential on the rotational quantum states and the imposition of constraints on the translational periodicity of the molecular wave function. From the analysis of the scattering data, the rotational modes are not greatly perturbed by the external potential. However, confinement on the scale of a few angstroms has dramatic consequences for the translational quantum states. This effect is explored using two simple solutions to the Schrödinger equation, namely particle in a box and particle in a sphere, and also by comparison with a recently published quantum calculation for hydrogen in the specific environment of the 5^{12} cage in an ice clathrate.

1. Computational five-dimensional quantum theory

A recently published 5D quantum theoretical treatment of hydrogen in the dodecahedral cage of SII ice clathrate (Xu et al., 2006) provides detailed predictions for the rotational and translational quantum states of the hydrogen molecule. These are summarized in Table A-2, ordered by the energy relative to the lowest $J = 0$ ground state (the study confirms that J is still a good quantum number).

These theoretical results are compared with the experimental results in Figure A-21, again assuming equal intensity for all of the transitions. The comparison is limited to a range up to approximately 28 meV. The band at 9 meV is reproduced, although the predicted

transition at 6.4 meV is not observed. Another discrepancy is the larger than observed splitting of the $J = 1$ rotational quantum state, where theory predicts transitions at 11.22 meV, 14.5 meV, and 18.67 meV while the interpretation of the experiment discussed above indicates that the transition are at 13.5 meV, 14.5 meV, and 15.1 meV.

As the ortho-hydrogen ground state is not observed below 13.5 meV, the assignment of the first two transitions on the basis of a comparison between the energy loss and gain data is solid. However, the assignment of the 15.1 meV transition as the $(1,1)_u$ state is not as certain, and it could arise from a transition to a translational quantum state. However, based on the 13.7-14.5 meV gap, we would expect the $(1,1)_u$ state to be roughly the same gap to the higher side of the 14.5 meV transition (i.e. 15.3 meV) as is the case in the theory result (-3.28 and +4.17 meV). The original assignment of the triplet about 14.5 to a split $J = 1$ state is sound based on these arguments, and the predicted splitting is much larger than found experimentally, although they are both small on the scale of the rotational constant B .

Energy (meV)	O/P	State	J=1 \rightarrow 0 (meV)
0	P	(0,0,0)	11.22
6.44	P	(1,0,0)	4.78
8.21	P	(0,1,0)	3.01
9.56	P	(0,0,1)	1.66
11.22	O	(0,0,0) (1,0)	
14.53	O	(0,0,0) (1,1) _l	
15.31	P	(2,0,0)	
16.1	P	(1,1,0)	
17.35	P	(1,0,1)	
17.55	O	(1,0,0) (1,0)	
18.44	P	(0,2,0)	
18.67	O	(0,0,0) (1,1) _u	
19.3	O	(0,1,1) (1,0)	
19.55	P	(0,1,1)	
20.76	O	(1,0,0) (1,1) _l	
21.33	O	(0,0,1) (1,0)	
21.78	P	(0,0,2)	
23.09	O	(0,1,0) (1,1) _l	
24.25	O	(0,0,1) (1,1) _l	
25.1	O	(1,0,0) (1,1) _u	
25.29	P	(2,1,0)	
26.38	O	(2,0,0) (1,0)	
26.95	O	(0,1,0) (1,1) _u	
27.45	O	(1,1,0) (1,0)	
28.30	O	(0,0,1) (1,1) _u	

Table A-2: Energies of the translational quantum states of ortho- and para-hydrogen predicted by (Xu et al., 2006), and the predicted neutron energy gain transitions from the ortho-hydrogen translational ground state.

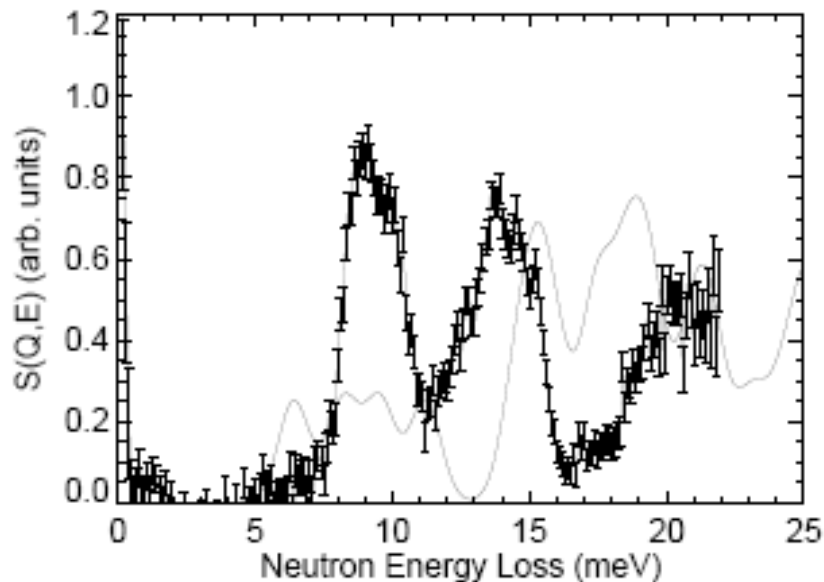


Figure A-21: Comparison between the prediction from the 5D quantum theoretical model (line) and the data measured on Pharos at 8 K.

Assignment of the two features at 8.77 meV and 10.01 meV is consistent with the expected gap between the $J = 0$ (0,0,0) ground state and the excited (0,1,0) and (0,0,1) translational states (8.21 meV and 9.56 meV). However, there is no evidence for a separate (1,0,0) state around 6 meV. It is possible that the calculation overestimated the anisotropy of the translational states and this is consistent with the uneven intensity distribution in these two peaks. It is quite likely that the transition to the third translational state is not resolved from the other two transitions.

On the neutron energy gain side, the broad distribution centered about 5 meV has not been discussed. It cannot arise from a rotational tunneling transition, as it is not present in

neutron energy gain, and the sample temperature of 8 K requires that it be associated with an excited state that cannot transition to the ground state. This then requires that the transition be associated with the $J = 1$ states, and they represent a transitions from ortho-hydrogen to the excited translational ground states of para hydrogen. The gap between the para-hydrogen excited translational states (8.77 meV and 10.1 meV) and the $J = 1$ states populated at 8 K (mainly 13.7 meV and 14.5 meV) is approximately 4.6 meV.

Although the sophisticated computational approach is attractive, it is not straightforward to determine why there is significant disagreement between experiment and theory. The next sections will discuss the application of three very simple models for the translational quantum states of the confined hydrogen molecules. Although simple, they provide semi-quantitative insight into the interaction between the clathrate framework and the adsorbed hydrogen.

2. Particle in a box

The simplest approach to understanding the translational quantum states is to consider the hydrogen to be in a cage that approximates to a three-dimensional rectangular box with infinitely high confinement potential. This is not expected to be quite correct, as there are openings in the cage and the shape is a crude approximation. The solution to the Schrödinger equation is (Atkins, 1970):

$$E_{n_1, n_2, n_3} = \frac{h^2}{8m} \left(\left(\frac{n_1}{L_1} \right)^2 + \left(\frac{n_2}{L_2} \right)^2 + \left(\frac{n_3}{L_3} \right)^2 \right), n_i = 1, 2, 3 \dots$$

where $L_{1,2,3}$ are the lengths of the sides, and m is the mass of the hydrogen molecule.

From the preliminary analysis we know that the peak at approximately 9 meV is associated with the center-of-mass motion of the hydrogen. This peak contains at least two features, centered at 8.7 meV and 9.6 meV. The relative areas of the two Gaussians fitted to this feature are similar, with the latter approximately twice the width of the former. This suggests that there are really three features in this band, corresponding to different values for L_i . A reasonable reproduction of this feature using the particle in a box equation for the separation between the ground state ($n_{i,j,k} = 1$) and the first excited states ($n_{i,j} = 1, n_k = 2$), using lengths of 1.75 Å, 1.85 Å, and 1.95 Å.

A qualitative comparison between this model and the measured spectrum is shown in Figure A-22, where the expected transitions are plotted as a series of Gaussian peaks together with the experimental data. Although it is possible to reproduce an excitation at approximately 9 meV using reasonable lengths for the size of the box, there are many predicted transitions at higher energies that are not present in the data. Some of these transitions could be shifted by rotation-translation coupling, but the sophisticated computational study described in Section 1 (Xu et al., 2006) predicts that this effect is on the order of a few percent.

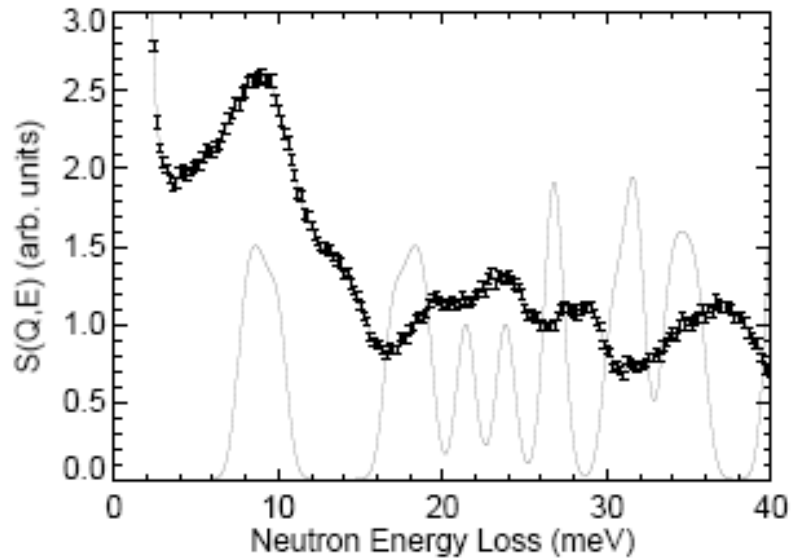


Figure A-22: Comparison between prediction of particle in a box model (line) and the experimental data measured at 8 K on Pharos.

3. Particle in a sphere

A spherical shape of the cavity is likely to be a much better approximation to the 5^{12} cavity. The solution to the Schrödinger equation for this model is (Griffiths, 1995):

$$E_l = \frac{u_{l,k}^2 \hbar^2}{2mr^2}$$

where k represents the series of points where the spherical Bessel functions of order l cross zero, m is the mass of the hydrogen molecule, and r is the radius of the sphere.

Two states are close in energy, and the radius of the cavity is chosen so that the energy gap between them approximately matches the location of the excitations centered about 9 meV. A comparison between this model and the experimental spectrum is shown in Figure A-23. There is no better agreement than is the case for the particle in the box model.

There are still too many predicted transitions, e.g. no peaks at 3.1 and 6.4 meV in the experimental data, and no sign of the predicted peak at approximately 15.6 meV.

4. Particle on the surface of a sphere

The implicit assumption in both of the above analytical models is that there is no potential within the dodecahedral cage that favors particular regions of the available space. This is unlikely to be the case, and *ab initio* calculations by (Patchkovskii and Tse, 2003) at the MP2 level predict a potential well approximately 1.1 Å from the center of the cage. As the potential difference between the center and this well is relatively large at 50 meV, the hydrogen molecular wave-function will be localized by this barrier.

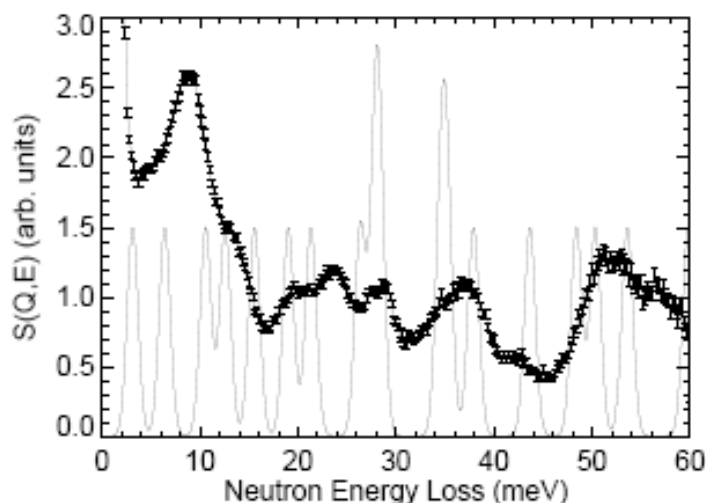


Figure A-23: Comparison between prediction for particle in a sphere of radius 1.8 Å (line) and the data taken on Pharos at 8 K.

This effect can be roughly approximated using the analytical solution for a particle constrained to be on the surface of a sphere. The energy levels for this model are given by (Atkins, 1970):

$$E_l = \frac{l(l+1)\hbar^2}{2mr^2}, l = 0, 1, 2, \dots$$

where m is the mass of the hydrogen molecule and r is the radius of the sphere. A comparison between the data from Pharos and this model is shown in Figure A-24. As there are at least two peaks at approximately 9 meV, the figure shows two series of peaks for sphere radii of 1.05 Å and 1.1 Å. The origin of the splitting is likely due to removal of the degeneracy of the states as the cavity is not exactly spherical.

There is reasonably good agreement, particularly as there are far fewer excitations predicted than is the case for the other models. All of the peaks are accounted for as the bands at 14 meV, 28 meV, and 42 meV arise from transitions between rotational quantum states. There is a predicted transition at approximately 3.5 meV, but this could be obscured by the significant scattering from the THF-ice clathrate at those lower energies.

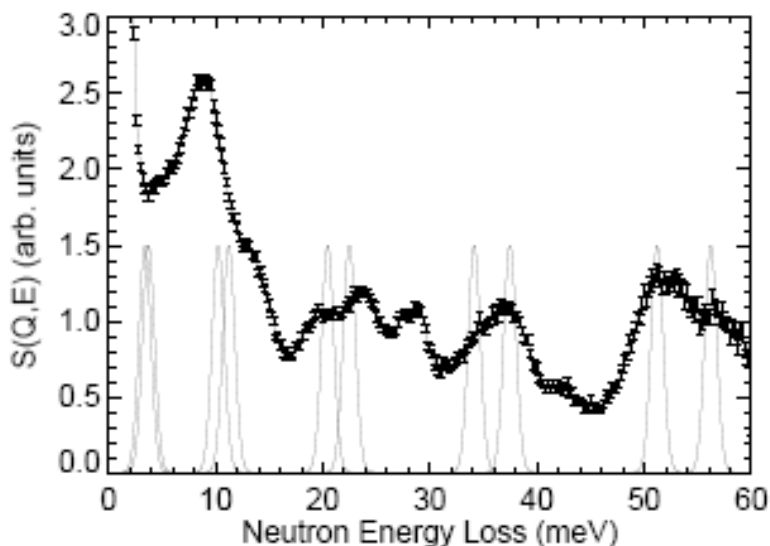


Figure A-24: Comparison between the excitations expected for particle on the surface of a sphere with radii 1.05 and 1.1 Å, and the data taken on Pharos at 8 K.

5. Summary of comparisons for translational quantum states

It is clear from the discussion that neither simple models nor sophisticated computational quantum theory correctly predicts all of the translational quantum transitions for hydrogen in the 5^{12} cage of THF-ice clathrate. The 5D theory, particle in a box, and particle in a sphere model all predict many more transitions than are observed. Confinement of the hydrogen onto the surface of a sphere gives more promising results, with the assumption that the apparent peak splittings arise from a splitting of degenerate states.

C. Temperature dependence

As the temperature of the sample is increased from 8 K, there will be temperatures at which the THF and hydrogen molecules will exhibit diffusive motion on the length and time

scales of the neutron experiments. As the DCS instrument was operated with a moderately high elastic energy resolution of approximately 90 meV (full-width at half-maximum), this diffusive motion would have to occur on the picosecond time-scale. It is expected that the onset of diffusive motion will occur at different characteristic temperatures for the THF and the hydrogen.

From the measurements made on the THF-ice binary clathrate, quasi-elastic scattering is observed at 50 K and above.

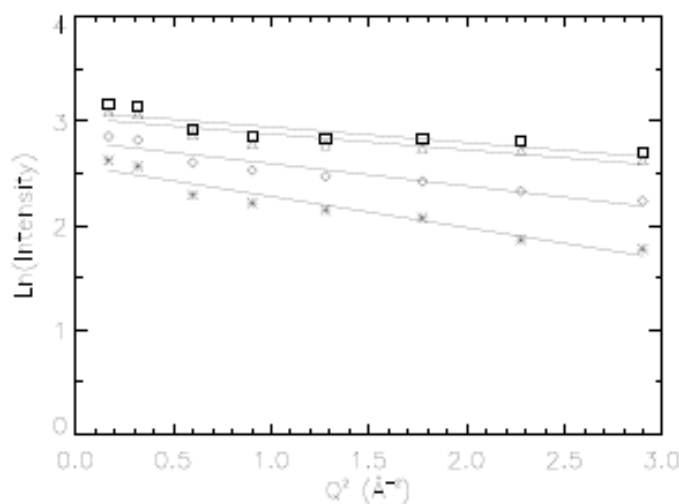


Figure A-25: Debye-Waller plots from the DCS data, with the intensity summed over the neutron energy loss range of ± 1 meV.

As the THF is fully deuterated, this scattering is coherent, and the intensity and width of the scattering is very dependent on the momentum transfer. As the hydrogen is known to occupy the small cage while the THF is in the larger cage, it is likely that the scattering from the THF-ice clathrate will not be significantly affected by the presence of the hydrogen. This is

consistent with the excellent match between the inelastic scattering from the clathrate with and without hydrogen below 7 meV. If this assumption holds, then the THF-ice scattering data can be subtracted from the H₂/THF/D₂O data to obtain the scattering from the hydrogen only.

This subtraction was carried out and the results inspected for any sign of a quasi-elastic broadening over the range 5 K-150 K. There was no evidence of diffusive broadening, or any sign of a shape anomaly in the vicinity of the elastic scattering indicative of a problem arising from the subtraction of the THF/ice background scattering. The conclusion is that the hydrogen molecule does not exhibit any diffusive motion on the length and time scale of the experiment up to a temperature of 150 K. This is consistent with the requirement that the sample be close to the melting point of the clathrate to incorporate the hydrogen into the structure.

The intensity of the elastic scattering from the hydrogen will have a Q-dependence that follows the Debye-Waller factor. The analysis is subject to interference from Bragg scattering from the clathrate, and the DCS data was analyzed with all detectors showing Bragg scattering removed. The signal integrated between -1 and 1 meV as a function of momentum transfer are plotted in Debye-Waller form in Figure A-25, including linear fits to extract the mean square displacements ($\langle u^2 \rangle$). Increasing the temperature should increase $\langle u^2 \rangle$, and the onset of a transition is often signaled by a rapid increase in $\langle u^2 \rangle$. There is a slow increase above 50 K, which is consistent with the lack of any quasi-elastic scattering.

However, the zero momentum transfer intercept should remain constant as a function of temperature, and this is not the case as is also shown in Figure A-26. This suggests that there may be some coupling between the motion of the hydrogen and the THF molecules, resulting in this unexpected drop in the zero-Q intercept.

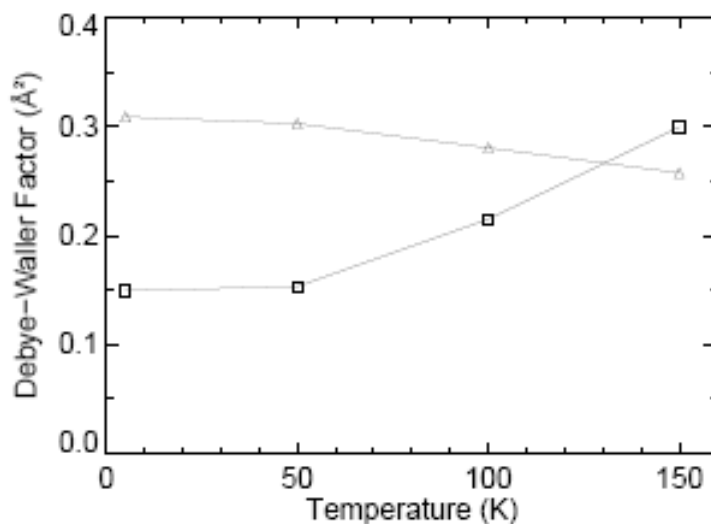


Figure A-26: Temperature dependence of the hydrogen molecule Debye-Waller Factor (squares). Also shown is the variation in the zero-Q intercept of the fits in Figure A-25 (triangles, arbitrary units).

Conclusion

Hydrogen was successfully loaded into a deuterated THF-water ice clathrate and measured on the Pharos and DCS inelastic neutron scattering spectrometers with similar results. The rotational quantum states are mildly perturbed from their free molecule energies demonstrating that the potential experienced by the hydrogen adsorbed in the dodecahedral 5^{12} cage is weakly anisotropic. A series of transitions between translational quantum states are also observed.

A computational quantum chemical study of hydrogen in the 5^{12} cage of structure-II ice clathrate (Xu et al., 2006) predicts a larger shift in the rotational transitions, and many more transitions between translational states than is observed. Comparisons between three simple exact solutions to the Schrödinger equation suggests that the most appropriate model confines the hydrogen molecule into a spherical shell approximately $1.05 \text{ \AA} - 1.1 \text{ \AA}$ from the cage center. This result is in good agreement with quantum chemical calculations for the hydrogen translational potential in this cage (Patchkovskii and Tse, 2003). The observed bands with more than one peak are interpreted to arise from a lifting of the degeneracy as the shell is not exactly spheroidal.

No quasi-elastic scattering is observed for the hydrogen up to a temperature of 150 K. However, there is a distinct increase in the Debye-Waller factor between 100 K and 150 K, indicative of the onset of motion with an increased amplitude.

Acknowledgments

This work has benefited from the use of the Lujan Neutron Scattering Center at LANSCE, which is funded by the Department of Energy's Office of Basic Energy Sciences. Los Alamos National Laboratory is operated by Los Alamos National Security LLC under DOE Contract DE-AC52-06NA25396. This work utilized facilities supported in part by the National Science Foundation under Agreement No. DMR-0454672.

REFERENCES

- Andersson, P., and Ross, R.G. (1983) Effect of guest molecule size on the thermal conductivity and heat capacity of clathrate hydrates. *Journal of Physics C. Solid state physics*, 16(8), 1423-32.
- Atkins, P.W. (1970) *Molecular Quantum Mechanics*. Clarendon Press, Oxford.
- Ballard, A.L., and Sloan, E.D. (2000) Optimizing thermodynamic parameters to match methane and ethane structural transition in natural gas hydrate equilibria. *Annals of the New York Academy of Sciences*, 912, 702-712.
- Benamotz, D., and Herschbach, D.R. (1993) Hard fluid model for solvent-induced shifts in molecular vibrational frequencies. *The Journal of Physical Chemistry*, 97(10), 2295-306.
- Berez, E., and Balla-Achs, M. (1983) *Gas Hydrates*. Elsevier Science Publishing Company, Inc., New York.
- Berry, G.D., and Aceves, S.M. (1998) Onboard storage alternatives for hydrogen vehicles. *Energy & Fuels*, 12(1), 49-55.
- Bertie, J.E., Bates, F.E., and Hendricksen, D.K. (1975) Far infrared-spectra and x-ray powder diffraction patterns of structure I hydrates of cyclopropane and ethylene-oxide at 100 degrees K. *Canadian Journal of Chemistry*, 53(1), 71-75.
- Bertie, J.E., and Jacobs, S.M. (1978) Infrared spectra from 300 to 10 cm⁻¹ of structure II clathrate hydrates at 4.3K. *The Journal of Chemical Physics*, 69(9), 4105-13.
- Blake, D., Allamandola, L., Sandford, S., Hudgins, D., and Freund, F. (1991) Clathrate hydrate formation in amorphous cometary ice analogs invacuo. *Science*, 254(5031), 548-551.
- Buffett, B.A. (2000) Clathrate hydrates. *Annual Review of Earth and Planetary Sciences*, 28, 477-507.
- Circone, S., Stern, L.A., Kirby, S.H., Durham, W.B., Chakoumakos, B.C., Rawn, C.J., Rondinone, A.J., and Ishii, Y. (2003) CO₂ hydrate: Synthesis, composition, structure, dissociation behavior, and a comparison to structure I CH₄ hydrate. *Journal of Physical Chemistry. B, Condensed matter, materials, surfaces, interfaces & biophysical*, 107(23), 5529-5539.

- Coulombeau, C., and Jobic, H. (1988) Neutron inelastic spectroscopy of ethylene oxide and partial reassignment of the vibrational frequencies. *Journal of Molecular Structure*, 176, 213-22.
- Daemen, L.L., Hartl, M.A., and Eckert, J. (2006) Introduction to Neutron Vibrational Spectroscopy. LANSCE Joint Neutron Scattering School in Soft Condensed Matter and Structural Biology, May 18-26, 2006.
- Davidson, D.W.a.R., J.A. (1984) NMR, NQR, and dielectric properties of clathrates. Academic Press, New York.
- Eisenberg, D., and Kauzmann, W. (1969) The structure and properties of water. Clarendon Press, Oxford, 1969.
- FitzGerald, S.A., Yildirim, T., Santodonato, L.J., Neumann, D.A., Copley, J.R.D., Rush, J.J., and Trouw, F. (1999) Quantum dynamics of interstitial H₂ in solid C₆₀. *Physical review. B, Condensed matter*, 60(9), 6439-51.
- Florusse, L.J., Peters, C.J., Schoonman, J., Hester, K.C., Koh, C.A., Dec, S.F., Marsh, K.N., and Sloan, E.D. (2004) Stable low-pressure hydrogen clusters stored in a binary clathrate hydrate. *Science*, 306(5695), 469-71.
- Gallmeier, J., Schafer, H., and Weiss, A. (1969) Cage structure as a feature common to compounds K₈E₄₆ (E = Si, Ge, Sn). *Zeitschrift fur naturforschung Part B Chemie Biochemie Biophysik Biologie und Verwandten Gebiete*, B24(6), 665.
- Gough, S.R., Garg, S.K., and Davidson, D.W. (1974) Ordering of guest-molecule dipoles in the structure 1 clathrate hydrate of trimethylene oxide. *Chemical Physics*, 3(2), 239-47.
- Griffiths, D.J. (1995) Introduction to Quantum Mechanics. Prentice Hall Inc., New Jersey.
- Grochala, W., and Edwards, P.P. (2004) Thermal decomposition of the non-interstitial hydrides for the storage and production of hydrogen. *Chemical Reviews*, 104(3), 1283-1315.
- Halpern, Y., Thieu, V., Henning, R.W., Wang, X.P., and Schultz, A.J. (2001) Time-resolved in situ neutron diffraction studies of gas hydrate: Transformation of structure II (sII) to structure I (sI). *Journal of the American Chemical Society*, 123(51), 12826-12831.
- Henning, R.W., Schultz, A.J., Thieu, V., and Halpern, Y. (2000) Neutron diffraction studies of CO₂ clathrate hydrate: formation from deuterated ice. *Journal of Physical Chemistry. A*, 104(21), 5066-5071.

- Herzog, H., Golomb, D., and Zemba, S. (1991) Feasibility, modeling and economics of sequestering power plant CO₂ emissions in the deep ocean. *Environmental Progress*, 10(1), 64-74.
- Hester, K.C., Strobel, T.A., Sloan, E.D., Koh, C.A., Huq, A., and Schultz, A.J. (2006) Molecular hydrogen occupancy in binary THF-H₂ clathrate hydrates by high resolution neutron diffraction. *Journal of Physical Chemistry. B, Condensed matter, materials, surfaces, interfaces & biophysical*, 110(29), 14024-14027.
- Hoffert, M.I., Caldeira, K., Jain, A.K., Haites, E.F., Harvey, L.D.D., Potter, S.D., Schlesinger, M.E., Schneider, S.H., Watts, R.G., Wigley, T.M.L., and Wuebbles, D.J. (1998) Energy implications of future stabilization of atmospheric CO₂ content. *Nature*, 395(6705), 881-884.
- Holder, G.D., and Hand, J.H. (1982) Multiple-phase equilibria in hydrates from methane, ethane, propane and water mixtures. *AIChE Journal*, 28(3), 440-447.
- Hwang, M.J., Wright, D.A., Kapur, A., and Holder, G.D. (1990) An experimental-study of crystallization and crystal-growth of methane hydrates from melting ice. *Journal of Inclusion Phenomena and Molecular Recognition in Chemistry*, 8(1-2), 103-116.
- Ishmaev, S.N., Sadikov, I.P., Chernyshev, A.A., Vindryevsky, B.A., Sukhoparov, V.A., Telepnev, A.S., and Kobelyev, G.V. (1983) Neutron structural investigations of solid para-hydrogen at pressures up to 24-kbar. 84(1), 394-403.
- Kasper, J.S. (1965) Clathrate structure of silicon Na₈Si₄₆ and Na_xSi₁₃₆(x 11). *Science*, 150, 1713-1714.
- Koga, K., Tanaka, H., and Nakanishi, K. (1994) Stability of polar guest-encaging clathrate hydrates. *Journal of Chemical Physics*, 101(4), 3127-34.
- Koga, Y., Siu, W.W.Y., and Wong, T.Y.H. (1990) Transition of short-range to medium-range order in aqueous-solution of 2-butoxyethanol. *Journal of Physical Chemistry*, 94(10), 3879-3881.
- Koh, C.A., Savidge, J.L., and Tang, C.C. (1996) Time-resolved *in-situ* experiments on the crystallization of natural gas hydrates. *Journal of Physical Chemistry*, 100(16), 6412-14.
- Koh, C.A., Soper, A.K., Westacott, R.E., Wisbey, R.P., Wu, X., Zhang, W., and Savidge, J.L. (1997) Neutron diffraction measurements of the nucleation and growth mechanisms of methane hydrate. 213th National Meeting of the American Chemical Society. American Chemical Society, San Francisco.

- Koh, C.A., Westacott, R.E., Zhang, W., Hirachand, K., Creek, J.L., and Soper, A.K. (2002) Mechanisms of gas hydrate formation and inhibition. *Fluid Phase Equilibria*, 194, 143-151.
- Krawitz, A.D. (2001) *Introduction to Diffraction in Materials Science and Engineering*. John Wiley and Sons, Inc.
- Kroto, H.W., Heath, J.R., O'Brien, S.C., Curl, R.F., and Smalley, R.E. (1985) C₆₀: Buckminsterfullerene. *Nature*, 318(6042), 162-3.
- Kuhs, W.F., Chazallon, B., Radaelli, P., Pauer, F., and Kipfstuhl, J. (1996) Raman spectroscopic and neutron diffraction studies on natural and synthetic clathrates of air and nitrogen NGH '96 - 2nd international conference on natural gas hydrates, PROCEEDINGS. 9-16 p.
- Kvenvolden, K.A. (2000) Gas hydrate and humans. *Annals of the New York Academy of Sciences*, 912, 17-22.
- Larson, A.C., and von Dreele, R.B. (1994) *General Structure Analysis System (GSAS)*. Los Alamos National Laboratory Report LAUR 86-748 (1994).
- Lebruman, J. (1969) Raman diffusion spectra of ethylene oxide and ethylene sulfide in sulfide in solid phase. *Comptes Rendus Hebdomadaires des Seances de l'Academie des sciences serie B*, 268(6), 486.
- Lee, H., Lee, J.W., Kim, D.Y., Park, J., Seo, Y.T., Zeng, H., Moudrakovski, I.L., Ratcliffe, C.I., and Ripmeester, J.A. (2005) Tuning clathrate hydrates for hydrogen storage. *Nature*, 434(7034), 743-746.
- Lisowski, P.W., and Schoenberg, K.F. (2006) The Los Alamos Neutron Science Center. *Nuclear Instruments & Methods in Physics Research. Section A, Accelerators, Spectrometers, Detectors and Associated Equipment*, 562(2), 910-14.
- Lokshin, K.A., and Yusheng, Z. (2005) Advanced setup for high-pressure and low-temperature neutron diffraction at hydrostatic conditions. *Review of Scientific Instruments*, 76(6), 63909-1.
- Lokshin, K.A., Zhao, Y.S., He, D.W., Mao, W.L., Mao, H.K., Hemley, R.J., Lobanov, M.V., and Greenblatt, M. (2004) Structure and dynamics of hydrogen molecules in the novel clathrate hydrate by high pressure neutron diffraction. *Physical Review Letters*, 93(12), 125503-4.
- Majumdar, A., Mahmoodaghdam, E., and Bishnoi, P.R. (2000) Equilibrium hydrate formation conditions for hydrogen sulfide, carbon dioxide, and ethane in aqueous

- solutions of ethylene glycol and sodium chloride. *Journal of Chemical and Engineering Data*, 45(1), 20-22.
- Mak, T.C.W., and McMullan, R.K. (1965) Polyhedral clathrate hydrates. Structure of double hydrate of tetrahydrofuran and hydrogen sulfide. *Journal of Chemical Physics*, 42(8), 2732.
- Mao, W.L., and Mao, H.K. (2004) Hydrogen storage in molecular compounds. *Proceedings of the National Academy of Sciences of the United States of America*, 101(3), 708-710.
- Mao, W.L., Mao, H.K., Goncharov, A.F., Struzhkin, V.V., Guo, Q.Z., Hu, J.Z., Shu, J.F., Hemley, R.J., Somayazulu, M., and Zhao, Y.S. (2002) Hydrogen clusters in clathrate hydrate. *Science*, 297(5590), 2247-9.
- Mao, W.L., Struzhkin, V.V., Mao, H.-K., and Hemley, R.J. (2005) Pressure-temperature stability of the van der Waals compound $(\text{H}_2)_4\text{CH}_4$. *Chemical Physics Letters*, 402(1-3), 66-70.
- McMullan, R.K., and Jeffrey, G.A. (1965) Polyhedral clathrate hydrates. Structure of ethylene oxide hydrate. *Journal of Chemical Physics*, 42(8), 2725.
- Mei, D.-H., Liao, J., Yang, J.-T., and Guo, T.-M. (1996) Experimental and modeling studies on the hydrate formation of a methane+nitrogen gas mixture in the presence of aqueous electrolyte solutions. *Industrial & Engineering Chemistry Research*, 35(11), 4342-4347.
- Mittal, K.L. (1977) *Micellization, Solubilization and Microemulsions*. Plenum Press, New York., Volume 1.
- Murthy, S.S.N. (1999) Detailed study of ice clathrate relaxation: Evidence for the existence of clathrate structures in some water-alcohol mixtures. *Journal of Physical Chemistry. A*, 103(40), 7927-7937.
- Myers, D. (1988) *Surfactant science and technology*. VCH Publishers, Inc.: New York, New York, USA; VCH Verlagsgesellschaft MBH: Weinheim, West Germany. Illus; XIII 351P p.
- Nicol, J.M., Eckert, J., and Howard, J. (1988) Dynamics of molecular hydrogen adsorbed in CoNa - a zeolite. *Journal of Physical Chemistry*, 92(25), 7117-7121.
- Patchkovskii, S., and Tse, J.S. (2003) Thermodynamic stability of hydrogen clathrates. *Proceedings of the National Academy of Sciences of the United States of America*, 100(25), 14645-14650.

- Pynn, R. (1989) Neutron Scattering-- A Primer. Los Alamos Science.
- Rawn, C.J., Rondinone, A.J., Chakoumakos, B.C., Circone, S., Stern, L.A., Kirby, S.H., and Ishii, Y. (2003) Neutron powder diffraction studies as a function of temperature of structure II hydrate formed from propane. *Canadian Journal of Physics*, 81(1-2), 431-8.
- Ripmeester, J.A., and Ratcliffe, C.I. (1998) The diverse nature of dodecahedral cages in clathrate hydrates as revealed by Xe-129 and C-13 NMR spectroscopy: CO₂ as a small-cage guest. *Energy & Fuels*, 12(2), 197-200.
- Rosi, N.L., Eckert, J., Eddaoudi, M., Vodak, D.T., Kim, J., O'Keeffe, M., and Yaghi, O.M. (2003) Hydrogen storage in microporous metal-organic frameworks. *Science*, 300(5622), 1127-9.
- Roux, G., Perron, G., and Desnoyers, J.E. (1978) Heat capacity evidence for pseudophase transitions in aqueous organic binary systems. *Journal of Physical Chemistry*, 82(8), 966.
- Rowsell, J.L.C., Eckert, J., and Yaghi, O.M. (2005) Characterization of H₂ binding sites in prototypical metal-organic frameworks by inelastic neutron scattering. *Journal of the American Chemical Society*, 127(42), 14904-14910.
- Rowsell, J.L.C., and Yaghi, O.M. (2005) Strategies for hydrogen storage in metal-organic frameworks. *Angewandte Chemie*, 44(30), 4670-4679.
- Sagara, T., Klassen, J., Ortony, J., and Ganz, E. (2005) Binding energies of hydrogen molecules to isorecticular metal-organic framework materials. *Journal of Chemical Physics*, 123(1), 014701.
- Saji, A., Yoshida, H., Sakai, M., Tanii, T., Kamata, T., and Kitamura, H. (1992) Fixation of carbon dioxide by clathrate hydrate. *Energy Conversion and Management*, 33(5-8), 643-649.
- Sandford, S.A., Allamandola, L.J., and Geballe, T.R. (1993) Spectroscopic detection of molecular-hydrogen frozen in interstellar ices (retracted article. See vol 287, pg 976, 2000). *Science*, 262(5132), 400-404.
- Schlapbach, L., and Zuttel, A. (2001) Hydrogen-storage materials for mobile applications. *Nature*, 414(6861), 353-8.
- Sloan, E.D. (1998a) Clathrate Hydrates of Natural Gases. Marcel Dekker, Inc., New York.

- . (1998b) Gas hydrates: Review of physical/chemical properties. *Energy & Fuels*, 12(2), 191-196.
- Smith, A.P., Benedek, R., Trouw, F.R., Minkoff, M., and Yang, L.H. (1996) Quasi-two-dimensional quantum states of H₂ in stage-2 Rb-intercalated graphite. *Physical Review. B, Condensed Matter*, 53(15), 10187-99.
- Spiekermann, M., Bougeard, D., and Schrader, B. (1982) Coupled calculations of vibrational frequencies and intensities. III. IR and Raman spectra of ethylene oxide and ethylene sulfide. *Journal of Computational Chemistry*, 3(3), 354-62.
- Staykova, D.K., Kuhs, W.F., Salamatin, A.N., and Hansen, T. (2003) Formation of porous gas hydrates from ice powders: Diffraction experiments and multistage model. *Journal of Physical Chemistry. B, Condensed Matter, Materials, Surfaces, Interfaces & Biophysical*, 107(37), 10299-10311.
- Stern, L.A., Hogenboom, D.L., Durham, W.B., Kirby, S.H., and Chou, I.M. (1998a) Optical-cell evidence for superheated ice under gas-hydrate-forming conditions. *Journal of Physical Chemistry. B, Condensed Matter, Materials, Surfaces, Interfaces & Biophysical*, 102(15), 2627-2632.
- Stern, L.A., Kirby, S.H., Circone, S., and Durham, W.B. (2004) Scanning electron microscopy investigations of laboratory-grown gas clathrate hydrates formed from melting ice, and comparison to natural hydrates. *American Mineralogist*, 89(8-9), 1162-1175.
- Stern, L.A., Kirby, S.H., and Durham, W.B. (1996) Peculiarities of methane clathrate hydrate formation and solid-state deformation, including possible superheating of water ice. *Science*, 273(5283), 1843-8.
- . (1998b) Polycrystalline methane hydrate: Synthesis from superheated ice, and low-temperature mechanical properties. *Energy & Fuels*, 12(2), 201-211.
- Stern, L.A., Kirby, S.H., Durham, W.B., Circone, S., and Waite, W.F. (2000) Natural Gas Hydrate, in *Oceanic and Permafrost Environments* Kluwer Publishers, 323-348.
- Stevenson, D.J. (1999) Life-sustaining planets in interstellar space? *Nature*, 400(6739), 32-32.
- Subramanian, S., Kini, R.A., Dec, S.F., and Sloan, E.D. (2000a) Evidence of structure II hydrate formation from methane plus ethane mixtures. *Chemical engineering science*, 55(11), 1981-1999.

- . (2000b) Structural transition studies in methane plus ethane hydrates using Raman and NMR. *Annals of the New York Academy of Sciences*, 912, 873-886.
- Subramanian, S., and Sloan, E.D. (1999) Molecular measurements of methane hydrate formation. *Fluid Phase Equilibria*, 158, 813-820.
- Suess, E., Borhmann, G., Rickert, D., Kuhs, W.F., Torres, M.E., Trehu, A.M., and Linke, P. (2002) Properties and fabric of near-surface methane hydrates at Hydrate Ridge, Cascadia margin. *Proceedings of the 4th International Conference on Gas Hydrates*, Yokohama, Japan, May, 2002.
- Sun, L., Banhart, F., Krasheninnikov, A.V., Rodriguez-Manzo, J.A., Terrones, M., and Ajayan, P.M. (2006) Carbon nanotubes as high-pressure cylinders and nanoextruders. *Science*, 312(5777), 1199-202.
- Takeya, S., Hondoh, T., and Uchida, T. (2000) In situ observation of CO₂ hydrate by X-ray diffraction. *Annals of the New York Academy of Sciences*, 912, 973-982.
- Tam, C.N., Trouw, F.R., and Iton, L.E. (2004) Inelastic neutron scattering study of the activation of molecular hydrogen in silver-exchanged a zeolite: First step in the reduction to metallic silver at low temperature. *Journal of Physical Chemistry. A*, 108(21), 4737-4743.
- Tse, J.S., Ratcliffe, C.I., Powell, B.M., Sears, V.F., and Handa, Y.P. (1997) Rotational and translational motions of trapped methane. Incoherent inelastic neutron scattering of methane hydrate. *Journal of Physical Chemistry. A*, 101(25), 4491-5.
- Tse, J.S., Shpakov, V.P., Belosludov, V.R., Trouw, F., Handa, Y.P., and Press, W. (2001) Coupling of localized guest vibrations with the lattice modes in clathrate hydrates. *Europhysics letters*, 54(3), 354-60.
- Uchida, T., Takeya, S., Kamata, Y., Ikeda, I.Y., Nagao, J., Ebinuma, T., Narita, H., Zatsepina, O., and Buffett, B.A. (2002) Spectroscopic observations and thermodynamic calculations on clathrate hydrates of mixed gas containing methane and ethane: Determination of structure, composition and cage occupancy. *Journal of Physical Chemistry. B, Materials, Surfaces, Interfaces & Biophysical*, 106(48), 12426-31.
- Wang, X.P., Schultz, A.J., and Halpern, Y. (2002) Kinetics of methane hydrate formation from polycrystalline deuterated ice. *Journal of Physical Chemistry. A*, 106(32), 7304-7309.
- Wang, Z.W., and Zhao, Y.S. (2006) High-pressure microscopy. *Science*, 312(5777), 1149-1150.

- Wegener, W., Vanderhaeghen, J., Hautecler, S., and van Gerven, L. (1978) Rotational motion of cyclic ether molecules in clathrate hydrates studied by neutron scattering. II. Inelastic scattering by ethylene oxide. *Physica B + C*, 95B C(1), 71-5.
- White, M.A., MacLaren, D.C., Marriott, R.A., and Zhan, B.Z. (2003) Thermodynamic stability of clathrate hydrates relative to their separate chemical components. *Canadian Journal of Physics*, 81(1-2), 175-82.
- Williams, K.D., and Devlin, J.P. (1997) Formation and spectra of clathrate hydrates of methanol and methanol-ether mixtures. *Journal of Molecular Structure*, 416(1-3), 277-86.
- Xu, M.Z., Elmatad, Y.S., Sebastianelli, F., Moskowitz, J.W., and Bacic, Z. (2006) Hydrogen molecule in the small dodecahedral cage of a clathrate hydrate: Quantum five-dimensional calculations of the coupled translation-rotation eigenstates. *Journal of Physical Chemistry. B, Condensed Matter, Materials, Surfaces, Interfaces & Biophysical*, 110(49), 24806-24811.
- Yildirim, T., and Hartman, M.R. (2005) Direct observation of hydrogen adsorption sites and nanocage formation in metal-organic frameworks. *Physical Review Letters*, 95(21), 1-4.
- Young, J.A., and Koppel, J.U. (1964) Slow neutron scattering by molecular hydrogen and deuterium. *Physical Review*, 135(3A), A603-A611.